ASSESSMENT OF THE CORROSION BEHAVIOUR OF ALLOYS 825 AND 625 IN STAGNANT SEAWATER- EFFECT OF TEMPERATURE AND WELDING

BY

PEDRO CLÁUDIO FRANCISCO CHICUBA

A thesis submitted to the Faculty of Engineering Built Environment, University of Cape Town, fulfillment of the degree of Master of Science in Materials Engineering.

Department of Mechanical Engineering,

Centre for Materials Engineering

University of Cape Town

June 2017

DECLARATION

I, Pedro Cláudio Francisco Chicuba, know the meaning of plagiarism and declare that all the work in this document, save for that which is properly acknowledged, is my own. This dissertation has been submitted to the Turnitin module and I confirm that my supervisor has seen my report and any concerns revealed by such have been resolved with my supervisor.

Signature: signature removed .....

Date: 23.06.2017 .....

ABSTRACT

Alloy 825 has been extensively used as a cladding alloy in the gas and oil industry for process piping up to and including the manifolds, separators, wellheads, risers and valves. The outstanding corrosion resistance of alloy 825 against general and localised corrosion attack is attributed to its high Ni, Cr and Mo content. However, corrosion failures of alloy 825 equipment have been observed in offshore environments. Alloy 825 has good weldability and for applications that require exceptional resistance to corrosion, Inconel filler metal 625 is used as ''overmatching composition''. Nevertheless, there is always a threat of galvanic corrosion when two dissimilar alloys are electrically connected.

In this study, the corrosion behaviour of alloy 825, alloy 625 weld and alloy 825 weldment[1] have been investigated. Potentiodynamic polarization curves for the alloys were recorded in synthetic seawater across a range of temperatures (30 to 60°C). Mixed potential theory was applied to determine corrosion potentials, rates of corrosion and predict the galvanic effect of coupling alloy 825 to alloy 625 filler metal via welding. Three standard methods were considered to determine the critical pitting temperature (CPT) for alloy 825. Lastly, long-term immersion tests in seawater were conducted to determine the relationship between the laboratory accelerated tests results and the performance of the alloys under real service conditions.

The results from the experimental tests revealed that alloy 825 and alloy 625 weld exhibit outstanding corrosion resistance to uniform corrosion, despite the effect of temperature on the corrosion rate of both alloys. The galvanic effect of coupling alloy 825 to alloy 625 via welding is insignificant. The corrosion morphology of alloy 825 and its weldment is temperature dependent. At temperatures below 45 °C, grain boundary attack was observed in alloy 825 samples, while pitting corrosion was observed at temperatures higher than 50 °C. Alloy 625 weld exhibited only one mode of corrosion attack, namely the selective dissolution of interdendritic phase throughout the test temperature range. There was no agreement between the CPT results for alloy 825 and its weldment obtained using the three standard methods. No correlation was found between CPT determined by laboratory tests and the temperature above which alloy 825 would suffer pitting corrosion in long term seawater exposure tests.

[1] Alloy 825 weldment is made of alloy 825 as the base material and alloy 625 filler metal as the fusion zone

ACKNOWLEDGEMENTS

I wish to express my deep gratitude and sincere thanks to all those who assisted me in the completion of this thesis, in particular:

- My supervisor, Professor Robert D. Knutsen, for his kind support, valuable advice and continuous supervision throughout this research project. Moreover, showing the trust and giving me the opportunity to accomplish my goals.

- My mentor, Mr. Ryan Matthews, for his constant engagement and meticulous suggestions during the discussions. Furthermore, believing in me and being such a role model.

- CME senior technical officer, Mrs. Penny Louw, for making sure all the lab equipment was always at hand and being a mother figure in one of the darkest days of my life.

- Mr. Pierre Smith, Mr. Peter Jacobs, Mr. Horst Emrich and the rest of the mechanical engineering technical staff for making any idea possible.

- Dr. Innocent Shuro and Mrs. Miranda Waldron for their SEM expertise.

Above all, I worship you almighty GOD for giving me the intellect, good health, strength and motivation to complete this master's thesis. Only due to His blessing I finish my research.

I dedicate this dissertation to:

My beloved grandmother, Maria Teresa, a true leader who inspired me in so many ways

My parents for their unconditional love and support

My brother and two sisters, Marcio, Francisca and Paula

My daughter, Francisca Hulisani, for her innocence and existence

My wife, Livhuwani, for her endless love and believing in me

None of this would be possible, without you all.

Table of Contents

LIST OF FIGURES

LIST OF TABLES

ABBREVIATIONS

Acronym	Definition
ASME	American Society for Mechanical Engineers
ASTM	American Society for Testing and Materials
API	American Petroleum Institute
AWS	American Welding Society
BP	British Petroleum
CCT	Critical Crevice Temperature
CPT	Critical Pitting Temperature
CR	Corrosion Rate
CRA	Corrosion Resistant Alloy
EDL	Electric Double Layer
EDS	Energy Dispersive Spectroscopy
EW	Equivalent Weight
FZ	Fusion Zone
HAZ	Heat Affected Zone
IHP	Inner Helmholtz Plane
IUPAC	International Union of Pure and Applied Chemistry
NACE	National Association for Corrosion Engineers
OCP	Open Circuit Potential
OHP	Outer Helmholtz plane
PR	Penetration Rate
PWHT	Post Weld Heat Treatment
SCE	Saturated Calomel Electrode
SEM	Scanning Electron Microscope

LIST OF SYMBOLS

The list of symbols is restricted to those repeatedly throughout the text.

Symbol	Definition	Unit
A^A	Anode area	mm^2
A^C	Cathode area	mm^2
b_a	Anodic Tafel slope	V/A
b_c	Cathodic Tafel slope	V/A
E	Potential	V
E°	Reversible standard potential	V
E_a	Activation energy	KJ/mol
E_{corr}	Mixed potential or Corrosion potential	V
E_g	Galvanic potential	V
E_{pit}	Pitting potential	V
E_{prot}	Protection potential	V
F	Faraday's constant	C/mol
i	Current density	$\mu A/cm^2$
i_a	Anodic current density	$\mu A/cm^2$
i_c	Cathodic current density	$\mu A/cm^2$
i_L	Limiting diffusion current density	$\mu A/cm^2$
i_{net}	Net current density	$\mu A/cm^2$
i_{pass}	Passive current density	$\mu A/cm^2$
k	Constant rate of corrosion reaction	
n	Number of electrons transferred	
η	Polarization or overpotential	V
η_T	Concentration overpotential	V
[O]	Concentration of oxidising agent	
q	Charge density	
[R]	Concentration of reducing agent	
R_o	Medium resistivity	Ω/cm
R_P	Polarization resistance	Ω

r_a	Anode dissolution rate	mm/yr
r_o	Cathode dissolution rate	mm/yr
T	Temperature	°C
σ	Specific conductivity	µS/m
δ	Wagner polarization parameter	mm
x	Critical dimension	mm
ϒ	Dendritic phase	

CHAPTER ONE: INTRODUCTION

1.1. Problem Description: Motivation

Alloy 825 is a nickel-iron-chromium alloy with the addition of molybdenum, copper and titanium. Due to its excellent corrosion resistance in both reducing and oxidising conditions, alloy 825 has been used as a cladding material on structural steel in the oil and gas industry to counteract corrosive marine conditions. This provides a more economical alternative than using corrosion resistant alloy (CRA) materials for the entire component. Major applications have been in the form of clad pipes, vessels, heat exchangers and valves. Most of the components made from 825 are manufactured using welding techniques and alloys 625 and FM65 are used as ”overmatching” filler metals (Paul et al., 2004 and DuPont et al., 2009:54). The higher alloy content of 625 produces a weld with corrosion resistance better than the base metal (Crum et al., 2000).

Even though alloy 825 is commonly used for offshore conditions, there have been reports of crevice and pitting corrosion under conditions where this was not expected. For example, Amon et al.(1999) observed pitting and crevice attack in 825 in contact with 0 to 10^{o}C seawater at depths of 500m. General observation was that short-term exposure of up to 20 days did not result in corrosion but exposure longer than 50 days resulted in severe attack. High pressures (50 bar) at depths in seawater were found to be the driving force for the corrosive attack. Furthermore, BP (British Petroleum) has reported a corrosion accident involving a riser tower made of steel pipes internally cladded with 825 (Figure 1.1).

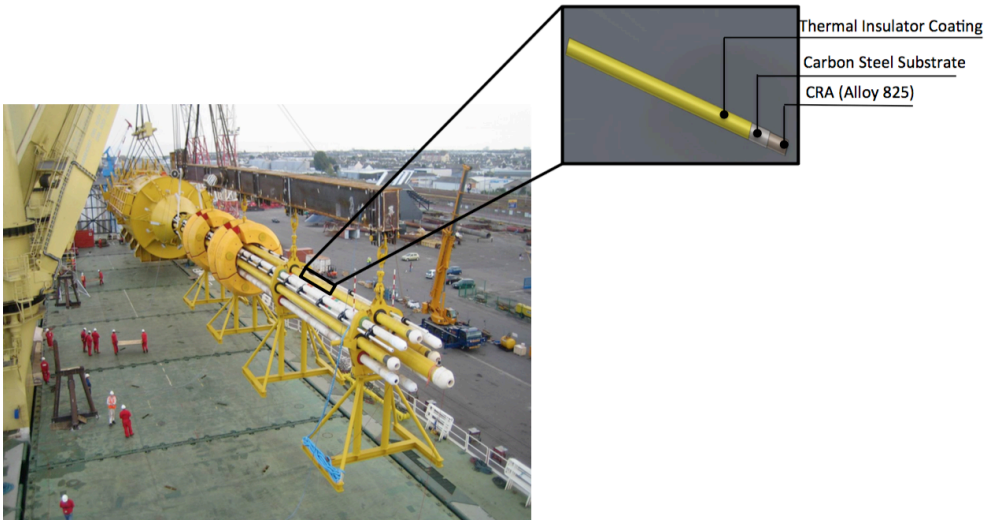

Figure 1.1 Upper section of the riser where pitting corrosion was observed and layout of the steel clad pipe

The equipment was inspected after 5 years of service in hydrocarbon production lines and the results revealed that one of the pipes was seriously damaged by pitting corrosion. Figure 1.2 shows a cross section through the largest pit and an external view of the same feature, which was located close to one of the circumferential alloy 625 welds. The black dashed line in Figure 1.2a shows the shape of the feature and the interface between alloy 825 (top) and the carbon steel (below). The pit has penetrated through the 3 mm thick alloy 825 cladding and removed 7 mm of the underlying carbon steel leading to a total pit depth of 10 mm. The red/yellow section in Figure 1.2b is the base of the pit where there is 8 mm of wall thickness remaining. It is believed that the cladding became partially detached from the carbon steel around the perimeter of the pit.

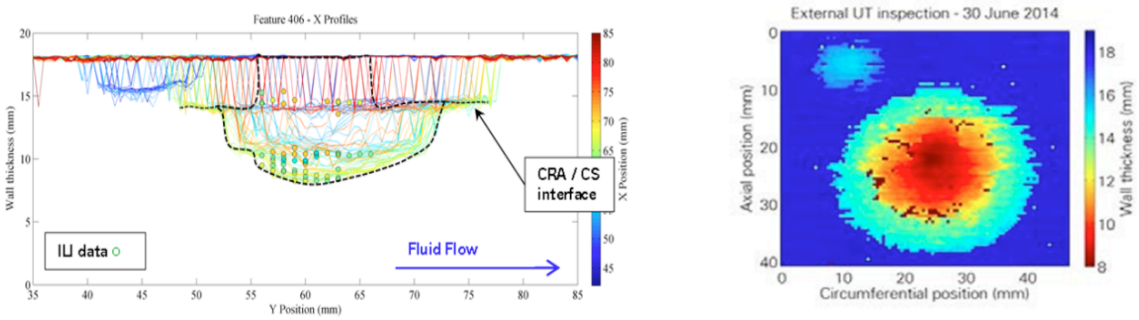

a b

Figure 1.2 Cross section and external view of the largest pit based on a) Combination of in-line inspection tool and external ultrasonic testing b) External ultrasonic testing

The surprising aspect of the incident is that the corrosion attack started from the alloy 825, which was supposed to protect the pipe against corrosive attack. The material certificates for the alloy 825 clad pipes, which was manufactured by BUTTING GMBH & CO.KG (Appendix A), indicate that the pipe's internal surfaces were brushed, ground and pickled to remove surface contamination and heat tint. This is confirmation that all contamination was removed and the passivation of the 825 clad pipes was achieved before the pipes left BUTTING GMBH & CO.KG. It is possible that the corrosion started during the construction period of the riser tower in one of the Angolan offshore oil fields. The upper section of the riser tower was stored in the sea for approximately 6 months prior to the welding operation. The seawater might have entered the pipe and the combined effect of the seawater chloride concentration and temperature caused the corrosion damage in the pipe (Figure 1.3). However, research is needed to confirm whether seawater was the cause of the corrosion of the alloy 825 clad pipes.

Figure 1.3 Upper section of the tower riser stored in the sea prior the welding operation

1.2. Research Objectives

As a result of the unexpected corrosion events which occurred in the aforementioned riser tower example, a number of research objectives were developed to characterise the corrosion performance of alloy 825 in seawater, and more particularly in stagnant (or non-flowing without constant aeration) seawater. In addition, alloy 625 was included in the study in view of the use of this alloy as a weld filler, which also gave rise to the consideration of the corrosion galvanic effect when alloy 825 is in contact with alloy 625 in seawater. The study was designed in such a way as to evaluate the robustness of alloy 825 in providing corrosion resistance in seawater under conditions of temporary stagnation and temperature fluctuations (30-60°C). Consequently, the primary focus is in characterising the corrosion behaviour of alloy 825, alloy 625, and the alloy 825/625 couple using a range of experimental conditions that involve the use of seawater under stagnant conditions. The specific objectives are listed as:

- To determine the corrosion potential and uniform current density of alloy 825 and alloy 625 weld in seawater at different temperatures.

- To predict the mixed potential and galvanic current density of an alloy 825|625 couple at different temperatures.

- To determine the breakdown potential of alloys 825 and 625 at different temperatures.

- To determine the critical pitting temperature for alloy 825 and its weldment in seawater.

- To check whether the critical pitting temperature determined for alloy 825 weldment by electrochemical laboratory testing is also the temperature above which alloy 825 would suffer from pitting corrosion in seawater immersion tests.

1.3. Research Approach

The investigation initiated with a review of the relevant published literature. Particular attention was paid to the thermodynamics and kinetics of corrosion, the susceptibility to galvanic and pitting corrosion and the general corrosion resistance of alloys 825 and 625. To try to fill the gaps in our knowledge about the corrosion behaviour of alloys 825 and 625 and the effect of coupling alloy 825 to 625 via welding, electrochemical laboratory tests together with long-term immersion tests were performed using natural and synthetic seawater. In addition, surface examination was conducted on samples after each test to record the mode of corrosion failure.

1.4. Limitations

This study is limited to the corrosion behaviour of alloy 825 and its weldment in stagnant seawater. The author understands in addition to uniform corrosion, grain boundary attack and pitting corrosion, there are other types of corrosion attack a metal may be subject to in seawater and these include crevice corrosion, microbially induced corrosion, cavitation corrosion and erosion corrosion. They are all of importance in the prediction of the metal alloy service life. However, uniform, grain boundary and pitting corrosion are the only corrosion mechanisms considered in this investigation. Furthermore, this study does not attempt to simulate directly any particular seawater environment nor does it attempt to investigate any particular failure analysis situation.

1.5. Structure

This dissertation is arranged into five chapters. The first chapter introduces this study and its background, objectives, limitations, approach and structure. Chapter Two records the results of a literature survey, which covered the thermodynamics and kinetics of corrosion and identifies the parameters that affect the susceptibility of alloys 825 and 625 weld to galvanic and pitting corrosion as well as general corrosion resistance. In Chapter Three, the experimental procedures employed for microstructure characterisation and corrosion evaluation in this research are presented. In Chapter Four the electrochemical test results, corrosion behaviour and morphologies for alloys 825 and 625 and its weldment are presented and discussed. The focus here was to quantify the effect of coupling alloy 825 to 625 weld and to determine the critical pitting temperature of alloy 825 and its weldment.In Chapter

Five the conclusions and findings of the work are presented as well as recommendations for future work.

CHAPTER TWO: LITERATURE REVIEW

2.1. Fundamentals of Corrosion

2.1.1. Definition of Corrosion

The NACE/ASTM G193-12d standard defines corrosion as "the deterioration of a metal, that results from a chemical or electrochemical reaction with its environment." Corrosion can take many forms and these depend on the morphology of the attack, as well as the type of environment to which the material is exposed. Traditionally, corrosion is classified into eight categories. The simplest type of corrosion encountered is uniform corrosion, which is characterized by attack that extends almost uniformly over the whole exposed surface (Fontana, 1987:9).

It is very rare to find metals in their pure state in nature, more commonly, they are chemically combined with other elements to form metallic ores such as oxides, sulfides and carbonates. Extraction of a metal from its ore involves supplying a tremendous amount of energy into the furnace as form of heat, which increases the Gibbs free energy (chemical energy) of the metals (Figure 2.1). After production, metals tend to revert to their lower energy level, more natural state of ore (Shreir, 1982: 2). Therefore, the driving force for all corrosion process is the reduction of the refined metal Gibbs energy to a more stable state.

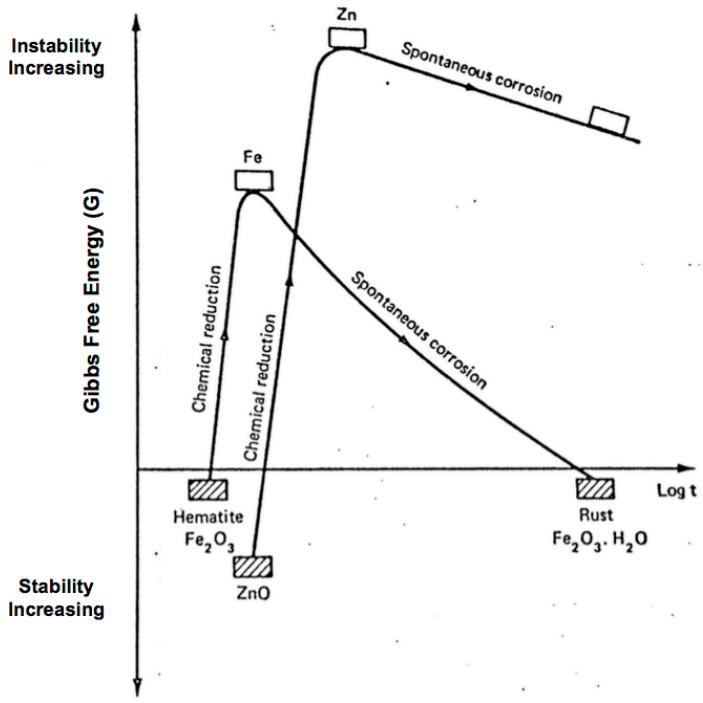

Figure 2.1 Energy profile of metallic zinc, iron and their compounds (Shreir, 1982)

2.1.2. Mechanism of Aqueous Corrosion

It is generally accepted that the corrosion of a metal in aqueous solution occurs via an electrochemical process, in which the corroding metal is oxidized to higher valence state (Shreir, 1982:9). The electrochemical cell has four components namely: the anode, cathode, electrolyte, which provides a path for ionic conduction and an electrical connection to allow electrons to flow between anode and cathode (Figure 2.2). Electrochemical corrosion will only occur if all four components are available and interactive (Jones, 1996:5).

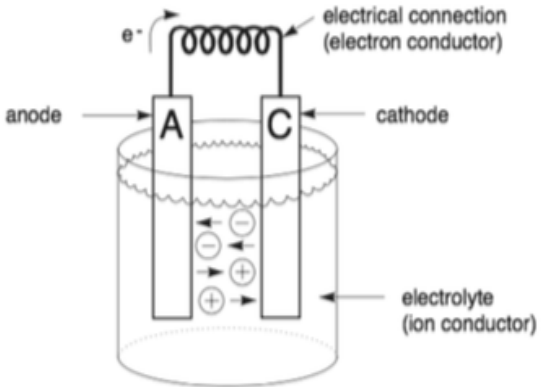

Figure 2.2 Electrochemical corrosion cell (Bradford, 2001)

The anode is where oxidation (loss of electrons) occurs and the metal ions (M^{n+}) enter the electrolyte, while the electrons (ne^-) are attracted to the cathode. The anodic reaction is written in general form:

$$M \rightarrow M^{n+} + ne^- \qquad \text{(Equation 1)}$$

Where M is the metal (anode), M^{n+} is the metal ion showing its valence (n+), e^- electrons and n represents the number of electrons.

Each oxidation reaction must be accompanied by a reduction reaction, which takes place at the cathode. Depending on the pH of the aqueous solution, the most common cathodic reactions are either oxygen reduction (basic solution) or hydrogen reduction (acidic solution)

$$O_2 + 4H^+ + 4e^- \rightarrow 2H_2O \qquad \text{(Equation 2)}$$

$$2H^+ + 2e^- \rightarrow H_2(g) \qquad \text{(Equation 3)}$$

2.2. Thermodynamics of Aqueous Corrosion: Reversible Potential

When a piece of pure iron is immersed in a deaerated ferric solution, a potential difference is established at the metal-solution interface and the following redox equilibrium reaction takes place at the metal surface:

$$Fe_{(S)} \rightleftharpoons Fe^{2+}_{(aq)} + 2e^{-} \qquad \text{(Equation 4)}$$

The potential difference across the metal-solution interface is called the reversible electrode potential and it represents the potential at which the metal is at equilibrium with its own ions (Groysman, 2009: 291). In the equilibrium state at constant temperature, there is no net reaction taking place at the surface of the metal and the reversible electrode potential is given by the Nernst equation (Pourbaix, 1974: 58):

$$E = E^{o} + \frac{2.3RT}{nF}\log\frac{[O]}{[R]} \qquad \text{(Equation 5)}$$

E° is a standard reversible potential, R = 8.314 J/(mol·K) is the universal gas constant, T is the solution absolute temperature, F = 9648.534 C/mol is the Faraday's constant, n is the number of electrons involved in the reaction. For the iron-electrode reaction, [O] represents the Fe^{2+} concentration (oxidizing agent) and [R] represents the Fe concentration (reducing agent). Electrode reversible potential is commonly regarded as a measure of the oxidizing power of the solution and it is used to rank metals with respect to their tendencies to corrode (Kelly et al., 2002: 90).

Experimentally, absolute electrode potential is not a measureble quantity (Trasatti, 1986). To measure a relative electrode potential at equilibrium, a reference electrode is used. The standard hydrogen electrode is conventionally used as a standard reference to compare other reference electrodes. However, for corrosion tests the most commonly used in aqueous solutions are the saturated calomel electrode (SCE), the Ag/AgCl electrode, and the Hg/Hg_2SO_4 electrode (Kelly et al., 2002:17).

2.3. Kinetics of Aqueous Corrosion

2.3.1 Mixed Potential Theory

Wagner and Traud (1938) proposed a theory to explain the operation of a cell containing more than one redox reaction. According to this theory, if the same piece of iron (see section 2.2) is immersed in a solution containing an oxidizing agent such as chloric acid at least two half-cell electrode reactions will occur simultaneously on the electrode interface:

$$Fe \rightarrow Fe^{2+}_{aq} + 2e^{-} \qquad \text{(Anodic reaction)} \qquad \text{(Equation 6)}$$

$$2H^{+}_{aq} + 2e^{-} \rightarrow H_{2(g)} \qquad \text{(Cathodic reaction)} \qquad \text{(Equation 7)}$$

As ilustrated in Figure 2.3, initially after the immersion, both half-cell electrodes will have different potentials ($E_{Fe/Fe(aq)}$ and $E_{H(aq)/2H}$), and gradually each potential will change until they reach a commom value, which is called mixed or corrosion potential (E_{corr}). Under these circumstances, the equilibrium condition of electrode immersed in acid solution may be expressed in form:

$$i_{corr} = i_a = i_c \qquad \text{(Equation 8)}$$

Where, i_{corr} is known as the corrosion current density, i_a and i_c are iron anodic and hydrogen cathodic reactions respectively.

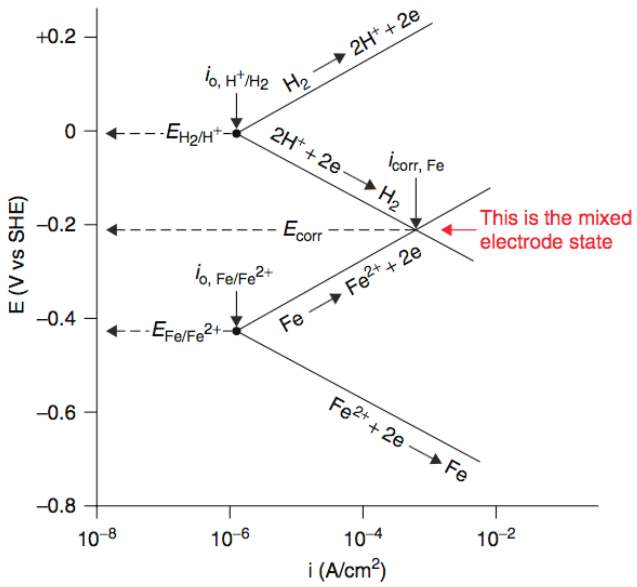

Figure 2.3 Evans diagram for mixed electrode state of iron corrosion in acid (Tan, 2013)

2.3.2 Electrode Polarization

If the system shown in Figure 2.3 is disturbed from the equilibrium position by polarization, a net current (i_{net} = i_a - i_c) will flow between the anode and the cathode. Polarization or overpotential is defined as the potential change from the corrosion potential (E – E_{corr}), caused by a net reaction at the electrode interface (Jones, 1996: 80). In addition, polarization can be divided into two types, namely activation and concentration polarization. Activation polarization occurs when an electrochemical process is controlled by a sequence of reactions at the metal-electrolyte surface (Fontana, 1987: 19). The relationship between the activation polarization and resultant current density is given by Tafel equation (Tan, 2013: 14):

$$\eta = \frac{2.3RT}{\alpha nF} \log \frac{i}{i_{corr}} \qquad \text{(Equation 9)}$$

where η is the overpotential, i the anodic or cathodic current density, i_{corr} the corrosion current density, F is Faraday's constant, R the universal gas constant, T the absolute temperature, n the number of electrons transferred in the anodic and cathodic reactions, and α is the coefficient related to the potential drop through the double layer.

The red line in the Figure 2.4 represents the relationship between the net current and the electrode polarization. It is important to emphasize that experimentally the individual anodic and cathodic current densities cannot be measured. The measured current is the difference between the two current densities i.e. anodic and cathodic.

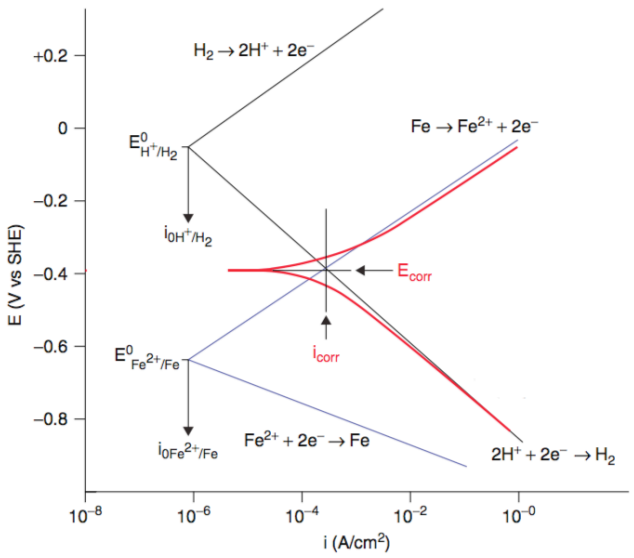

Figure 2.4 Experimental polarization curves and Evans diagram for iron corrosion in deaerated acidic solution (Tan, 2013)

Experimental measurement of the activation polarization may be complicated by two interfering phenomena, namely concentration polarization and a resistance effect (Stern and Geary, 1957). Concentration polarization results when the reduction rates are relatively high at the cathodic sites and the regions adjacent to the electrode surface will become depleted of cations. Due to the concentration gradient, species will be transported from the bulk solution to the electrode interface by diffusion processes. The magnitude of the concentration polarization is given by combining Fick's Law of diffusion with Nernst equation (Jones, 1996: 85):

$$\eta_T = \frac{2.3RT}{nF} \lg\left(1 - \frac{i}{i_L}\right) \qquad \text{(Equation 10)}$$

where η_T is the concentration overpotential, i the anodic or cathodic current density, i_L the limiting diffusion current density, F is Faraday's constant, R the universal gas constant, T the absolute temperature, n the number of electrons transferred in the anodic and cathodic reactions.

The resistance of the solution between the reference electrode and the polarized electrode, and sometimes, the resistance of a passive film formed on the electrode contributes to the total polarization measured (Stern and Geary, 1957). If R is the total resistance, the total potential responsible for anodic polarization (for example) is the sum of activation, concentration and resistance polarization:

$$\eta_T = \frac{2.3RT}{\alpha nF} \log\frac{i}{i_{corr}} + \frac{2.3RT}{nF} \lg\left(1 - \frac{i_c}{i_L}\right) + iR \qquad \text{(Equation 11)}$$

2.3.3 Corrosion rates

The quantification of the corrosion attack depends directly on the mode of corrosion. In the case of uniform corrosion, corrosion rates can be accurately determined by dividing the total mass of the metal lost by the surface area and the time of exposure. However, if the mode of corrosion is localized, e.g. pitting, then the average amount of metal removed over the entire surface is meaningless (Bradford, 2001:44). The rate of penetration is expression, which is used to describe the corrosion rate of almost any type of corrosion except stress corrosion cracking. Corrosion or penetration rate (PR) can be calculated from the corrosion current using Faraday's law (Fontana, 1987):

$$\text{CR (mpy)} = \frac{0.13 \times i_{corr}(EW)}{d} \qquad \text{(Equation 12)}$$

where mpy is milli-inches per year, i_{corr} is the corrosion current density ($\mu A/cm^2$); EW is the equivalent weight of the corroding species (g) and d is the density of the corroding species, (g/cm^3). According to Jones (1996: 77), for iron the equivalence between current density and penetration rate is 1 $\mu A/cm^2 \approx 0.46$ mpy. Table 2.1 summarises the penetration rate (PR) equivalent to 1 $\mu A/cm^2$ for some stainless steels and nickel-based alloys.

Alloys	Oxidation state	Density	EW	PR equiv. to 1 $\mu A/cm^2$
Stainless Steel		g/cm^3		mpy
304	Fe/2,Cr/3,Ni/2	7.9	25.12	0.41
316	Fe/2,Cr/3,Ni/2/Mo3	7.9	24.62	0.41
430	Fe/2,Cr/3	7.7	25.30	0.42
Nickel Alloys				
200	Ni/2	8.89	29.36	0.43
400	Ni/2,Cu/2	8.84	30.12	0.44
600	Ni/2,Fe/2,Cr/3	8.51	26.41	0.40
825	Ni/2,Fe/2,Cr/3/Mo3	8.14	25.52	0.40

Table 2.1 Corrosion current density and its corrosion rate equivalence (Jones, 1996: 77)

The unit **mpy** continues as the most frequently used corrosion rate expression in the United States. However, with the increasing use of metric units in recent years, engineers are more familiar with **mm/yr** and **µm/yr** for high and low corrosion rates respectively. Table 2.2 compares **mpy** with most preferred metric units where **mm/y** produces decimal numbers while **µm/yr** yields very large numbers.

Relative Corrosion Resistance	mpy	mm/yr	µm/yr	nm/h	pm/s
Outstanding	<1	<0.02	<25	<2	<1
Excellent	1-5	0.02-0.1	25-100	2-10	1-5
Good	5-20	0.1-0.5	100-500	10-50	20-50
Fair	20-50	0.5-1	500-1000	50-150	20-50
Poor	50-200	1-5	1000-5000	150-500	50-200
Unacceptable	200+	5+	5000+	500+	200+

Table 2.2 Typical corrosion rate of ferrous and nickel based alloys (Fontana, 1987: 172)

2.4. Galvanic Corrosion

Galvanic corrosion, which is also known as bimetallic corrosion, is one of the more common forms of corrosion. Galvanic corrosion also acts as stimulus for other forms of corrosion such as intergranular corrosion, stress corrosion cracking, pitting and crevice corrosion (Mansfeld, 1971). This type of corrosion attack results from an interaction of reduction and oxidation reactions with coupled metals; whether this type of corrosion will occur depends on many factors such as corrosion potential of the uncoupled metals, current densities, Tafel slopes and area ratios.

2.4.1. Factors Affecting Galvanic Corrosion

Figure 2.5 illustrates some of the factors, which determine whether galvanic corrosion will occur in a particular environment and if so at what rate. A brief discussion of the significance of some of them are given in the following pages.

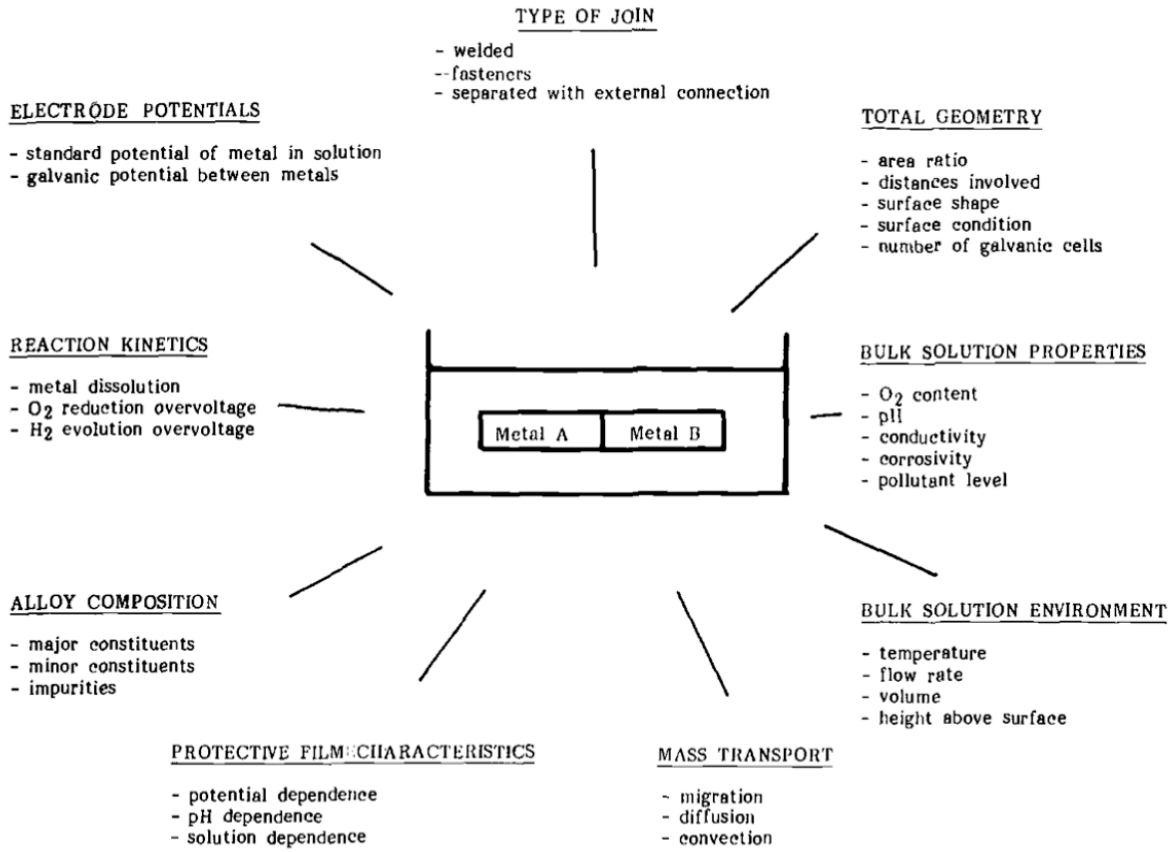

Figure 2.5 Factors affecting galvanic corrosion (Oldfield, 1988)

2.4.1.1. Electrode Potentials

The corrosion behaviour of a galvanic couple can often be predicted based on the corrosion potentials of uncoupled metals in a given environment. Seawater is the most abundant electrolyte and of practical importance, hence, corrosion potential for most metals and alloys have been measured in this medium. Figure 2.6 shows a typical seawater galvanic series. The more negative the value of corrosion potential is for a certain alloy in the galvanic series, the higher will be the tendency to undergo an oxidation reaction when coupled to the alloys with more positive potential. As point out by Mansfeld et al. (1974) galvanic series are good indicators for potential for galvanic corrosion to occur. However, they do not give any indication of the real extent of galvanic corrosion when dissimilar alloys are coupled.

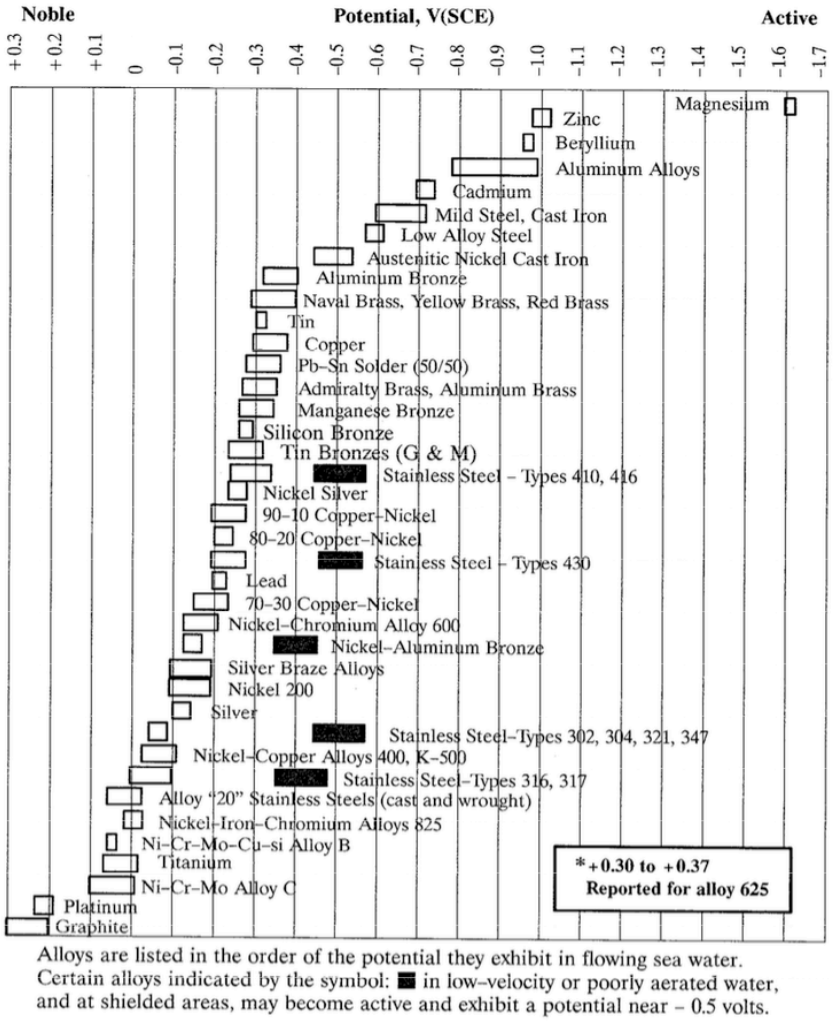

Figure 2.6 Galvanic series for various alloys (ASTM G82-98: 2014)

2.4.1.2. Reaction Kinetics: Galvanic Current

The position of a metal or alloy in the galvanic series (Figure 2.6) indicates whether it will behave as an anode or cathode in the galvanic couple. The galvanic current density, thereafter, indicates the potential rate for galvanic corrosion to occur. According to Mansfeld (1973), the galvanic current density (i_g) results from the difference between the oxidation current density [$i_a(E_g)$] and reduction current density [$i_c(E_g)$] of the anode metal at the galvanic potential (E_g):

$$i_g = i_a(E_g) - i_c(E_g) \qquad \text{(Equation 13)}$$

The galvanic current density can also be expressed as:

$$i_g = i_a - i^A_{corr} * \exp[-\frac{2.3(E_g - E_{corr})}{b^A_c}] \qquad \text{(Equation 14)}$$

Where b^A_c is the Tafel slope for the reduction reaction on the anode, i^A_c and E_{corr} are the corrosion current density and potential of the anodic metal before coupling and i_a is the current density of the anodic metal after coupling. Mansfeld et al. (1974) have proposed three different expressions for the galvanic current based on three common cases of corrosion involving galvanic couples. In the **first case** , the polarisation (E_g - E_{corr}) is considered to be too large such that the dissolution of the metal is the only reaction occurring at the anode and reduction of oxidisers (H^+,H_2O, O_2) are the only reactions occurring at the cathode. Therefore, the measured galvanic current (i_g) equals the anodic dissolution rate (i_a) and Equation 14 reduces to:

$$i_g = i_a \qquad \text{(Equation 15)}$$

The **second case**, the polarisation is assumed to be small such that the oxidation and reduction reactions take place in the anode metal. In this case, the measured galvanic current (i_g) is no longer equal to the anodic dissolution rate, the former current is equal to the difference of anodic and the cathodic currents on the anode metal:

$$i_g = i_a - i_{corr} \qquad \text{(Equation 16)}$$

For reduction reactions under diffusion control (**the third case**), the corrosion current density in the anode metal is equal to the limiting current density for oxygen diffusion (i^L_{O2}). Therefore, the measured galvanic current (i_g) with respect to the anode will be:

$$i_g \approx i_{corr}(\frac{A^C}{A^A}) = i^L_{O_2}(\frac{A^C}{A^A}) \qquad \text{(Equation 17)}$$

where A_A and A_C are the anode and cathode areas in the galvanic couple. Mansfeld and Kenkel (1976: 20) have proposed the relative dissolution rate (Equation 18) as a way to check the compatibility of dissimilar alloys in the galvanic couple.

$$\frac{r_a - r_o}{r_o} = \frac{i_g}{i_{corrA}} \qquad \text{(Equation 18)}$$

where, r_a and r_O are the dissolution rate of the anode metal in the couple and uncoupled conditions respectively, while I_g is the galvanic current and i_{corrA} is the current density of the anode metal in the uncoupled condition respectively. According to their criteria, relative dissolution rate below 5 implies compatibility, between 5 and 15 is borderline and above 15 alloys are incompatible. However, this criteria might have to be modified for different galvanic couples (Mansfeld and Kenkel, 1976: 20).

2.4.1.3. Type of Joint

In many mechanical structures, welding is a preferred joining technique than mechanical fastening, brazing or soldering. However, the corrosion resistance of a weld is generally lower than the metals being joined. This can be attributed to several factors including welding plates with filler metal of different composition resulting in element concentration gradients, which significantly reduce the corrosion resistance of the weld deposit (Scrum et al.,2016). Additionally, weld solidification causes element segregation and precipitation of interdendritic secondary phases in the fusion zone. These segregation and secondary phases can lead to localised corrosion (DuPont, 1996: 146). The best way to minimise the above defects is to use overmatched filler metal, i.e. a filler metal with higher alloy content than the base metal. An alternative approach could be post weld heat treatment for weld homogenization.

2.4.1.4. Area Ratio

Generally, a high cathode to anode ratio results in high galvanic current or anodic dissolution rate whereas a low cathode to anode ratio prevents galvanic corrosion from happening. Mansfeld (1971) investigated the effect of the variation of the cathode to anode area ratio in a galvanic couple using the three common cases already discussed in subsection 2.4.1.2. For the first case, the galvanic potential and the current density of the more noble metal (anode) in the galvanic couple can be expressed as follow (see Mansfeld (1971) for the derivations):

$$\phi_g = k_1 + \frac{b_c}{b_a + b_c} \log \frac{A^C}{A^A} \quad \text{(Equation 19)}$$

$$\log i_g^A = k_2 + \frac{b_c}{b_a + b_c} \log \frac{A^C}{A^A} \quad \text{(Equation 20)}$$

where Φ_g is galvanic potential , i_g is current density of the more noble metal (anode),k_1 and k_2 are constants, b_a and b_c are the Tafel slope for anodic and cathodic reactions respectively, A^A and A^C are the areas of the anodic and cathodic metals. Equation 20 shows that the dissolution rate of the anode (i_g^A) increases as the ratio of cathode to anode area increases, accompanied by an enoblement of the couple galvanic potential (Equation 19). Equation 20 also illustrates the importance of maintaining the ratio of cathode to anode area in any galvanic couple as small as possible.

2.4.1.5. Bulk Solution Properties

The properties of a solution are some of the most important factors affecting the corrosion behavior of a galvanic couple. For example, the level of aggressive anions e.g. halogens or inhibitors determine whether corrosion can occur. The level of oxygen and pH determines the type of cathodic reaction occurring in a specific system. The conductivity controls the corrosion rates at the surface of the metal.

2.4.1.6. Bulk Solution Environment

This group of factors includes the solution temperature, flow rate and height above the couple. In general, the corrosion current density is expected to rise as the temperature increases, according to the well-known Arrhenius equation:

$$k = Ae^{-\frac{E_a}{RT}} \quad \text{(Equation 21)}$$

where k is the rate of the corrosion reaction, E_a (J/mol) is the molar activation energy of the process, R is the gas constant (8.314 J/mol/K), T is the temperature (K) and A is a constant.

2.4.2. Mixed Potential Theory for Two Metals

Mixed potential theory proposed by Wagner and Traud (1938) can also be used to estimate the corrosion behaviour (parameters) of a galvanic couple. In the case of a coupling of two dissimilar metals, the mixed corrosion potential ($E_{corr\ AB}$) and the galvanic current ($i_{corr\ AB}$) fall where the resultant cathodic reaction intercepts the resultant anodic reaction. When metal A is couple to metal B the corrosion rate of the individual members changes such that the anodic current increases from $i_{corr\ B}$ to ($i'_{corr\ B}$) and the cathodic current decreases from $i_{corr\ A}$ to $i'_{corr\ A}$. The position of the curves in the Figure 2.7 and a quatitative prediction of the galvanic current depends on the all the factors discussed in the previous sub-section 2.4.1.

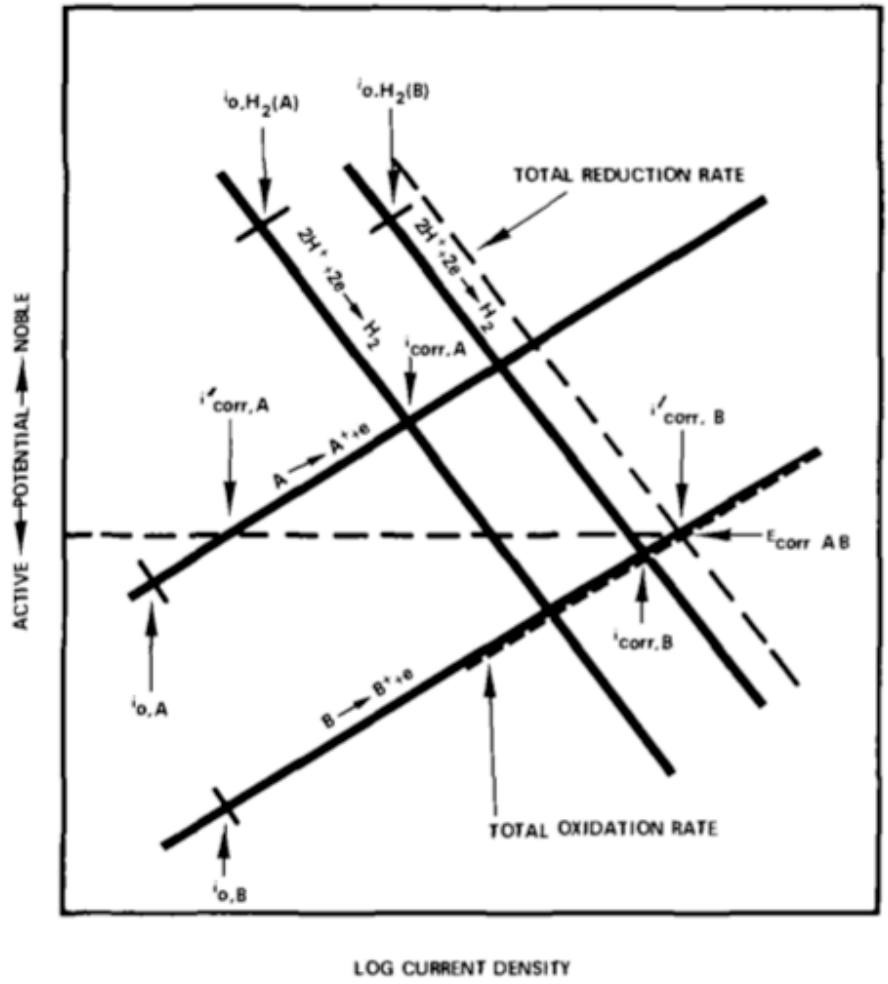

Figure 2.7 Schematic of potential behavior of galvanically coupled metals A and B (Boboian, 1976: 5)

2.4.3. Potential and Current Density Distribution on Galvanic Corrosion

In a given environment, the corrosion potential and current of a galvanic couple may be uniformly distributed or it may vary along the distance away from the couple junction, depending on whether the critical dimension (x) is larger or smaller than the **Wagner polarization parameter (δ)** (Waber, 1954). The critical dimension, x, is half of the width of the anodic member in the galvanic couple. It depends on the configuration of the electrodes and electrolytes (Kennard and Waber, 1970). The polarization parameter has the dimension of length and is defined by Wagner (1951) as:

$$\delta = \sigma \left| \frac{d\Delta E}{di} \right| = \frac{R_P}{R_o} \qquad \text{(Equation 22)}$$

where σ is the specific conductivity of the medium, dΔE and di are the derivatives of the overvoltage and current density of the anodic metal or electrode respectively, R_o is the resistivity of the medium and R_P is the polarization resistance of the anodic metal. When the Wagner number (x/δ) is small, the potential and current density will be uniformly distributed across the couple. On the contrary, if the number becomes too large, potential and current density will vary along the distance away from the couple junction.

Figure 2. 8 shows the effect of varying the Wagner number (x/δ) on the distribution of current density across various galvanic couples (Waber and Rosenblunt, 1955). It is clear from Figure 2. 8 that current distribution becomes more uniform for Wagner number lower than 1.

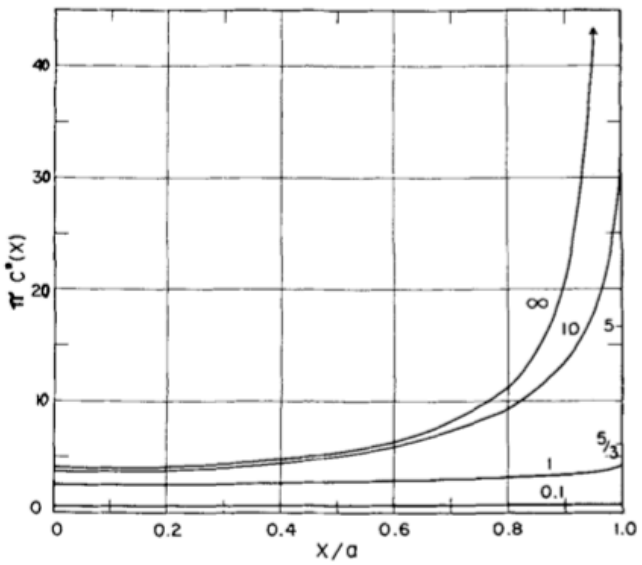

Figure 2.8 Effect of polarisation on the variation of anodic current density parameter. Curves are for different values of Wagner number (x/δ) (Waber and Rosenblunt, 1955)

2.5. Pitting Corrosion

Pitting is a localised form of corrosion, which results in small and deep cavities in the metal or alloy surface. It occurs on metals, under natural conditions, when the the mixed potential at the metal/solution interphase is higher than the pitting potential (NACE,2015). Pitting corrosion is influenced by a variety of parameters, including environment, temperature, alloy or metal composition, surface finish and heat treatment. Pit development occurs in stages. Once a pit nucleates, it is likely that a stable pit will grow. However, stable pits will not grow unless they survive the metastable phase. The formation of pits, including the metastable phase will be discussed below.

2.5.1. Stages of the Pitting

2.5.1.1. Pitting Initiation

The pit initiation process is perhaps the most disputed aspect of pitting phenomenon, as there are many different models that attempt to explain the initiation and formation of pits at the metal surface. It is believed that to nucleate pits on the surface of active-passive metals or alloys, local dissolution followed by breakdown of the passive film must occur first. Theoretical models, which support the above claim, have been classed in three main groups (Kruger, 1976): a) aggressive ions migration and contamination of the passive film, b) adsorption of aggressive species and c) mechanical breakdown model (Figure 2.9).

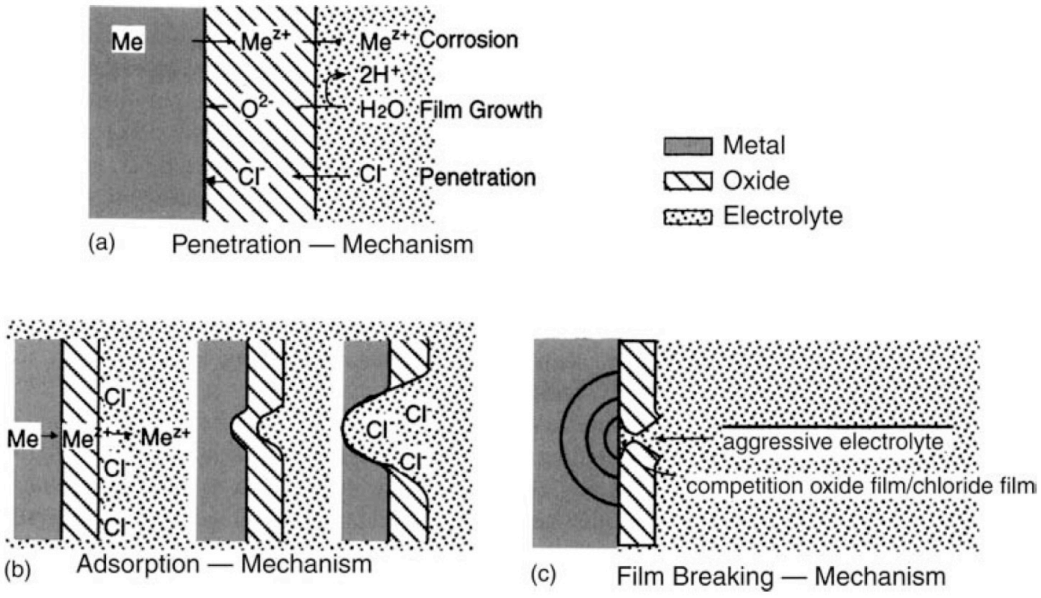

Figure 2.9 Model of pit initiation leading to passive film breakdown (Ed.Revie, 2011: 161)

a) Penetration Mechanism

This theory suggests that aggressive ions (e.g. halogens) are incorporated into and migrate through the passive film to the metal/film interface where they participate in the destruction of the passive film. The penetration mechanism is still not well understood. However, there is evidence for chloride ions penetrating through the passive film on aluminium (Macdonald, 1992 and Natishan et al., 1999).

b) Competitive ion adsorption Mechanism

In the ion adsorption mechanism, aggressive ions first absorb around a cation in the passive film surface and then form high-energy complexes, which lead to local dissolution, thinning and breakdown of the passive film (McCafferty, 2010: 285).

c) Film Breakdown Mechanism

This theory suggests that the adsorption of aggressive ions on the film/solution interface causes mutual repulsion of the adsorbed charged species. When the repulsive forces are high enough, electrochemical breakdown of the passive film occurs (McCafferty, 2010: 285). On the other hand, there is also abundant experimental evidence suggesting that pits nucleate at pre-exsisting physical defects or chemical heterogeneities at the surface of the metal such as flaws, scratches, non-metalic inclusions, grain boundaries and second-phase particles. (Frankel, 1998).

2.5.1.2. Metastable Pits

Metastable pitting is an unstable pit that nucleates below the pitting potential and grows during the incubation time but re-passivate before stable pits start growing (Frankel, 1998). Metastable pitting has been observed as the transient fluctuaction of the current under potentiostat control (Figure 2.10). Each current spike reflects the formation, growth and repassivation of a metastable pit. The lifetime of metastable pits is very short, lasting typically less than 5 seconds (Joubert, 1988:13).

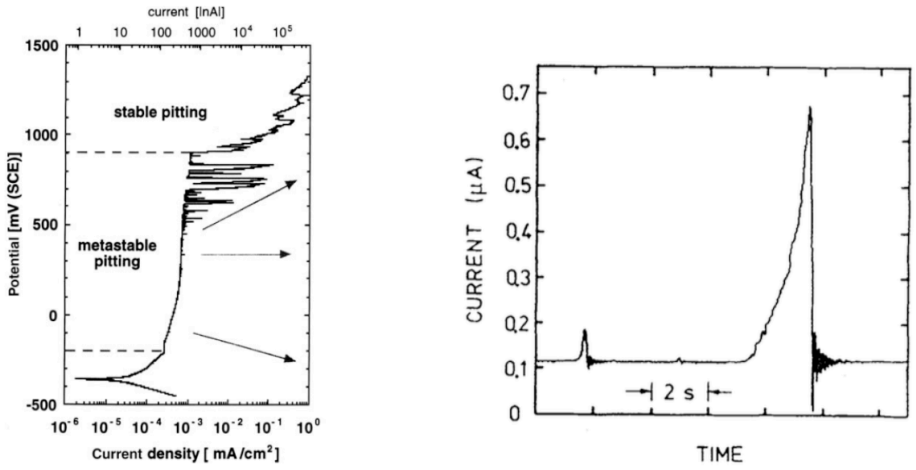

Figure 2.10 Potential-current and current-time curves of stainless steel showing different stages of localised corrosion (Ed.Revie, 2011:160)

Metastable pits in stainless steel are formed due to the dissolution of active inclusions, which remain open but repassivate (Burstein, Pistorius and Mattin, 1993). According to Frankel et al.,(1987), metastable pits develop underneath porous layers, which are a remnant of the passive film. Destroying such porous layers during metastable growth leads to repassivation of the pit (Figure 2.11). Understanding metastable pit formation is extremely important because whether pits repassivate at the metastable stage or grow to become stable pits, they all start as metastable pits (Pistorius and Burstein, 1994).

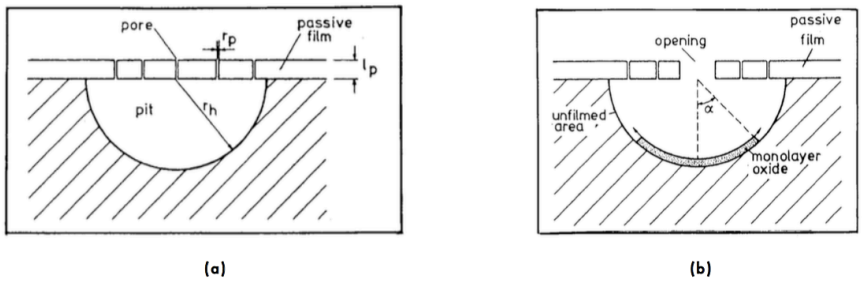

Figure 2.11 a) Metastable pit development underneath a porous layer b) Pit repassivation due to destruction of a porous layer (Pistorius and Burstein, 1994)

2.5.1.3. Pit Growth

a) Metal Dissolution Hydrolysis

This approach suggests that the main cause of pit propagation is a localised acidification inside the pit, due to metal hydrolysis. Studies have been conducted, which reveal that inside a pit or crevice, the solution has a different composition and pH from the bulk solution. According to Galvele (1976), a stable pit will grow if the relationship between potential and

current density inside the pit obeys a logarithmic law , then, there will be a critical potential below which pit growth will not occur because the acidification inside the pit will result in a pH below the critical pH value.

b) Salt Film Formation

This model assumes that a necessary condition for a stable pit growth is the formation of a salt film at the bottom of the pit, which obstructs the repassivation of the pit. The dense pore free salt film is composed of cations of the metal and aggressive ions from the solution (Frankel et al., 1987). The rate of salt film dissolution dictates the rate at which the pit grows (Szklarska-Smialowska, 1999).

c) Diffusion Controlled

In this model the pit growth stage is thought to be controlled by a diffusion process. During the metastable phase, the diffusion barrier is provided by the porous layer over the pit mouth and the pit depth. Pit growth reaches stability when the product of the growth current density and the radius of the pit equals 3 mA/cm. At this stage the pit propagates in the absence of the porous layer and " the diffusion barrier is provided by the depth of the pit itself, and this condition enables the pit anolyte to maintain the saturated metal salt concentration necessary to sustain metal dissolution" (Burstein et al., 1993).

2.5.2. Pitting Potential

The tendency for a metal alloy to undergo pitting when immersed in chloride solutions including seawater is characterised by means of the pitting potential. Stable pits will not grow at potentials lower than a certain characteristic potential. The effect and significance of this potential on pitting corrosion can be best understood with the empirical schematic polarization curves shown in Figure 2. 12. In the absence of chloride ions and/or temperature variation, the passive film at the alloy surface remains intact up to the transpassivation potential or oxygen evolution. However, in the presence of chloride ions and with the variation of solution temperature, the passive film breaks down locally and stable pits start growing at the pitting potential (E_{pit}).

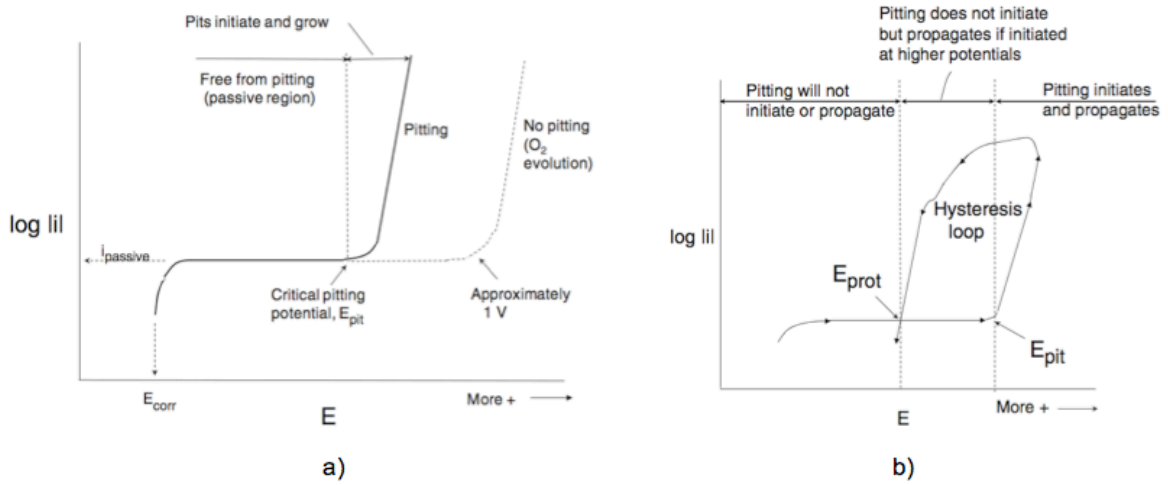

Figure 2.12 Schematic of polarization curve showing a) the critical pitting potential and b) pitting potential and pitting protection potential (McCafferty, 2010)

When the potential scan is reversed, the current density decreases with decreasing potential until the reverse curve intercepts the forward curve in the passive region (Figure 2.12). The sample potential at this intersection is called the protection potential (E_{prot}). If the sample potential were to remain below its protection potential, then there is a very slim chance that pitting will occur at all (Frankel, 1998). The hysteresis loop formed on the reversal scan provides information about the susceptibility to pitting and the ability of the passive film to repair itself. Generally, the presence of a hysteresis loop on a cyclic polarization curve implies pits have initiated in the sample and the passive film can't repair itself. The less the hysteresis, the more resistant is the alloy to pitting corrosion (Tait, 1994: 67).

2.5.3. Effect of Chloride Ions on Pitting Potential

Passive layers on stainless steels and nickel-based alloys can be destroyed by certain chemical species. The chloride ion is the most common of these and is found in many salt solutions. Through the analysis of the transport process inside a pit, Galvele (1976) observed that the critical pitting potential is a linear function of the logarithm of the chloride ion concentration:

$$E_{Pit} = a + b\log[Cl^-] \qquad \text{(Equation 23)}$$

where a and b are constants and $[Cl^-]$ is the chloride ion concentration.

2.5.4. Effect of Temperature on the breakdown potential

The influence of temperature on the breakdown potential of iron, aluminium, nickel, titanium and their respective alloys has been investigated in chloride solution. The term breakdown potential refers to the potential at which corrosion in general starts, because, from polarization curves, it is not always possible to distinguish when the corrosion is pitting, crevice or intergranular, or if the current density increases due to the transpassive dissolution. Szklarska-Smialowska (1971) has found that for type 430 and 304 stainless steel, there is a linear relationship between temperature and breakdown potential in the temperature range 30 to 100°C (Figure 2.13). An increment of temperature by 10 °C shifts the breakdown potential toward more active values by 30 mV.

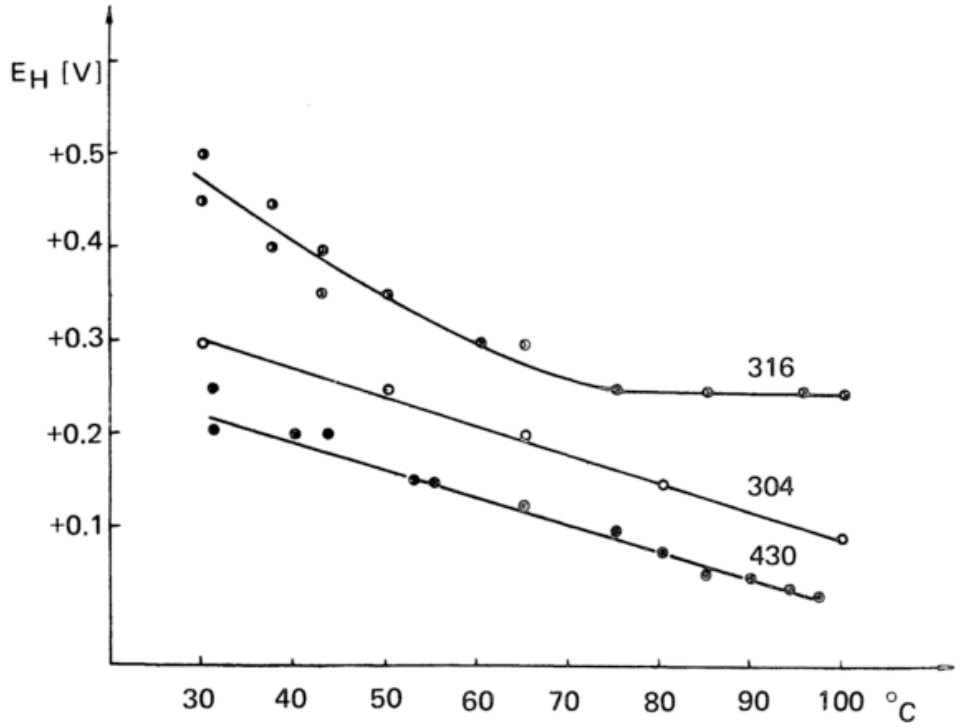

Figure 2.13 Breakdown potential of 430, 304 & 316 steels at 30 to 90 °C in 3% NaCl solution (Szklarska-Smialowska, 1971)

However, for type 316 stainless steel, the relationship between breakdown potential and temperature is not linear. With increasing temperature, the breaking down potential decreases until 70 °C, where it remains constant. This particular behaviour of 316 stainless steel could be attributed to the presence of molybdenum in the alloy composition.

Brigham (1972) measured a series of polarisation curves for various molybdenum containing austenitic stainless steels at different temperatures. A plot of the breakdown potential versus temperature produced curves with three distinct regions (Figure 2.14), which the author named as low, transition and high temperature regions. Brigham (1972) also observed that in the intermediate region for each alloy there is an unique temperature below which the alloy is immune to the initiation of pits and above which the alloy suffers pitting when exposed to an oxidising chloride solution such as $FeCl_3$. This temperature is called **critical pitting temperature** (**CPT)** and is the most accurate method to ascertain the temperature below which alloys are resistant to pitting.

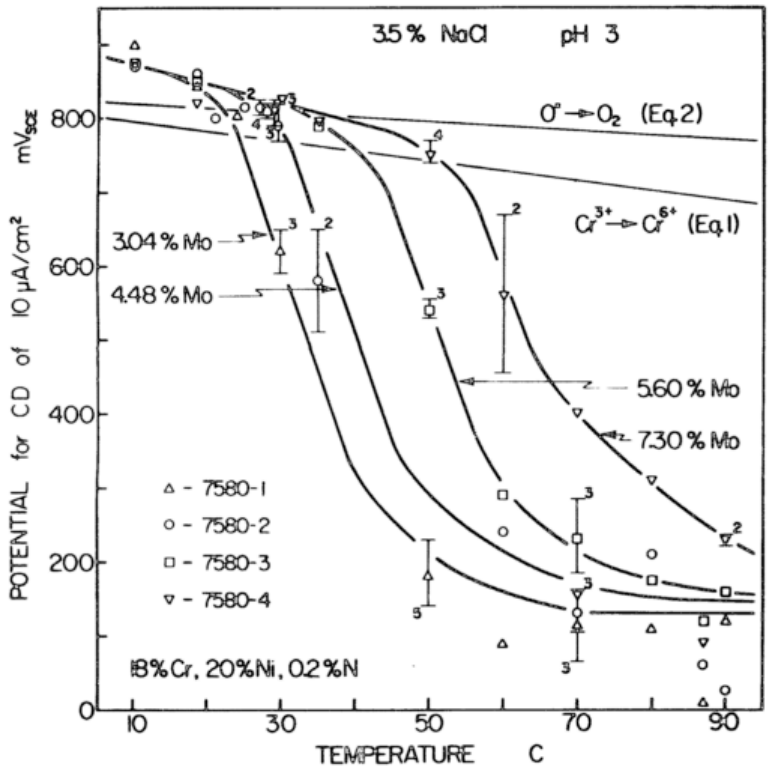

Figure 2.14 Effect of Mo and temperature on the breakdown potential of series of austenitic stainless steel (Brigham and Tozer, 1973)

Szklarska-Smialowska (2005: 23) believes that the number and size of pit initiation sites in the samples control the slope of the curves in Figure 2.14. When the sample has many pit initiation sites of different sizes and properties, then slope of the curves will be gradual or gentle and the critical pitting temperature will fall within a wider range of temperature. On the other hand, Brigham and Tozer (1973) have observed that extrapolating the anodic polarisation curves in Figure 2.14 to slower scan rate, the slope of the curves would rotate toward the vertical line. Consequently, an intermediate potential will be revealed in which the critical pitting temperature of an alloy does not vary with potential (Figure 2.15).

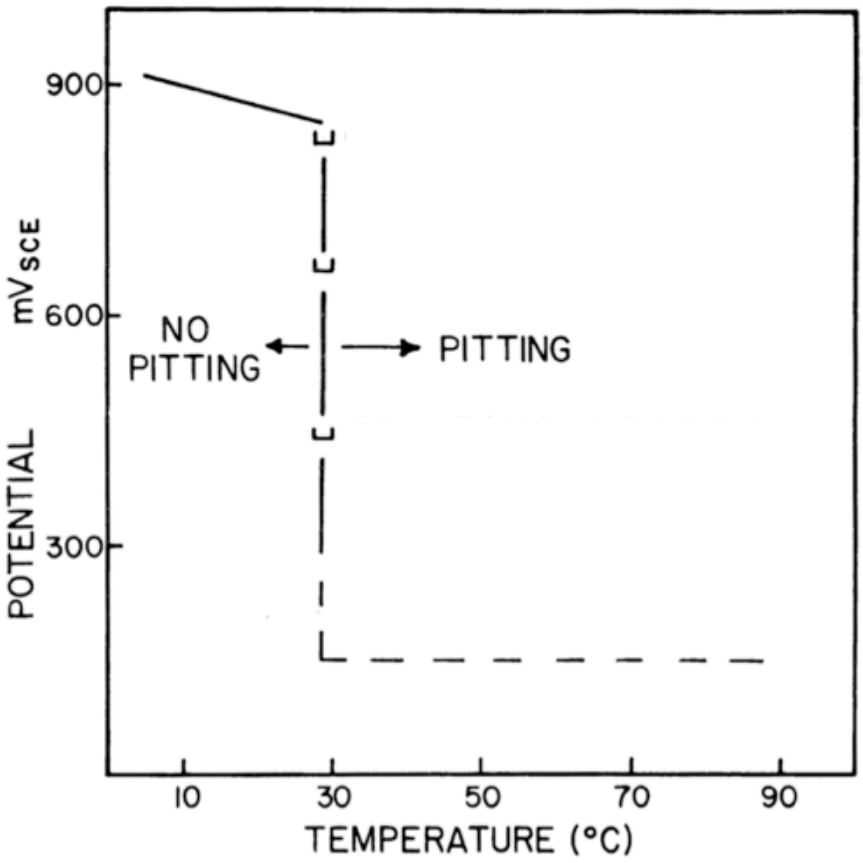

Figure 2.15 Schematic of the effect of slow scan rate on the slope of graph Breakdown Potential vs. Temperature.

2.6. Corrosion Resistance of Solid Solution Nickel-Based Alloys 825 and 625

Alloy 825 is an austenitic solid solution strengthened Ni-Fe-Cr alloy with minor additions of molybdenum, copper and titanium (Table 2.3). Technically alloy 825 is an iron-based alloy with very high concentration of nickel and it normally exhibits corrosion properties intermediate between stainless steels and Ni-Cr-Fe alloys (DuPont, 2009: 48). The outstanding corrosion performance of alloy 825 can be attributed to the high concentration of Cr, which provides excellent corrosion protection through the formation of passive films at the surface of the alloy. In both reducing and oxidizing environments, the alloy resists general and localised corrosion. It is a versatile alloy with application in a wide variety of corrosive environments, including chemical and petrochemical processing, pollution control, oil and gas recovery, acid production, nuclear fuel reprocessing, and handling of radioactive wastes (ASM International, 1990:1390).

Alloy 825 has good weldability by all conventional weld methods. Therefore, many and varied components e.g. pipes, tees, necks, manifolds and storage vessels have been manufactured using standard welding techniques. However, the corrosion resistance of welds in solid solution strengthened alloys is lowered following welding. This fact can be attributed to micro-segregation, formation of second phase particles, inclusions and porosity in the fusion zone (DuPont, 1996: 48). These weld defects can lead to localised corrosion.

Alloy	UNS	Ni	Fe	Cr	Mo	Mn	Al	Others
Iron-Nickel-Chromium Alloys								
800	N08800	30-35	Bal.	19-23		1.5	0.6	Si 1 Ti 0.15-0.60
800H	N08801	30-35	Bal.	19-23		1.5	0.6	Si 1 Ti 0.15-0.60
800HT	N08811	30-35	Bal.	19-23		1.5	0.6	Si 1 Ti 0.15-0.60
825	N08825	38-46	Bal.	19.5-23.5	2.5-3.5	1.0	0.2	Si 0.5 Ti 0.6-1.2
Welding Electrodes and Rods								
FM65	N08065	38-46	22.0 min	19.5-23.5	2.5-3.5	1.0	0.20	Cu 3 Ti 0.6-1.2
230-w	N06231	Bal.	3.0	20-24	1-3	1.0	0.3-0.5	Co 5.0 W 13-15
625	N06625	58.0 min	5.0	20-23	8-10	0.5		Nb 3.15-4 Ti 0.4

Table 2.3 Composition of some solid solution nickel-based alloy (DuPont et al., 2009:49)

Post weld heat treatment (PWHT) and pickling are normally necessary to improve the fusion zone corrosion resistance. However, these procedures are often not an option for field fabrications if the dimensions of the components being manufactured are too large. An alternative approach to PWHT is to use filler metals that match or exceed the corrosion resistance of the base metal. Filler metals 625 and FM65 are the preferred “over-matching composition” welding products for alloy 825 (Paul et al., 2004 and DuPont et al., 2009:54). The higher alloy element content of these weld products offset the effects of elemental segregation in alloy 825 weldments, which can result in preferential weld corrosion (Crum and Kiser, 2000). This approach may eliminate elemental segregation and the formation of second phase particles but it does not address all the defects associated with poor welding.

2.7.1. Intergranular Corrosion

Alloy 825 has been found to be susceptible to intergranular attack. However, very few studies exist on the intergranular corrosion of alloy 825. Raymond (1968) has conducted one of these studies on the mechanisms of sensitization[2] and stabilization of alloy 825. He found that the main reason for the intergranular corrosion susceptibility of alloy 825 is the precipitation of chromium carbides and the formation of chromium depleted areas adjacent to the grain boundary. According to the author, heating alloy 825 into its sensitizing temperature range (649 - 760°C) causes intergranular corrosion because of the precipitation carbides of type M_7C_3 and $M_{23}C_6$ in the grain boundaries.

On the other hand, partial stabilization against intergranular corrosion of alloy 825 can be achieved by the addition of titanium to the alloy composition. Titanium has a higher chemical affinity with carbon, nitrogen and oxygen than chromium, iron and molybdenum. Therefore, it will encourage the precipitation of titanium carbonitride before precipitation of M_{23} carbonitride, thus avoiding chromium and molybdenum depletion zones. However, addition of titanium to alloy 825 as the sole stabilization agent has not proved to be effective, especially when the 825 is heated into its sensitizing temperature range (Raymond, 1968).

Heat treatment above the sensitizing temperatures (annealing) followed by water quenching also avoids sensitization and intergranular corrosion in some austenitic stainless steels and nickel base alloys. Nevertheless, non-sensitized (that is, annealed) alloys can still be susceptible to intergranular attack in strongly oxidizing solutions (Henthorne, 1972: 79). The reasons for this kind of attack remain unclear. However, it can be argued that the intergranular corrosion susceptibility of annealed alloys depend on the properties of their grain boundaries. These are high-energy regions that collect drained point defects, precipitated second particles and segregated elements or impurities (Kasparova, 2000). Therefore, upon exposure to very strongly oxidising solutions, the chemical and physical difference between grain boundaries and the grains serve as the driving force for intergranular corrosion.

[2] The term sensitization refers to the heat treatments that may make the alloy susceptible to intergranular corrosion

2.7.2. Effect of Experimental, Environmental and Compositional Factors on the Breakdown Potential

There are very limited data available on the influence of experimental, environmental and compositional factors on the breakdown potential of alloys 825 and 625. Manning (1980) has investigated the effect of potential scan rate on the pitting potential of various high performance alloys (including alloy 825) in acidic chloride solution. He concluded that pitting potentials determined by scan higher than 0.36 V/hour are strongly influenced by experimental procedural changes. On the other hand, Dunn et al., (1996) have measured pitting and repassivation potential of alloy 825 as a function of surface finish and amount of cold work in a strongly alkaline water. They found out that increasing the surface roughness of the material , decreases the pitting potential by 100 mV. Cold work had no measurable effect on the pitting potentials.

2.7.3. Pitting Corrosion: Critical Pitting Temperature (CPT)

Critical pitting temperature (CPT) for various nickel-based alloys, have been determined using different tests techniques. McCoy et al. (2013) measured the CPT of alloys 825 and 625 using ASTM G48 method C (Table 2.5). This method was designed to rank the relative pitting resistance of stainless steels and nickel-based alloys for seawater applications.

Alloy	CCT (ºC)	CPT (ºC)
Inconel Alloy 686	>85	>85
Inconel alloy C-276	>45	>85
Inconel alloy 725	35	>85
Inconel alloy 625	30 - 35	≥85
Incoloy alloy 25-6MO	30 - 35	65 - 70
Duplex Stainless Steel 2205	20	30
Incoloy alloy 825	5	30
316 Stainless Steel	<0	15

Table 2.4 Critical Crevice & Pitting Temperature for various nickel alloys (McCoy et al.,2013)

Several exceptions have been reported concerning successful correlation between the performance of alloys in the ASTM G48 method C test solution (6% $FeCl_3$) and performance in certain environments, such as natural seawater and chloride containing environments (Garner, 1981 & Steinsmo et al., 1997). However, these should not be used to measure the critical pitting temperature of any metal or alloy in seawater. One of the reasons could be attributed to the test conditions used by ASTM G48 method. For example, ASTM G48 test solution (6% $FeCl_3$) is very severe due to its extremely low pH of 1.5 and very high oxidizing

power. Therefore, very low, critical pitting temperatures are measured (Ronge et al.,1992). These test conditions do not represent any real service environment.

There are more reliable electrochemical techniques, which have been used to determine CPT, which are potentiodynamic (Brigham and Tozer, 1973, Qvarfort, 1989) and the potentiostatic method (Salinas-Bravo and Newman, 1994). The potentiodynamic method consists of measuring potentiodynamic polarization curves at different temperatures and plotting the breakdown potential vs. temperature. CPT is the temperature where the breakdown potential falls sharply from transpassive to pitting corrosion. To get a more accurate result using this method, an Avesta cell[3] is required to prevent the test results from being affected by crevice corrosion. In the potentiostatic method, "the sample is polarised at a fixed anodic potential, more noble than any possible breakdown potential, in an aggressive solution, the temperature of which is increased slowly and the CPT is the temperature at which a marked current increase is observed"(Ebrahimi et al., 2012). The heating rate in the potentiostatic method should be slow enough allow enough time for the incubation of stable pits and pitting initiates at high temperatures, otherwise, this method will produce an overestimation of the critical pitting temperature (Salinas-Bravo and Newman, 1994).

In this study, the effect of varying seawater temperature (30 to 60 ºC) on the breakdown potential of both alloys 825 and 625 will be investigated. Furthermore, the critical pitting temperature of alloy 825 and its weldment will be determined using a potentiodynamic method and the results will be compared to the result obtained from ASTM standard G48 (McCoy et al.,2013). The question as to whether or not the critical pitting temperature of alloy 825 and its weldment can be used to predict their performance in real seawater environment will be also addressed.

[3] The Avesta Cell is a special cell for pitting corrosion testing which prevents crevice corrosion at the crevice formed between the specimen and the mounting material.

CHAPTER THREE: EXPERIMENTAL PROCEDURES

3.1 Testing Samples

Chemical composition of alloy 825 and filler rod alloy Inconel[4] 625 are listed in Table 3.1. Alloy 825 samples were cut from a hot rolled and annealed plate, which was donated by Escova LDT (see Appendix A for the material certificate). Several filler rods of Inconel 625 were used to build up a fully welded alloy 625 sample. Alloy 825 samples were joined by TIG using Inconel alloy 625 filler material. The values of the welding parameters are shown in Table 3.2. The sample dimensions for metallographic examination, potentiodynamic polarization and immersion tests are summarised in Table 3.3.

	Composition (wt %)												
Elements	**C**	**S**	**Cr**	**Ni**	**Mn**	**Si**	**Mo**	**Ti**	**Cu**	**Fe**	**P**	**Al**	**Co**
N08825	0.012	0.002	22.6	39.7	0.78	0.26	3.09	0.73	1.90	30.4	0.017	0.15	0.15
N06625	0.10	0.015	23.0	58.0	0.50	0.50	10	0.40	0.50	5.0	0.02	0.40	-

Table 3.1 Chemical composition of alloy 825 and Inconel filler rod alloy 625

Welding Process	Voltage V	Current A	Heat input (kJ/min)	No. of Passes
TIG	10-12	125	1.98	2

Table 3.2 Welding parameters of Alloy 825 welds

Test	Sample Material	No of Sample	Sample Size
Potentiodynamic	Alloy 825	3	50 x 50 x 10 mm
	Alloy 625 (weld)	//	//
	Alloy 825 weldment	//	//
Immersion	Alloy 825 weldment	15	50 x 25 x 3 mm
Metallographic Ex.	Alloy 825	4	5 x 5 x 5 mm
	Alloy 625 (weld)	//	//
	Alloy 825 weldment	//	//

Table 3.3 Samples sizes and materials

[4] Inconel is a trademark of Special Metals Corporation group of companies

3.2 Sample Preparation

Except for the metallographic samples, the final surface finish for all test samples was obtained by mechanically polishing them with 180 grit paper. One day before each test, samples were rinsed with distilled water and dried in air. Samples for metallographic examination were prepared according to ASTM E3-11 (ASTM, 2011) and metallographic etching book (Petzow, 1999:118).

3.3 Metallographic Examination

All samples of Alloy 825 and alloy 625 weld of size of 5mm x 5mm x 5mm were hot mounted in Polyfast resin using a Struers hot mounter labopress-3 machine. The surface preparation and etching operation were completed according to ASTM E3-11 (ASTM, 2011) and Metallographic Etching book (Petzow, 1999:118).

3.4 Testing Solution

The solution for all electrochemical tests was prepared in accordance with ASTM D1141-98 (reapproved 2013), while the long immersion test was conducted in natural seawater collected at the Marine Biology Research Unit (UCT). The seawater analyses were performed at A.L. Abbott and Associates (PTY) LTD (see Appendix A). Table 3.4 lists the major ion composition and some properties of the seawater.

Constituents	Qty	Unit
Chloride (Cl^-)	20074	mg/l
Sodium (Na^{2+})	9800	//
Sulfate (SO_4^{2-})	2725	//
Magnesium (Mg^{2+})	1885	//
Calcium (Ca^{2+})	401	//
Potassium (K^+)	200	//
Bromide (Br^+)	22	//
Bicarbonate (HCO_3^-)	181	//
Fluoride	1.9	//
Strontium (Sr^{2+})	678	µg/l
Total Dissolved Solids	46067	mg/l
Total Alkalinity	148	//
pH (at 25°C)	7.07	
Conductivity (at 25°C)	6675	mS/m

Table 3.4 Composition of seawater: Major ions and some properties

3.5 Instrumentation

3.5.1 Microscopy

Light microscope images were all obtained from a Nikon Eclipse microscope (MA200), while images of the samples after electrochemical tests were captured with an iPhone 6 camera. Samples microstructures were analysed and photographed from a Nova nanoSEM 230 scanning electron microscope. The settings for SEM were: acceleration voltage (U_{acc}) =20 keV, magnification =1000 x, horizontal field width (HFW) =298 µm and working distance (WD) =5.0 mm.

3.5.2 Potentiostat & Temperature Controller

VersaSTAT 3 potentiostat and galvanostat together with the VersaStudio software package were used to perform potentiodynamic polarization experiments, as shown in Figure 3.1. The solution temperature was controlled externally by a thermo-regulated water bath. Polarization measurements were performed with an Avesta cell, which is a cell designed to avoid crevice corrosion between the specimen and the mounting material. A thermally insulated box was built to house the cell. This was used to maintain a more uniform temperature distribution within the testing cell. A thermocouple was placed near the surface of the specimen to monitor the temperature. A saturated calomel electrode and graphite rods were used as reference and counter electrodes respectively in the electrochemical test.

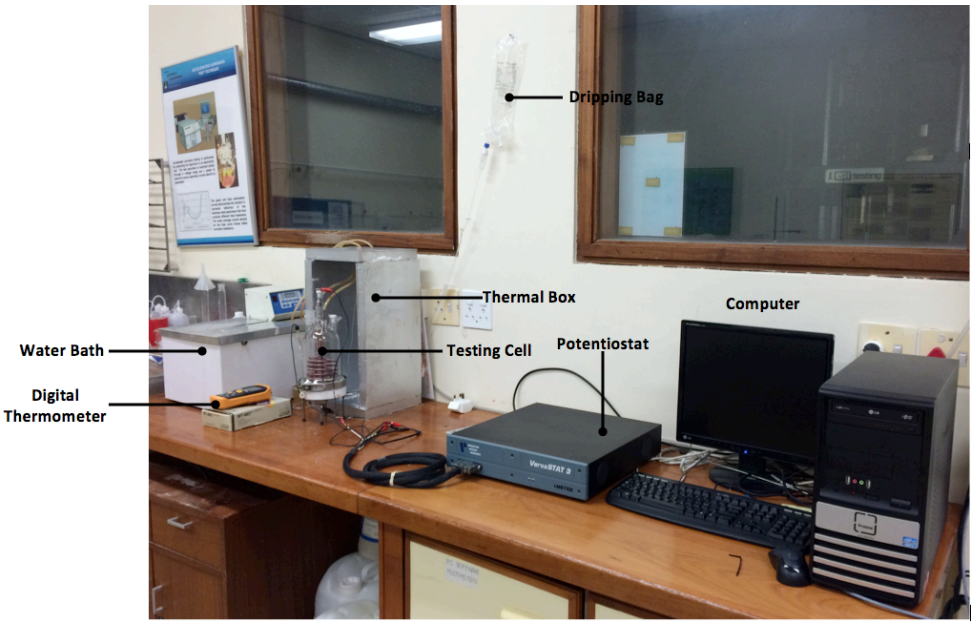

Figure 3.1 Laboratory test setup for potentiodynamic polarisation measurements

3.5.3 Thermo-Regulated Water Bath

Figure 3.2 shows one of thermo-regulated water baths (fish tanks and temperature controller), which was used to control the temperature of the Laboratory Immersion Test. Fifteen small and identical chambers were built from glass to accommodate the welded samples and the natural seawater.

Figure 3.2 Laboratory setup for immersion Corrosion test

3.6 Test Procedures

3.6.1 Potentiodynamic Polarization Measurements

3.6.1.1. Standard Test

In order to ensure that the Avesta cell and the Potentiostat were functioning properly, a reference test was performed on type 430 stainless steel samples according to ASTM standard G5-13 (ASTM, 2013). Figure 3.4 displays the test result, which is quite similar (shape and current range) to the curves presented in the ASTM standard G5-13 (ASTM, 2013).

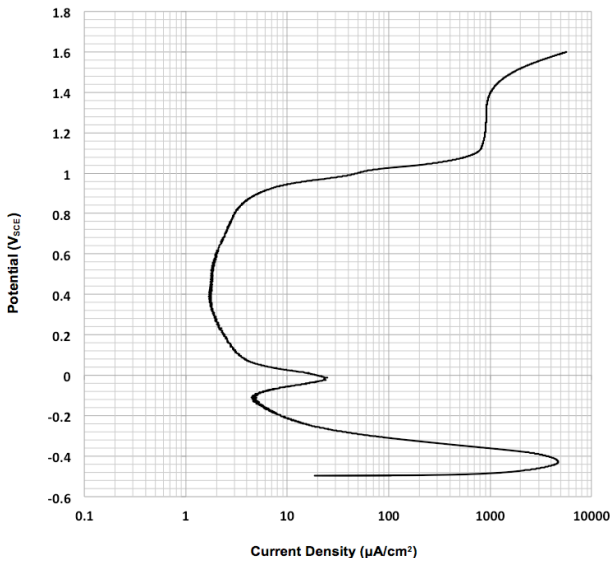

Figure 3.3 Potentiodynamic polarisation curve for Type 430 stainless steel in 1.0N sulfuric acid

3.6.1.2. Procedures

One day[5] before each potentiodynamic polarization test, a polished sample was immersed in synthetic seawater (at 25°C) to allow the sample's open circuit potential (OCP) to stabilize to a rate of change of less than 3 mV/min as recommended by ASTM F2129-06. The sample was transferred to the test cell and the solution temperature was raised to the target value. The test cell was open to the air to avoid oxygen depletion in the solution. The sample OCP or corrosion potential (E_{corr}) was recorded after one-hour of immersion in test cell. Afterwards, the sample potential was scanned at 0.1mV/s, from -0.3 mV_{SCE} below E_{corr} through to +1.2 V_{SCE} or until transpassivity is observed in the polarization curve. Tests at each temperature was repeated three or more times to ensure repeatability in the results.

3.6.1.3. Data Filtering and Smoothing

Figure 3.5 shows a raw polarization curve obtained from alloy 825 sample in seawater. All curves obtained from testing samples (alloy 825, 625 and weldment) were noisy in the cathodic branch as well as in the lower section of the anodic branch. In addition, a break in current density was also observed in all curves.

A Matlab function was used to reduce the noise level on the curves. The break in the corrosion current was a systematic error due to calibration of the potentiostat. As it had no physical significance, it was eliminated by shifting the curve at higher potential backwards to match the curve at lower potential (Figure 3.6).

Mathematical expressions were used to model a section of the alloys polarization curves near the (first) corrosion potential (Figure 3.7). By deconstructing the matched curves, the anodic and cathodic components are revealed and the corrosion parameters of the alloys can be determined (see Appendix C1).

[5] The author observed that a period shorter than 12 hours was not enough to allow the OCP of the samples to stabilize to the change rate of potential (3 mV/min) recommended by ASTM F2129-06. Therefore, samples were prepared and immersed in solution one day before there were tested.

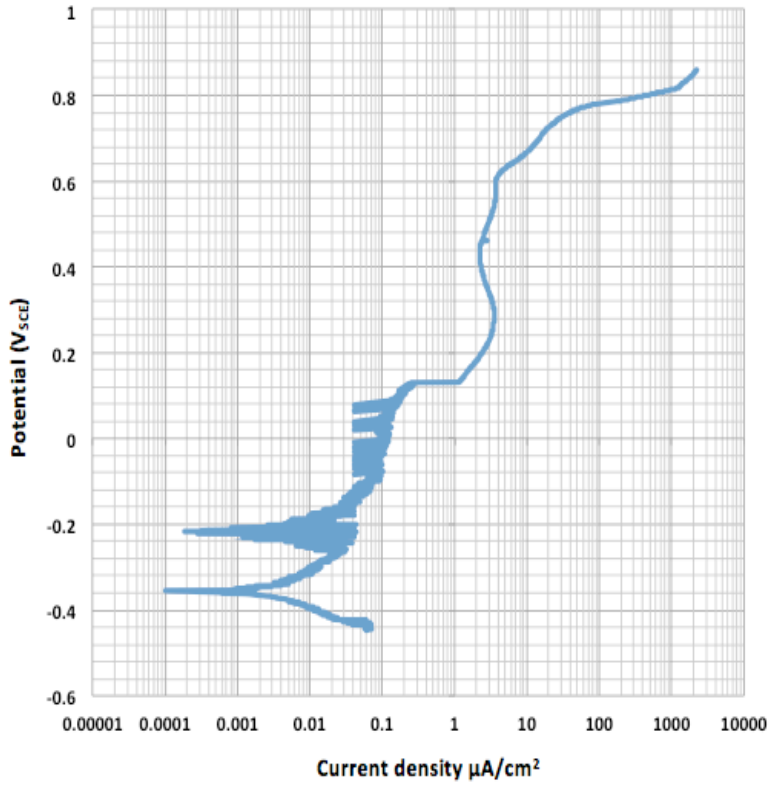

Figure 3.4 Raw potentiodynamic curve of alloy 825 obtained in seawater at 30°C

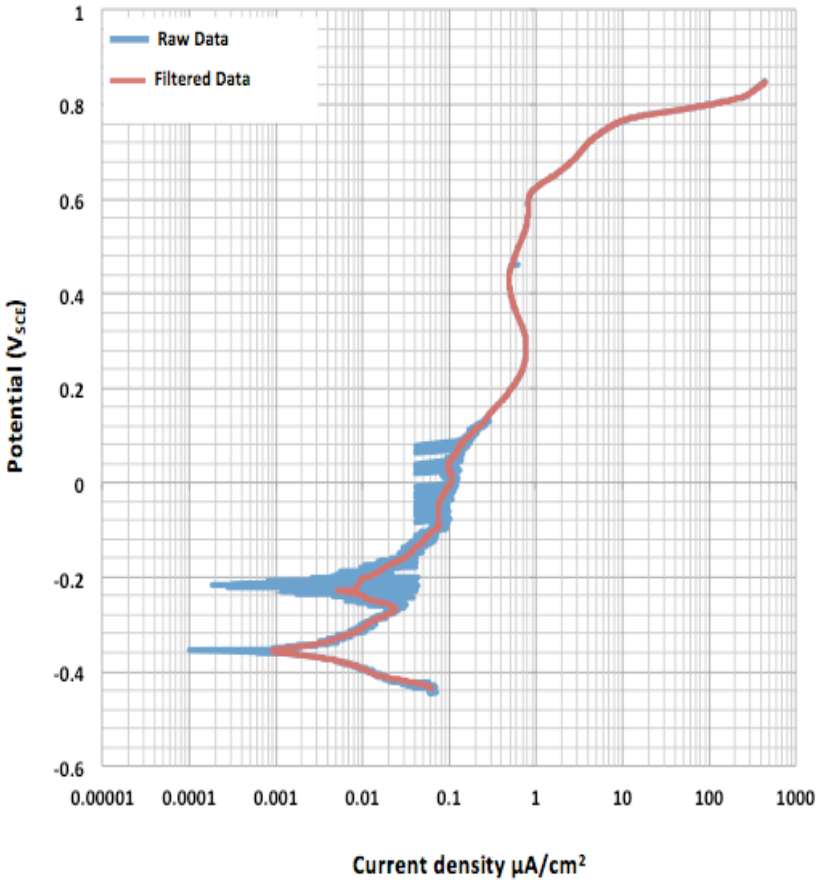

Figure 3.5 Raw and smoothed polarization curves of alloy 825 obtained in seawater at 30°C

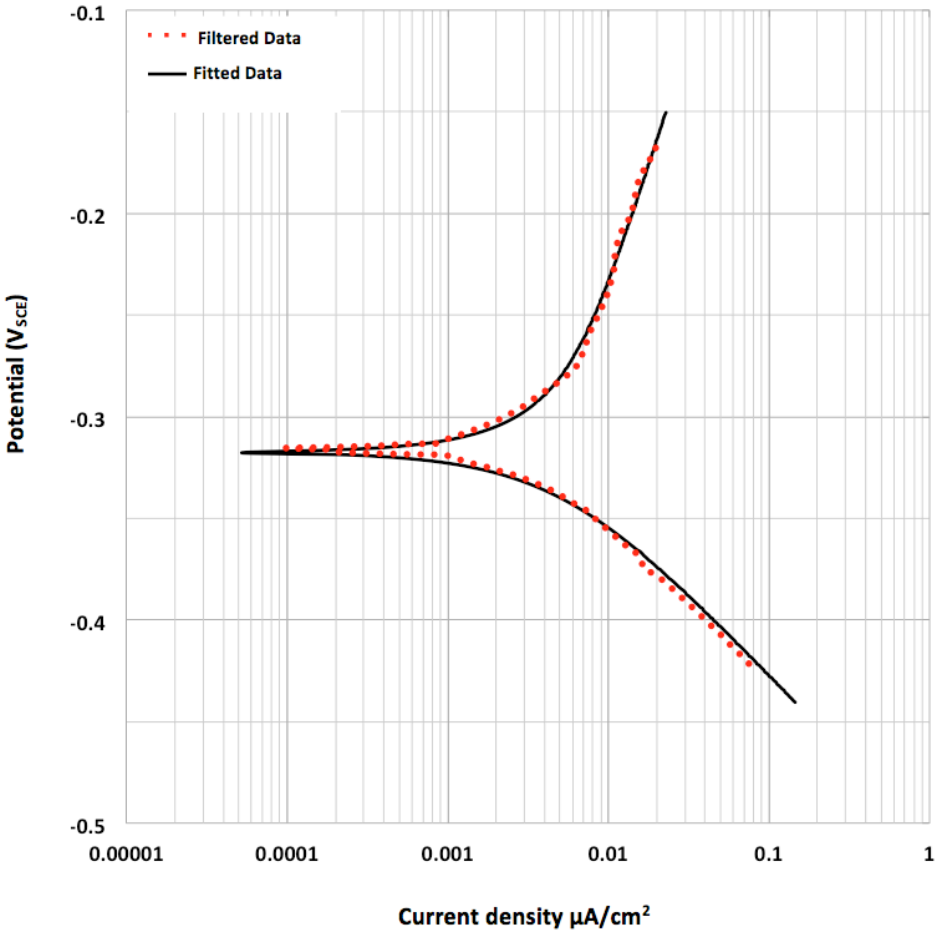

Figure 3.6 Filtered and matched section of alloy 825 polarization curve, near the open circuit potential.

3.6.1.4. Corrosion Potential and Current Density

A straight line fitted across approximately a decade of the linear portion of the measured cathodic curve will represent the Tafel[6] curve (Figure 3.8). The anodic branch of alloy 825 also shows some linearity but it is not an indication of the Tafel region because the anodic branch of the experimental curve represents the dissolution of various alloying elements. However, a reasonable estimation of the corrosion current density may be determined from the intersection of E_{corr} with the cathodic components of the matched curves (Flitt and Schweinsberg, 2010).

[6] Tafel behaviour is related to an oxidation or reduction of a single species only

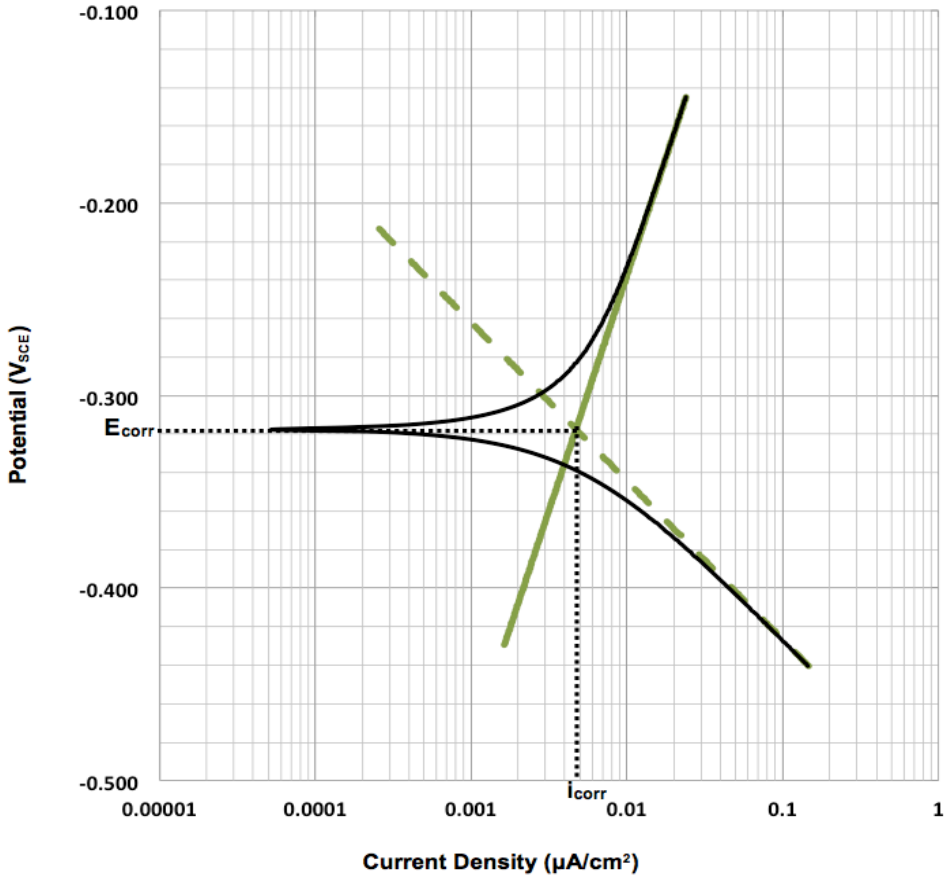

Figure 3.7 Matched polarization curve of alloy 825 near its open circuit potential plus its anodic and cathodic components.

3.6.1.5. Couple Potential and Galvanic Corrosion Current

Figure 3.9 shows the anodic and cathodic components for uncoupled alloys 825 and 625 weld. The area ratio of alloy 825 to alloy 625 in the weldment is 1.2 (Figure 4.17). Therefore, factor of 1.2 was used to adjust the current density of alloy 625 in the couple condition. According to mixed potential theory for two metals (Boboian et al., 1976: 7), when alloys 825 and 625 are coupled, the resultant galvanic potential of the system (E_g) is where the total oxidation and reduction components intercept. Since the alloy 625 weld is the anodic component in the couple, its corrosion current density increases to $i_{corr\ B'}$ and alloy 825 corrosion current density reduces to $i_{corr\ A'}$.

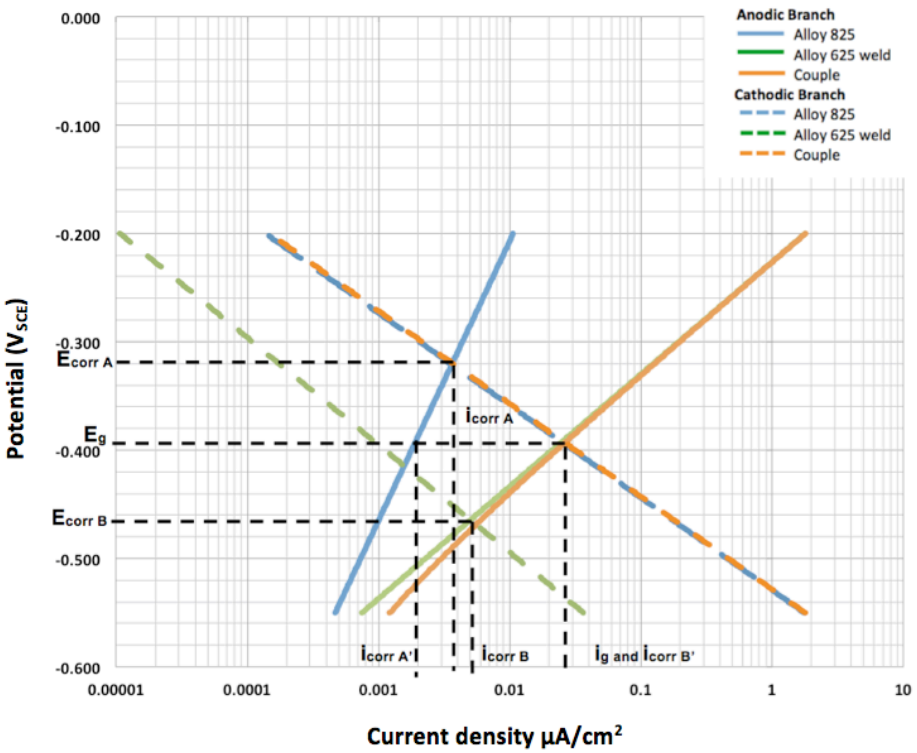

Figure 3. 8 Mixed potential theory applied on alloy 825 & 625 couple

3.6.1.6. Breakdown Potential and Critical Pitting Temperature

Three potentiodynamic polarization curves were obtained at each 5°C increment in the interval 30 - 70°C. Each curve exhibits a breakdown potential. In this work, breakdown potential (E_b) is defined as the potential at which the current density equals 10 µA/cm^2. E_b was plotted as function of the test temperature, which produced a reverse S-shaped curve. The onset of pitting resulted in a stepped decrease in potential (see sub-section 4.4.1). Therefore, CPT was in the temperature interval where E_b dropped from the high potential range to the low potential range.

3.6.2 Laboratory Corrosion Immersion Test

The laboratory corrosion immersion test was divided into two phases and each phase lasted for six months. First, all 15 welded samples were immersed in seawater and the temperature of the water bath was kept at 30 °C (Figure 3.2). After six months, samples were examined for pitting corrosion. Afterwards, samples were cleaned and in groups of 6 samples they were immersed again in seawater at different temperatures namely 50°C, 60 °C and 70°C.

CHAPTER FOUR: RESULTS AND DISCUSSION

4.1 Microstructure Characterisation

Figure 4.1 shows a polished surface of alloy 825 after 24 hours immersion in synthetic seawater. No corrosion attack was observed at the surface of the sample, which implies that passive layers might have formed and developed on the surface of alloy 825 due to exposure to the air. Chromium oxide (Cr_2O_3) and chromium hydroxide ($Cr(OH)_3$) are the main components of the passive layers formed on stainless steel and nickel-based alloys (Drogowska et al., 1998). On the other hand, the presence of chloride ions, in solution, affects the passive layer stability. It has been reported that the porosity of passive films increases in solutions containing chloride ions, due to formation of metallic chloride salts (Cardoso et al., 2008).

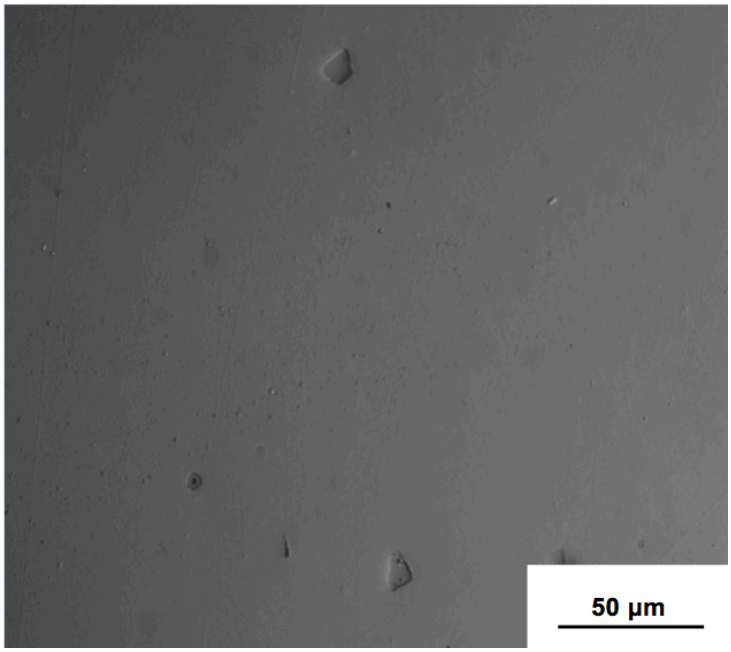

Figure 4.1 Polished surface of alloy 825 (with titanium inclusions) after 24 hours immersion in synthetic seawater

The microstructure of alloy 825 in hot rolled and soft annealed condition is shown in Figure 4.2. It comprises an austenite matrix (γ) with titanium carbo-nitride (TiCN) inclusions. The austenite phase exhibits grains with different sizes and most of the grains contain annealing twins probably formed during the recrystallization phase in the hot rolled process (Wang et al., 2015). Titanium is added to alloy 825 to prevent chromium depletion by forming titanium carbide of type TiC in preference to chrome carbides (Raymond, 1968).

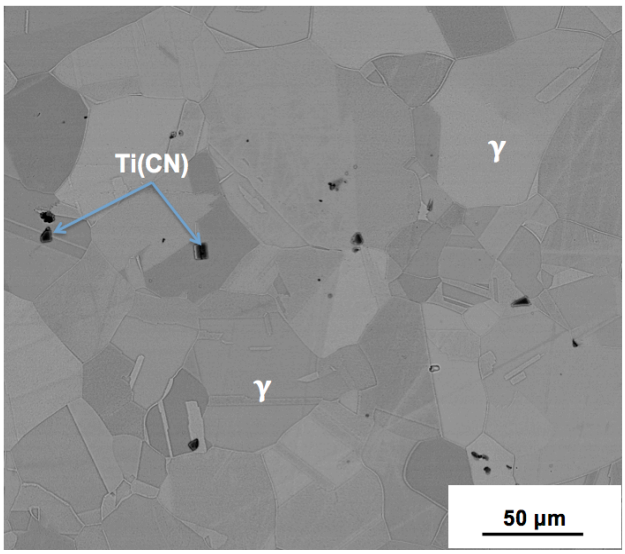

Figure 4.2 Microstructure of alloy 825 in hot rolled and annealed condition

Welding could be considered a casting process on a small scale. Therefore, the microstructure of alloy 625, in Figure 4.3, comprises coarse dendritic grains (Y) and fine interdendritic phases (laves phases). According to the work of DuPont (1996) and Silva et al. (2013), the alloy 625 weld micrsostrucutre exhibits strong segregation and consequently depletion of elements such as Mo and Nb in the dendritic regions, whereas elements such as Ni, Fe and Cr are slightly enriched in these regions. The variation in greyscale contrast in Figure 4.3 below is indicative of the variation of composition across the dendritic structure. The observed microstructure of alloy 625 is consistent with those reported by others (Cieslak et al., 1986, Cieslak, 1991), except that no solidification cracks were observed at the surface of the weld.

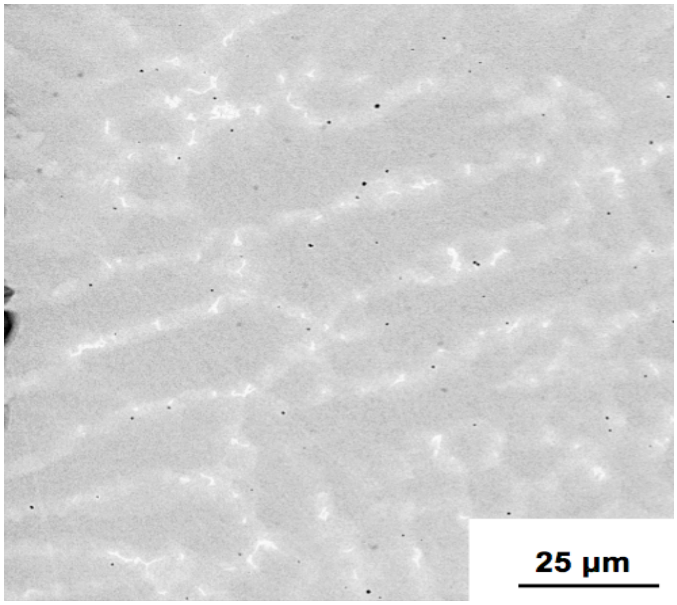

Figure 4.3 Microstructure of alloy 625 in weld condition

Figure 4.4 shows an alloy 825 weldment, which comprises alloy 825 as the base material (BM) and alloy 625 as the weld. The weldment exhibits three distinct zones, namely the fusion zone (FZ), heat affect zone (HAZ), and the unaffected base material (BM). Both alloys 825 (BM) and 625 (FZ) preserve their microstructures as shown in Figures 4.2 and 4.3. The HAZ also exhibits an austenitic microstructure but the grain sizes are smaller compared to the grains in BM. The microstructure in HAZ shows recrystallized grains, which is the inevitable effect of the heat of welding.

Normally, alloy 825 HAZ becomes sensitized during welding. Therefore, post weld heat treatment (PWHT) at a minimum of 1040 °C for one hour is recommended to dissolve any carbide, homogenize the structure and prevent intergranular corrosion in alloy 825 (DuPont et al., 2009: 55). However, in many cases, particularly in field fabrication, PWHT is not an option due to the enormous size of the components being welded. It is important to emphasize that often alloys are heated into their sensitization range during welding, but do not exhibit intergranular corrosion in service. This is true even if laboratory tests predict that intergranular attack may occur in the alloys (Henthorne, 1972).

The main purpose of this study was to evaluate the corrosion behaviour of alloy 825 and weldment under the service conditions. Therefore, post welding heat treatment was not considered.

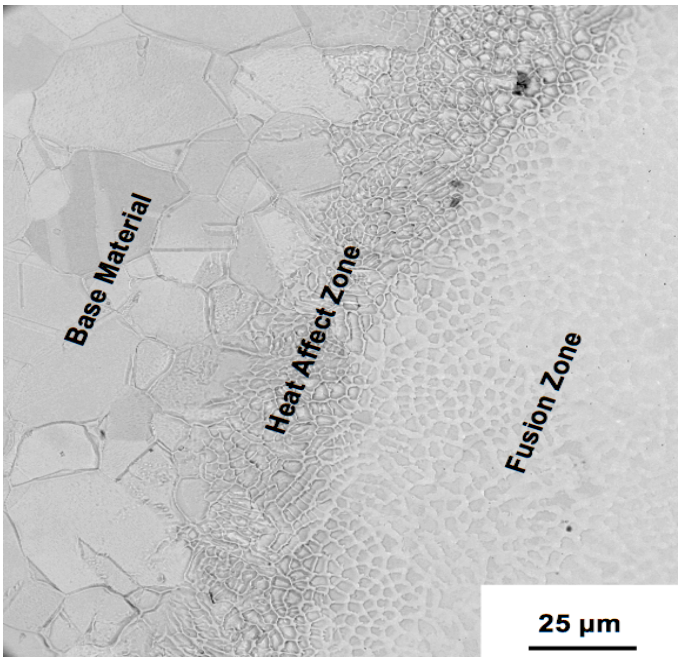

Figure 4.4 Micrograph of alloy 825 weldment showing the different microstructures

4.2 Effect of Temperature on the Uniform Corrosion Behaviour of alloy 825 and 625 Weld

The effect of temperature on the corrosion of alloys 825 and 625 weld was determined from their polarization curves using mixed potential theory (see Appendix C2). Table 4.1 summarises the uncoupled corrosion potentials, current densities and the rates of penetration for both alloys at different temperatures.

Although the values of corrosion potentials (E_{corr}) do not show a trend with temperature, they were observed to decrease very slightly with increasing in temperature (Figure 4.5). According to Cardoso et al.(2008) the corrosion potential of stainless steel and nickel-based alloys depends on the quality of the passive film formed at the surfaces of the alloys. In the presence of chloride solutions, temperature increases cause the passive film to become more porous due to the diffusion of chloride ions inside the film. Consequently, the passive film becomes less protective and the corrosion potential decreases (Carranza and Alvarez, 1996).

Alloy 625 weld appeared to be the more active metal of the pair, implying that when both alloys are electrically coupled, 625 will be the anode and will corrode more than 825. Theoretically, alloy 625 has greater corrosion resistance than alloy 825 due to its higher content of chromium and molybdenum (Al-Fozan and Malik, 2008). However, during welding, 625 filler metal is heated above its melting point and the solidification process always results in micro-segregation of alloying elements, which may reduce its corrosion resistance.

	T (°C)	30	40	50	60
Alloy 825	$E_{corr\ A} \pm \sigma$ (mV_{SCE})	-315 ± 7	-357 ± 1	-351 ± 21	-361 ± 46
	$i_{corr\ A} \pm \sigma$ (10^{-3} µA/cm^2)	3.97 ± 0.38	4.57 ± 0.19	5.44 ± 0.18	8.56 ± 4.04
	$r_A \pm \sigma$ (10^{-3} µm/yr)	40.3 ± 3.9	46.3 ± 1.9	55.2 ± 1.8	86.8 ± 41.0
Alloy 625	$E_{corr\ B} \pm \sigma$ (mV_{SCE})	-528 ± 55	-547 ± 21	-549 ± 6	-548 ± 23
	$i_{corr\ B} \pm \sigma$ (10^{-3} µA/cm^2)	6.43 ± 1.60	11.54 ± 0.40	12.84 ± 0.63	28.46 ± 18.60
	$r_B \pm \sigma$ (10^{-3} µm/yr)	65.2 ± 16.2	117.0 ± 4.1	130.2 ± 6.4	288.6 ± 188.6

Table 4.1 Corrosion potentials (E_{corr}), current densities (i_{corr}) and penetration rates (r) of alloy 825 and 625 weld at different seawater temperature

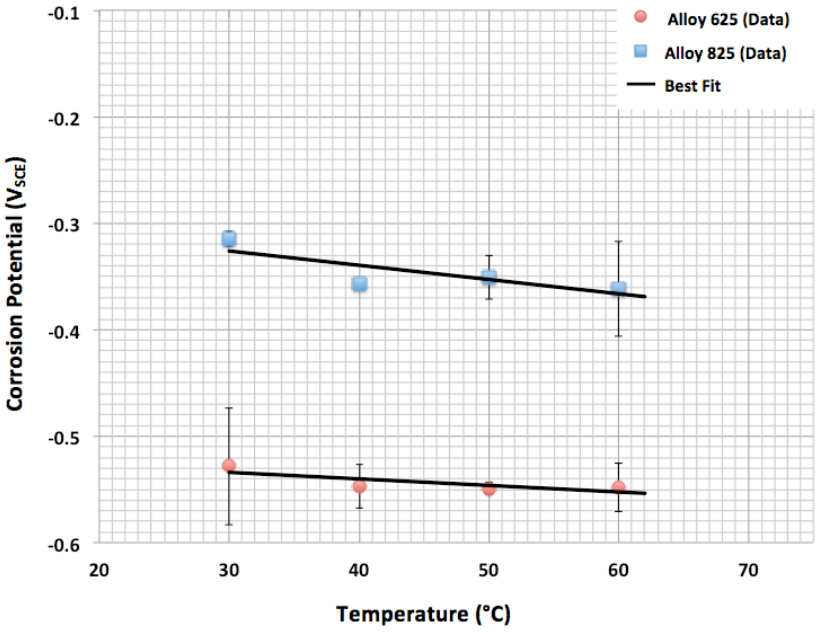

Figure 4.5 Influence of seawater temperature on the corrosion potential of alloys 825 and 625 weld.

Figure 4.6 illustrates how temperature affects the corrosion current density for both alloys. As expected, the corrosion current densities for alloys 825 and 625 weld were observed to increase as the temperature rose. This observation is entirely in agreement with Arrhenius equation (see sub-section 2.4.1). The graph in Figure 4.6 also reveals that the corrosion current density of 625 is more sensitive to temperature variation than 825. The reasons for the difference can be explained by comparing the activation energy (E_a) of both alloys.

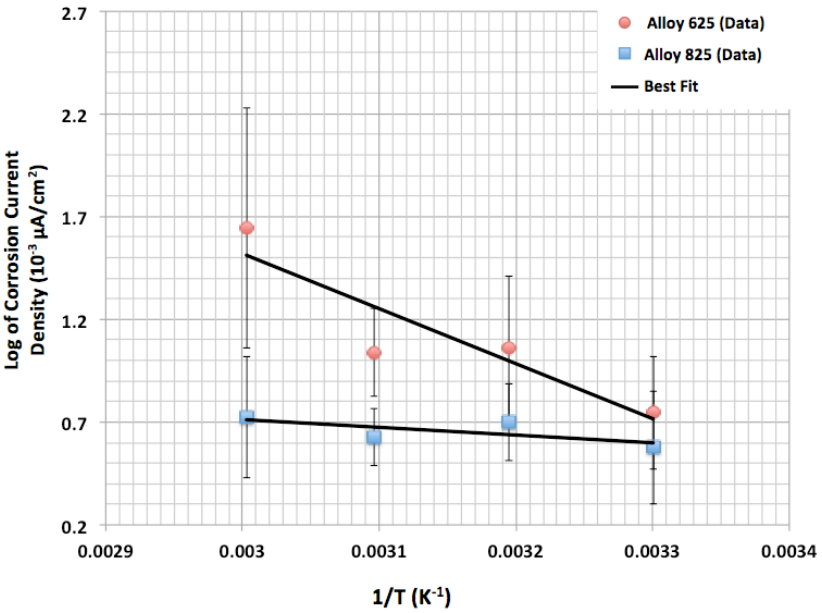

Figure 4.6 Influence of seawater temperature on the corrosion current density of alloys 825 and 625 weld

Activation energy (E_a) is one of the parameters of main interest in the kinetics of corrosion because it dictates the rate of corrosion (Trethewey and Chamberlain, 1998: 62). The calculated values of activation energies, from the slope of Log(i_{corr}) vs. 1/T graphs (see Appendix C4) for alloys 625 weld and 825 are 38.2 kJ/mol and 20.6 kJ/mol respectively. Clearly, alloy 625 weld has the higher activation energy, which implies that with change in temperature the variation of corrosion current density will be larger in alloy 625 weld than alloy 825.

The variation of corrosion penetration rate of alloys 825 and 625 weld as a function of temperature is shown in Figure 4.7. According to the typical corrosion penetration rates for nickel-based alloys listed in Table 4.2 (see sub-section 2.3.3), both alloys 825 and 625 weld exhibit outstanding resistance to uniform corrosion (< 25 µm/yr) in range of 30 to 60 °C. Such small penetration rates are also indicative of the existence of passive films with very low electronic conductivity at the surfaces of both alloys. In addition, these values are expected to decrease further as the passive film continues to improve gradually in a long-term. According to Evans (1960) and Abd El Kader and Shams El Din (1979), the interaction between the solution and the surface of passive metals promotes the healing and further thickening of the pre-formed oxide film. The growth of the oxide film will stop when the film acquires a thickness that is stable in the solution (Abd El Meguid and Abd El Latif, 2007).

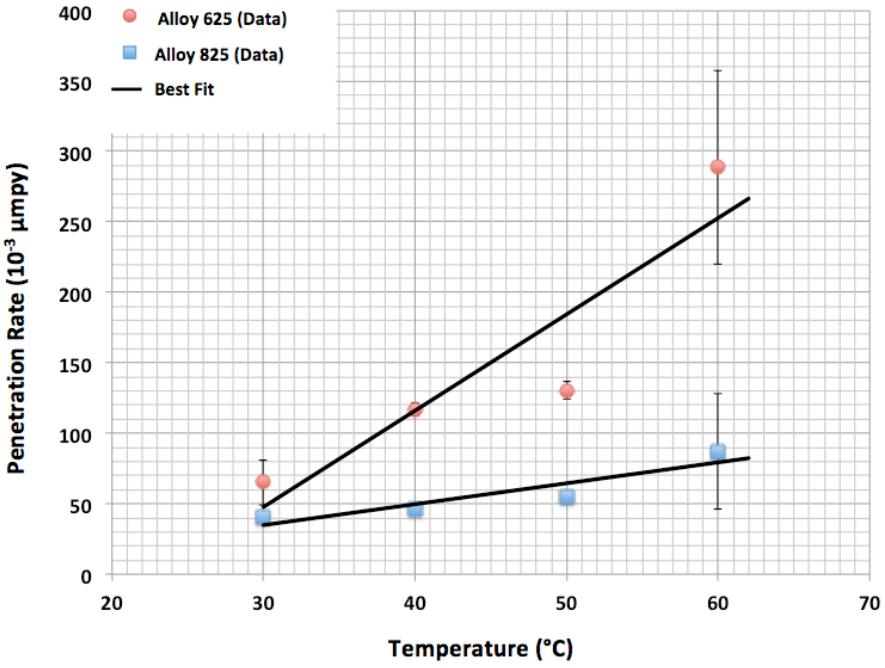

Figure 4.7 Effect of seawater temperature on the penetration rate of alloys 825 and 625 weld

4.3 Effect of Weld and Temperature on the Corrosion Behaviour of an Alloy 825 and 625 Couple

The previous section showed that individually, both alloys 825 and the alloy 625 weld exhibit outstanding resistance to uniform corrosion in seawater due to the existence of protective films at their surfaces. However, coupling two dissimilar alloys in a corrosive solution may increase the corrosion rate and destroy the protective film of the less noble alloy, exposing the substrate to localised corrosion (Baboian, 2005:370). In addition to the effect of the solution composition, high temperatures also have pronounced effects on galvanic corrosion.

4.3.1 Theoretical Predicted Galvanic Corrosion Data

The effect of coupling 825 to 625 filler metal (via welding) was also predicted from alloy polarization curves using the concept of mixed potential theory. Table 4.2 summarises the theoretically predicted galvanic potential and current density, rate of penetration and the relative dissolution rate of the alloys 825|625 couple at different temperatures. All the parameters in Table 4.2 were derived from the experimental data (see Appendices C3, D1 & D2).

	T (°C)	30	40	50	60
Coupled	$E_g \pm \sigma$ (mV_{SCE})	-422 ± 30	-449 ± 24	-442 ± 13	-440 ± 6
	$i_g \pm \sigma$ (10^{-3} µA/cm^2)	30 ± 7	111 ± 3	2579± 26	3096 ± 454
	$r_g \pm \sigma$ (10^{-3} µm/yr)	304 ± 71	1125 ±30	26150 ±271	31392 ±4603
Alloy 825	$i_{corr\ A'} \pm \sigma$ (10^{-3} µA/cm^2)	1.92 ± 0.58	0.49 ± 0.13	0.13 ± 0.09	1.69 ± 2.43
	$r_{A'} \pm \sigma$ (10^{-3} µm/yr)	19 ± 6	5 ± 1	1 ± 1	17 ± 25
Alloy 625	$i_{corr\ B'} \pm \sigma$ (10^{-3} µA/cm^2)	28.20 ± 4.07	117 ± 9	2477 ± 21	3097 ± 71
	$r_{B'} \pm \sigma$ (10^{-3} µm/yr)	286 ± 41	1186 ± 91	25116 ± 218	31402 ±720
Relative dissolution rate ($i_g/i_{corr\ B}$)		**4.65**	**9.64**	**200.86**	**108.80**

Table 4.2 Predicted galvanic potentials (E_g), galvanic current densities (i_g) and penetration rates (r) of the alloys 825|625 couple at different seawater temperatures

It was mentioned in section 3.6.1.5 that a factor of 1.2 was used to adjust the current density of alloy 625 weld due to the area ratio between alloy 825 and alloy 625 in the weldment. According to Oldfield (1988:15), cathode to anode area ratio in galvanic couple affects the corrosion rate of the anodic member. Figure 4.8 illustrates how temperature affects the galvanic potential and corrosion current density of the alloys 825|625 couple. The galvanic parameters of the couple respond to the temperature variation in the same way as the corrosion parameters of the individual alloys in their uncoupled conditions.

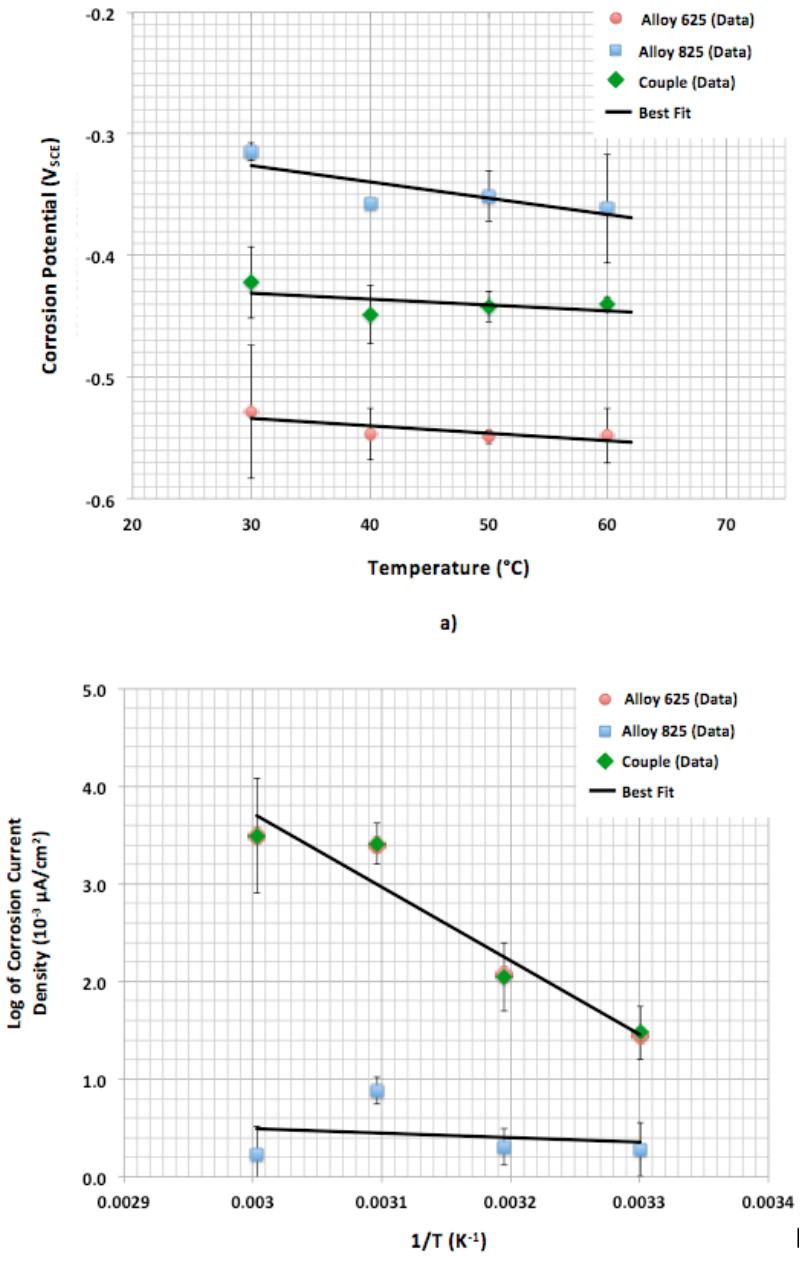

Figure 4.8 Influence of temperature on the a) Galvanic potential and b) current density of alloy 825|625 couple.

Coupling alloy 825 to 625 shifts the galvanic potential from the potentials of alloys 825 and 625 in the uncoupled condition (Figure 4.8a). The current density of alloy 625 increases and equals the galvanic current density while the corrosion current density of alloy 825 is significantly reduced (Figure 4.8b). According to Mansfeld (1971), the galvanic currrent density of a couple can be expressed as the difference between the partial anodic and cathodic current densities of the anode:

$$i_g = i_a - i^A_{corr} * \exp[-\frac{(E_g - E_{corr})}{b^A_c}] \qquad \text{(Equation 21)}$$

where i_g is the galvanic current density, i_a anodic current density at the anode metal in the galvanic couple, i^A_{corr} and E_{corr} are the corrosion current density and potential of the more active metal (anode) in the uncouple condition, E_g is the galvanic potential and b_c is the tafel slope of the cathode metal in the uncoupled condition.

Linking the Mansfeld (1971) expression (Equation 21) with the results obtained in the Figure 4.8, it becomes clear that the galvanic potential of the alloys 825|625 couple is larger compared to the more active corroson potential of alloy 625 (Figure 4.8a), such that the only contribution to the galvanic current comes from the anodic current density of alloy 625 (Figure 4.8b). Since the current density of alloy 825 in the galvanic couple is almost zero, it is reasonable to conclude that oxidation and reduction corrosion reactions take place at separated members of the galvanic couple,i.e. the only significant corrosion reaction occurring at the alloy 625 surface is oxidation and the only process occurring at the alloy 825 surface is reduction of O_2.

Table 4.3 summarises the effect of seawater temperature variation on the resistivity of seawater (R_W) and corrosion parameters of alloy 625, i.e. Tafel slopes (b_a & b_c), polarization resistance (R_P), Wagner polarization parameter (δ) and number (x/δ), where x, the critical dimension, is half of the width of alloy 625 (x= 2.5 cm). All the parameters (in Table 4.3) were derived from experimental data (see Appendix D3).

T	R_W	$b_a \pm \sigma$	$b_c \pm \sigma$	$R_P \pm \sigma$	$\delta \pm \sigma$	x/δ
°C	Ω/cm	mV	mV	Ω	cm	
30	17.28	46.67 ± 2.89	39.67 ± 3.51	377.96± 9.80	21.87± 0.57	0.11
40	14.74	40.33 ± 2.52	31.67 ± 5.86	312.85± 41.33	21.23± 2.81	0.12
50	12.84	27.33 ± 2.08	29.00 ± 2.65	247.85± 7.33	19.30± 0.57	0.13
60	11.38	27.67 ± 2.31	32.33 ± 2.08	263.72± 19.57	23.99± 1.72	0.11

Table 4.3 Seawater resistivity (R_W), alloy 625 Tafel slopes (b_a & b_C) and polarization resistance (R_P), Wagner parameter (δ) and number (x/ δ) at different temperatures.

The parameters of main interest, in Table 4.3, is the Wagner number (x/δ), because it determines whether the potential and current density across the surface of alloy 625 (anode), in the galvanic couple, will be uniformly distributed or varied along the distance away from the couple junction. Non-uniform distribution of galvanic parameters lead to localised attack of the more active member (anode) near the couple junction, where the current density is at highest (Baboian, 2005:370). Therefore it should be avoided. According to Waber and Rosenblunt (1955), (x/δ) equal or lower than 1 implies uniform distribution of the current and potential across a galvanic couple (see sub-section 2.4.3) . Data in Table 4.3 shows that at any testing temperature, the ratio (x/δ) is always below 1. Therefore, corrosion attack across the surface of alloy 625 weld in the galvanic couple will be uniform.

Figure 4.9 is a plot of the relative dissolution rate (i_g / i_{corr}) of the galvanic couple at different temperatures (see Appendix D2 for derivations). Mansfeld & Kenkel (1976: 20) have proposed the relative dissolution rate (i_g /i_{corr}) as a means to check the compatibility of dissimilar alloys in the galvanic couple. Where i_g is the galvanic current density and i_{corr} is the corrosion current density of the more active alloy in the galvanic couple (alloy 625weld). According to their criteria, relative dissolution rate below 5 implies compatibility, between 5 and 15 is borderline and above 15 alloys are incompatible. Unfortunately, these criteria do not apply for alloys 825 and 625 couple. The reasons will become clear after the introduction of Figure 4.10.

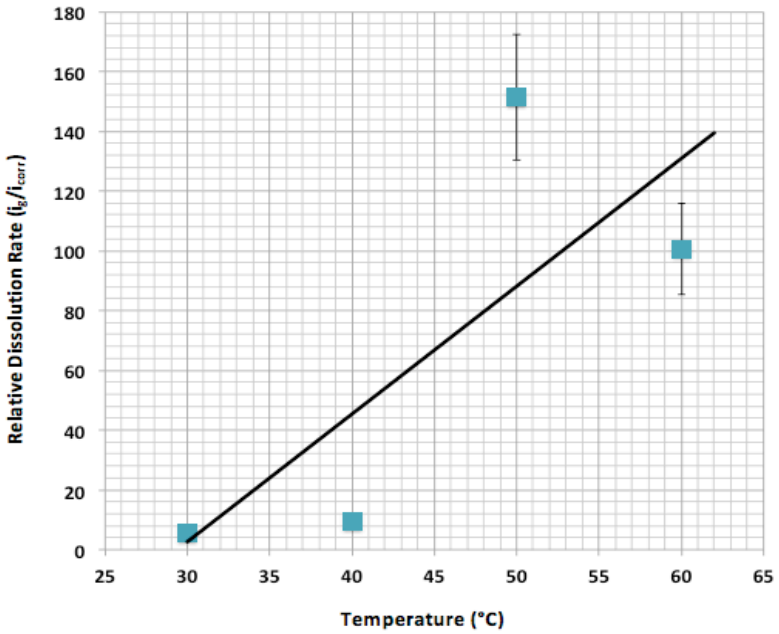

Figure 4.9 Effect of temperature on the relative dissolution rate of the alloys 825|625 couple.

Figure 4.10 illustrates the effect of temperature on the galvanic penetration rate and alloy 625 penetration rate in the couple condition. Again, according to the typical corrosion penetration rates for nickel-based alloys listed in Table 2.2, alloy 625 weld (in the couple condition) still exhibits resistance to uniform corrosion which varies between outstanding (< 25 µm/yr) at temperature below 50 °C and excellent (25 to 50 µm/yr) at 60 °C.

Although the relative dissolution rates, in Figure 4.9, indicate incompatibility between alloy 825 and 625 weld at 50 °C and 60°C, alloy 625 still showing excellent corrosion resistance in the couple condition (Figure 4.10). Therefore, it is reasonable to conclude that coupling alloy 825 to alloy 625 weld at temperatures up to 60 °C may lead to a large increase in the corrosion rate of the alloy 625 weld. However, the couple remains compatible in that temperature interval.

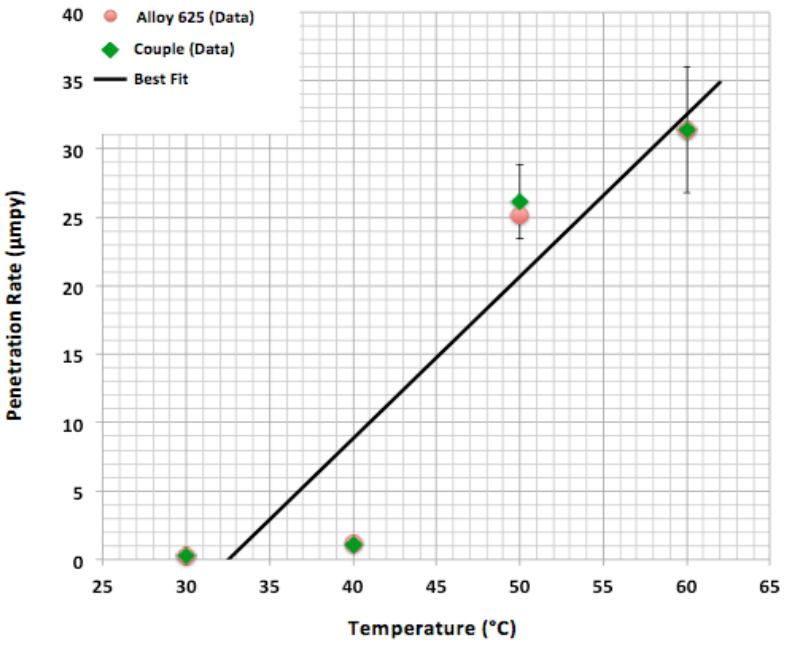

Figure 4.10 Effect of temperature on the penetration rate of the alloys 825|625 galvanic couple.

It is worth mentioning that the heat generated from the welding operation alters the microstructure and composition of the area of the base material adjacent to the fusion zone (HAZ). Normally, the galvanic potential is more active and the corrosion rates are higher at the HAZ than at the base metal and fusion zone surfaces (Bakour et al., 2012). However, the preferential corrosion attack on the alloy 825 HAZ can be minimised by postweld heat treatment.

4.4 Effect of Temperature and Welding on the Breakdown Potential of Alloys 825 and 625

Electrochemical studies of the passive films found that a characteristic potential exists above which passive films become thermodynamically unstable and may dissolve or break depending on the aggressiveness of the medium and its temperature. The effect of seawater temperature on the breakdown potential of alloy 825, alloy 625 and alloy 825 weldment will be investigated in this section.

4.4.1 Alloy 825

Table 4.4 summarises the breakdown potential of alloy 825 in synthetic seawater at different temperatures. In this work, breakdown potential was defined as the potential at which the current density exceeded 10 $\mu A/cm^2$ in the polarisation curves (see Appendix D4).

Temperature	30ºC	35ºC	40ºC	45ºC	50ºC	55ºC	60ºC	65ºC	70ºC
	0.828	0.835	0.805	0.810	0.438	0.168	0.320	0.230	0.200
Breakdown Potential (V_{SCE})	0.854	0.829	0.800	0.737	0.315	0.254	0.264	0.201	0.209
	0.856	0.836	0.825	0.738	0.396	0.210	0.370	0.200	0.197
mean (V_{SCE})	0.846	0.833	0.810	0.761	0.383	0.211	0.292	0.210	0.202
Standard deviation (V_{SCE})	0.016	0.004	0.013	0.042	0.063	0.043	0.053	0.017	0.007

Table 4.4 Breakdown potential of alloy 825 at different temperatures

Figure 4.11 illustrates graphically how the breakdown potential of alloy 825 (in Table 4.4) vary with temperature. The fitting curve reveals three distinct regions: Upper bound region (T< 45 °C), Transition region (45 °C < T < 50 °C), and Lower bound region (T > 50 °C).

Upper Bound Region

In this region, alloy 825 exhibited relatively high breakdown potentials and intergranular corrosion was observed in testing samples, despite alloy 825 being in the solution-annealed condition. It was discussed in sub-section 2.7.1 why stainless steels and nickel-based alloys can suffer intergranular attack in a few specific environments even if they are in the solution annealed condition.

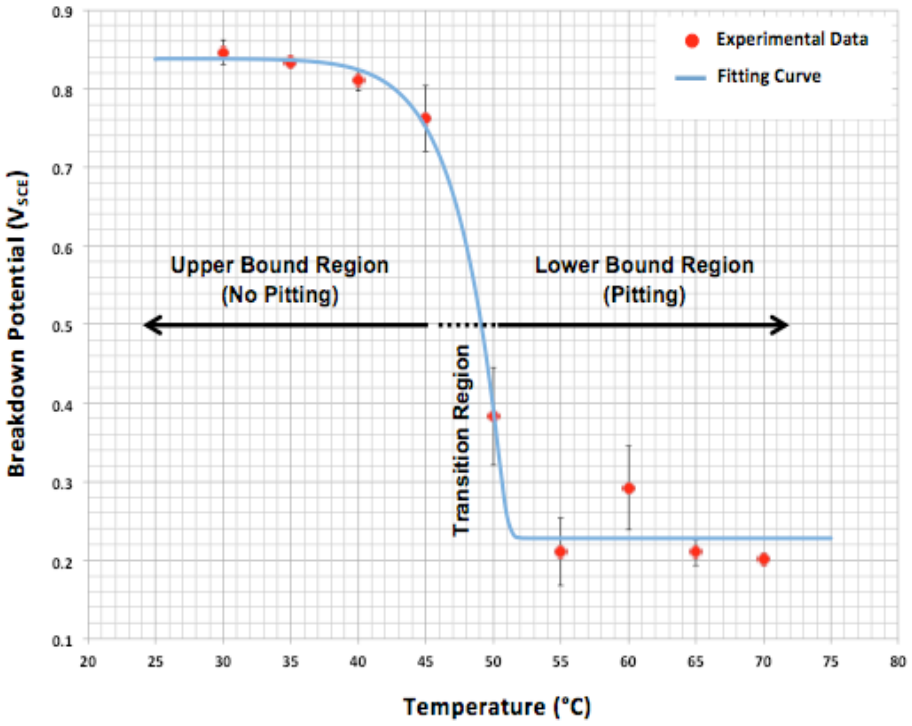

Figure 4. 11 Effect of temperature on the breakdown potential of alloy 825

Transition Region

The transition zone is characterised by a sharp slope where the breakdown potential of alloy 825 falls considerably with small increase in the temperature. In this region, pitting corrosion was observed on testing samples at 50 °C, while at 45 °C and below the alloy did not pit. The dependence of the type of corrosion attack on the temperature in this interval, suggests that there exists for alloy 825 in seawater a critical pitting temperature (CPT), which lies between 45 and 50 °C. Below the CPT, alloy 825 will not pit regardless of the oxidizing power (potential) of the seawater.

Lower Bound Region

At sufficiently high temperatures (T ≥ 55 °C), the breakdown potential dropped to a minimum value (approx. 0.205 V) and pitting corrosion was observed in alloy 825 at every temperature in this region. The pitting potential as well as the number of pits remained independent of the temperature within this region. This observation contradicts Rozenfeld theory, which supports that the number of pits is higher at elevated temperatures due to the increasing chemisorption of chloride ions on the metal surface (Szklarska-Smialowska, 1971). However, the pit density was observed

to increase as the potential increased beyond pitting potentials, suggesting that pits initiation sites in alloy 825 have different threshold potentials. Overall, there is a good agreement between the data for alloy 825 and the results of Brigham (1972), who investigated the dependence of pitting potential of various molybdenum bearing austenitic stainless steel at different temperatures.

4.4.2 Alloy 625 Weld

Table 4.5 summarises the breakdown potential of alloy 625 weld in synthetic seawater at different temperatures.

Temperature	25ºC	30ºC	40ºC	50ºC	60ºC	70ºC	80ºC
	0.084	0.357	0.332	0.345	0.250	0.181	0.170
Breakdown Potential (V_{SCE})	0.172	0.314	0.302	0.305	0.278	0.180	0.161
	0.347	0.326	0.358	0.337	0.241	0.205	0.167
mean (V_{SCE})	0.201	0.332	0.331	0.329	0.256	0.188	0.166
Standard deviation (V_{SCE})	0.134	0.022	0.028	0.021	0.019	0.015	0.005

Table 4. 5 Breakdown Potential of Alloy 625 wed at different temperatures

For better visualization of the effect of temperature on the breakdown potential of alloy 625, the experimental data in Table 4.5 were plotted in Figure 4.12.

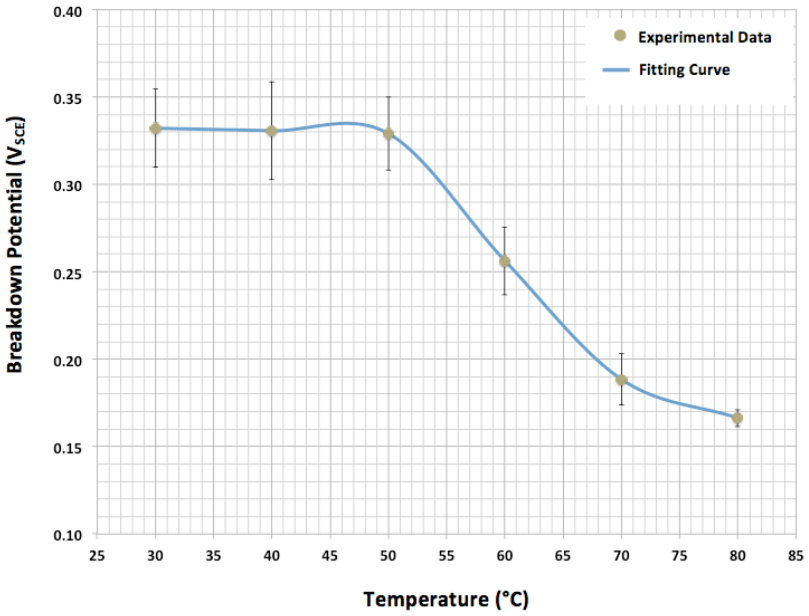

Figure 4.12 Effect of temperature on the breakdown potential of alloy 625

As can be seen from Figure 4.12, alloy 625 weld exhibits very low breakdown potentials compared to alloy 825. The passive film at the surface of alloy 625 weld is far less sensible to temperature variation in the range of 30-70 °C. This claim is supported by the relative small variation of the breakdown potential of alloy 625 weld with temperature. Such low values of potentials obtained for alloy 625 weld can be attributed to the heterogeneity observed in the microstructure of alloy 625 (see section 4.1). It was already mentioned that chromium and molybdenum oxides are responsible for the corrosion resistance of nickel-based alloys such as alloys 625 and 825. However, solidification causes micro-segregation of elements in the weld microstructure and consequently, the oxide layers formed in the weld surface will have areas, which are enriched and depleted of chromium and molybdenum. The areas with chromium and molybdenum depletion will be more active and will effectively lower the average potential of the weld.

No pitting corrosion was observed during these potentiodynamic tests of alloy 625 weld material, instead selective dissolution of the interdendritic phases (laves phases) was observed throughout the temperature range (see section 4.6). Additionally, the different temperature regions were less pronounced in alloy 625 weld than observed in the case of alloy 825.

4.4.3 Alloy 825 Weldment

Mixed potential theory cannot be used to predict the effect of welding (galvanic effect) and variation of temperature on the breakdown potential of alloy 825. Therefore, potentiodynamic polarization tests were performed directly on alloy 825 weldment. Table 4.6 summarises the breakdown potential of alloy 825 weldment obtained from the experimental polarisation curves (see Appendix D4).

Temperature	30ºC	40ºC	45ºC	50ºC	55ºC	60ºC	65ºC
	0.765	0.737	0.689	0.369	0.220	0.234	0.203
Breakdown Potential (V_{SCE})	0.762	0.714	0.712	0.563	0.301	0.211	0.220
	0.801	0.748	0.714	0.301	0.248	0.200	0.204
mean (V_{SCE})	0.776	0.733	0.705	0.411	0.256	0.215	0.209
Standard deviation (V_{SCE})	0.022	0.017	0.014	0.137	0.041	0.017	0.010

Table 4.6 Breakdown potential of alloy 825 weldment at different temperatures

Figure 4.13 is the plot of breakdown potential versus temperature for alloy 825 (Table 4. 4) and its weldment (Table 4. 6). Comparing both curves, one can observe that the breakdown potential for the weldment shifted to lower values as temperature increased, following the same trend as the breakdown potential of alloy 825. The critical pitting temperatures for both alloy 825 and its weldment fall in the same temperature interval (45 - 50 °C). The pitting potentials in the high temperature region are also similar for both alloys. The only small difference is observed in the low temperature region where breakdown potentials for the weldment are slightly lower than the corresponding values for alloy 825.

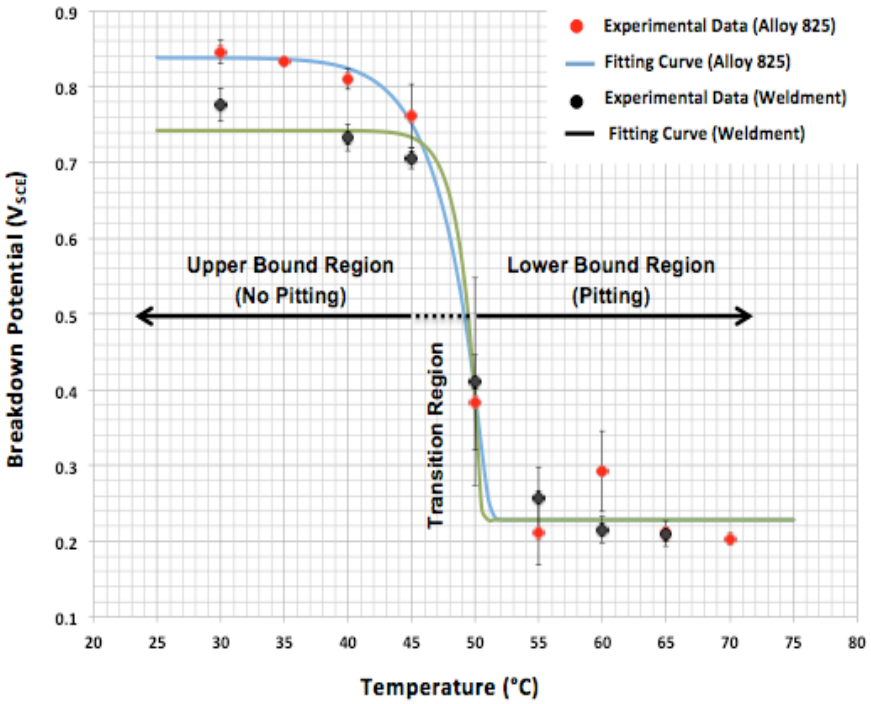

Figure 4. 13 Effect of temperature and weld on breakdown potential of alloy 825

4.5 Comparison of the Critical Pitting Temperature of Alloy 825 Obtained by Different Methods

In this section, the critical pitting temperature (CPT) value of alloy 825 in seawater determined (by the author) using potentiodynamic polarization method is compared to the value determined by McCoy et al. (2013) using different ASTM method: chemical (G48-11). The results obtained by the two methods are shown in Table 4.7 and there is no agreement among them. The reason for these differences could be due to the different test conditions used in each method.

Test Method	CPT (°C)
Chemical (ASTM G48)	30±1
Potentiodynamic (author)	45-50

Table 4.7 Critical Pitting Temperature for alloy 825 obtained from three different methods

ASTM G48 test method seems to be the most conservative method as it produced the lowest CPT value for alloy 825. Several authors have reported good correlations between the performance of alloys in 6% $FeCl_3$ solution (G48 test solution) and performance in certain real environments (Garner, 1981), (Steinsmo, Rogne and Drugli, 1997) and (Brigham and Tozer, 1973). However, this test method may be inadequate to determine the true CPT of alloys because 6% $FeCl_3$ test solution is often more severe than any real service environment. For example, there is a huge difference between the pH of acidified 6% $FeCl_3$ solution (pH = 1,5) and natural seawater (pH =8,2). Furthermore, CPT values using ASTM G48 methods are sometimes calculated using empirical equations (Brigham and Tozer, 1974) and that may also cause them to be lower than would be measured.

According to ASTM G48-11, these test methods can be used for quality control of stainless steels and ranking the pitting susceptibility of a series of alloys. However, it should not be used to determine maximum allowable service temperatures (CPT). ASTM G48 test methods yield a gross underestimation of the true CPT values. Underestimating CPT will result, consequently, in an unnecessary use of very expensive corrosion resistant alloys.

Potentiodynamic CPT tests were performed in synthetic seawater and the samples potential were scanned at rate of 0.1mV/s from the corrosion potential. The CPT value from potentiodynamic tests falls between 45 - 50°C, which further complicates the search for the actual CPT for alloy 825 in seawater, since that interval is not closer to the value determined by the previous methods. However, based on the transition from intergranular corrosion to pitting corrosion observed between 45 - 50°C (Figure 4.11), it can be argued that the potentiodynamic method yields the most reliable CPT value. That transition in corrosion behaviour suggests that there exists a critical pitting temperature for alloy 825 below which the alloy is immune to pitting corrosion, regardless of the potential and time of exposure.

4.6 Corrosion Morphology

Surface morphologies, after potentiodynamic testing, for alloys 825, 625 weld and the weldment have been investigated in this section. Three major types of corrosion attack were observed. The morphology of attack on the alloy 825 and weldment were found to be temperature dependent in the 30 - 70 °C range, while alloy 625 weld exhibits the same corrosion morphology throughout the whole temperature interval. The corrosion morphology observed in testing samples were classed into two groups; low temperature (T< 45 °C) and high temperature (T > 50 °C).

4.6.1 Low Temperature Corrosion Morphology

In this temperature region, alloy 825 underwent intergranular corrosion (IGC), which is hardly observed with high-nickel alloys in solid annealed condition (Figure 4.14). It was discussed in sub-section 2.7.1 that the IGC susceptibility of annealed nickel based alloys depends on the properties of the intergranular zones of the crystal lattice, i.e. grain boundaries. These are high-energy regions that collect drained point defects, precipitated second particles and segregated elements or impurities (Kasparova, 2000). Therefore, upon exposure to very strongly oxidising solutions, the chemical and physical difference between grain boundaries and the grains serve as the driving force for intergranular corrosion.

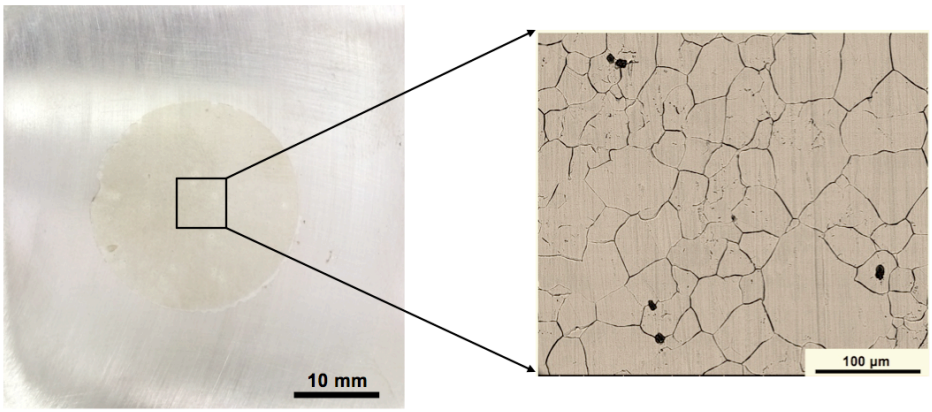

Figure 4.14 Intergranular corrosion attack on alloy 825 at T< 45°C

Alongside intergranular corrosion, some pits were also observed in alloy 825 in low temperature range (Figure 4.15). As shown in section 4.1, the surface of alloy 825 is not homogeneous, contains relatively large titanium nitride (TiN) inclusions. This compound, although chemically stable, may act as a pit nucleation site. Possible evidence of TiN disolution was found in the potentiodynamic polarisation curves of

alloy 825 at 35 °C and 45 °C temperatures (see Appendix B), where the current density increases sharply at certain passive potential.

According to Szklarska-Smialowska (2005:397), mechanical treatments such as polishing and grinding processes may cause surface microcracks at the inclusion/matrix interface. Therefore, electrochemical dissolution of inclusions start at the bottom of the microcrack at a certain passive potential or below the oxygen evolution potential. Although there is supporting evidence to show that titanium inclusion compounds can act as pit nucleation sites (Szklarska-Smialowska, 2005: 385). However from the standpoint of crevice and pitting corrosion titanium inclusions are less harmful than MnS, FeS and CrS precipitates (Dowling et al., 1995).

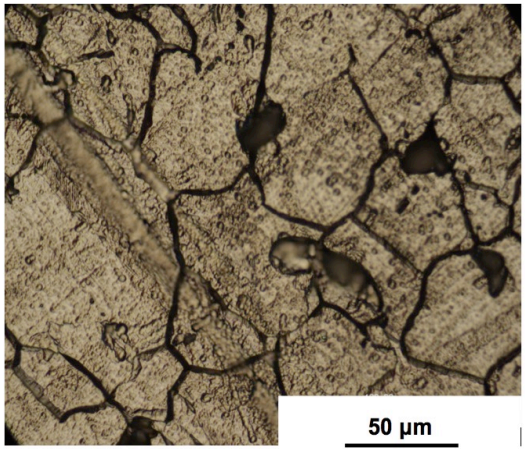

Figure 4.15 Pitting and intergranular corrosion attack observed on alloy 825 at T< 45°C

Alloy 625 (in form of a weld) underwent selective dissolution attack of the interdendritic phase or lave phase commonly observed in the microstructure of welds (Figure 4.16). This type of attack is attributed to the micro-segregation or coring phenomenon that occurs during weld solidification.

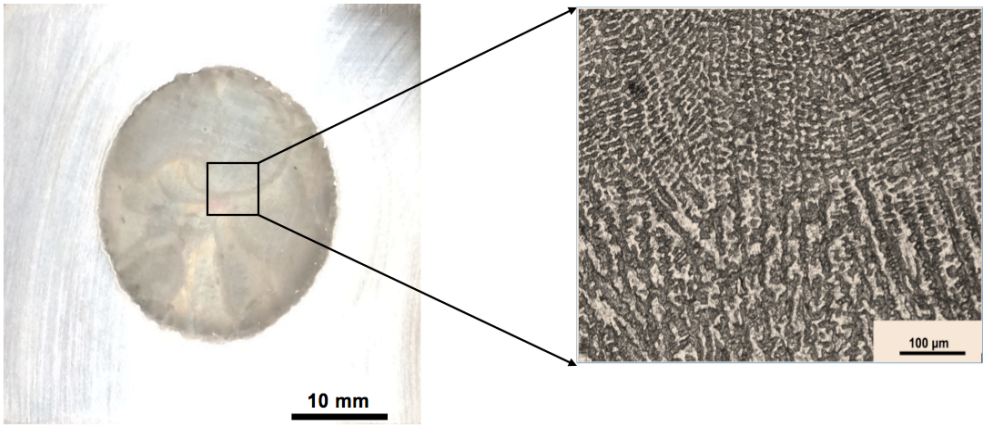

Figure 4.16 Selective dissolution of interdendritic phase on alloy 625 at T <45°C

Micro-segregation causes the dendrite phase to be enriched with Fe, Cr and Ni, while the interdendrite phases becomes depleted of these elements in alloy 625 weld microstructures (Cieslak et al., 1988). Therefore, the dendrite phase will act as the cathode to the interdendrite phase when exposed to aggressive corrosive environment and microgalvanic cells will be created across the alloy 625 weld microstructure. Almost always, welded structures have less resistance to corrosion than filler metals or alloys of the same composition due to the micro-segregation phenomenon. Post weld heat treatment is generally required to improve the weld corrosion resistance.

Alloy 825 (BM) and alloy 625 weld (FZ) preserved their corrosion mode in the weldment in the low temperature range. The heat-affected zone (HAZ), which was totally recrystallized, suffered intergranular attack as the base material alloy (see Figure 4.17). This type of attack in HAZ is also referred as weld decay or low-temperature heat affected zone corrosion (Henthorne, 1972: 70). Most of the time, intergranular corrosion problems in HAZ of nickel based alloys and stainless steels are related to the metallurgical changes occurring in the sensitization range.

For the case of alloy 825 HAZ, an exposure of several seconds or minutes during welding at temperatures in the range 927-982 °C (sensitization temperatures) causes precipitation of chromium-rich carbide ($M_{23}C_6$) at areas adjacent to grain boundaries (Raymond, 1968). Therefore, the chromium and molybdenum depleted zone across the grain boundaries becomes susceptible to corrosion attack as show in Figure 4. 17.

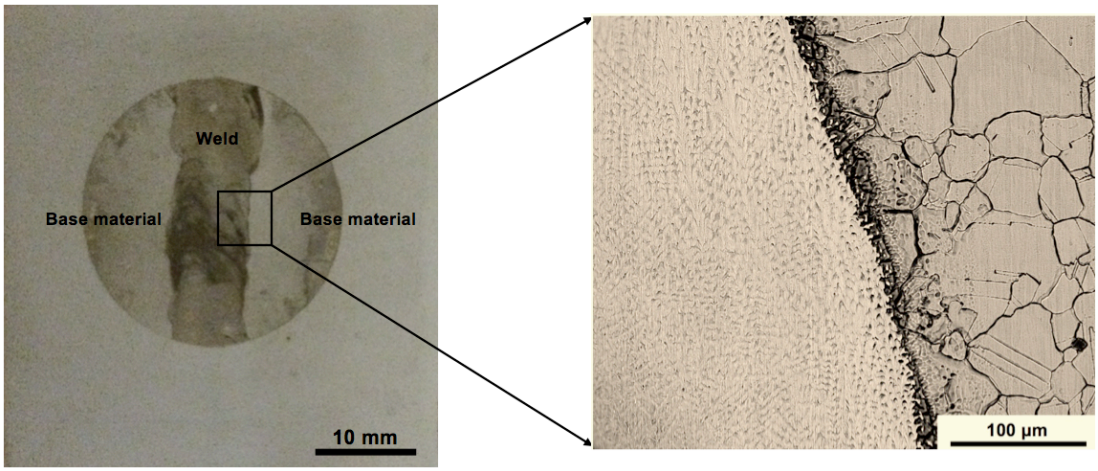

Figure 4.17 Intergranular and selective dissolution of interdendritic phase on alloy 825 weldment at T <45°C

4.6.2 High Temperature Corrosion Morphology

At temperatures higher than 50 °C, alloy 825 underwent surface tarnishing followed by catastrophic pitting. The pitting density and shapes in the samples were dependent on the applied potential i.e. at pitting potential (E_p) or near it, single and deep pits were observed on the surface of the samples (Figure 4. 18) while several larger but less deep pits were observed at potentials much higher than the E_P (Figure 4. 19).

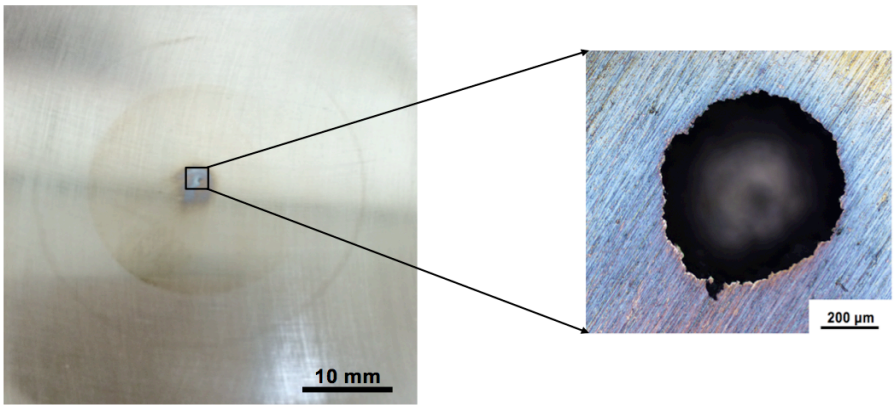

Figure 4. 18 Pitting corrosion observed on alloy 825 at T >50°C

These observations are in good agreement with studies by others researchers. However, it cannot be determined whether the dependence of pitting generation rate on potential obeys a linear or an exponential function. Therefore, no statement can be made about the mechanism of pit initiation. According to Videm (1974), an exponential relationship between pitting generation rate and potential suggests that the adsorption of chloride ions controls the pit initiation, while Shibata and Takeyama (1977) advocate that a linear relationship implies that electromechanical breakdown of the passive film is the dominant mechanism for pitting generation.

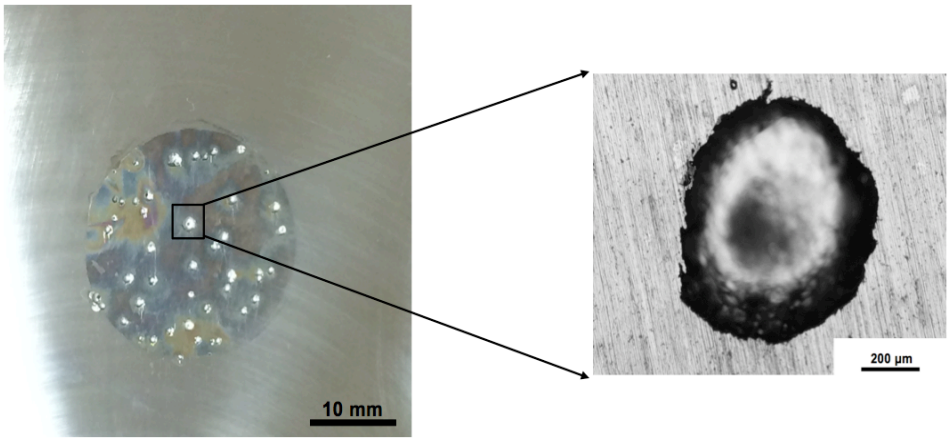

Figure 4.19 Effect of applied potential on pitting density of alloy 825

In general, pits were covered with remaining porous passive films (Figure 4.20). According to Frankel et al. (1987), these covers are responsible for the devepment of metastable pits into stables ones. Destroying such porous layer during metastable growth leads to repassivation of the pits. On the other hand, “cover on pits can make visual detection very difficult, so that the awareness of the severity of attack is overlooked and the likelihood of catastrophic failure is enhanced” (Frankel, 1998).

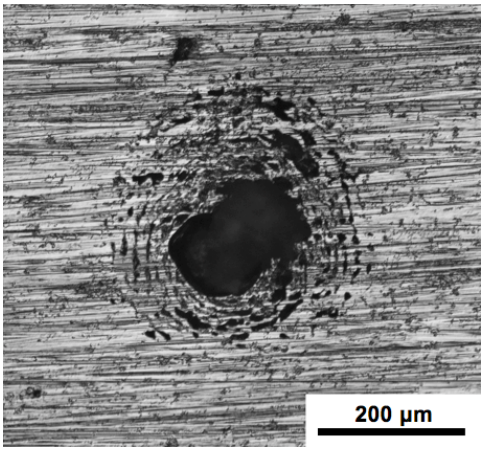

Figure 4.20 Pit on alloy 825 showing a pit cover with passive film

Figure 4.21 shows the pitting corrosion in alloy 825 weldment and no pitting attack was observed in the weld metal (alloy 625). The preferential attack on base material (alloy 825) rather than in fusion zone indicates that elemental segregation on the weld microstructure has no effect on pitting resistance of weld alloy 625 in seawater environment, at least not in temperature range of 30 - 80 °C. Furthermore, these results also highlight the beneficial effect of using alloy 625 as overmatching filler metal to weld alloy 825. It accepts iron dilution from the base material (alloy 825) while providing greater pitting corrosion resistance in as-welded condition.

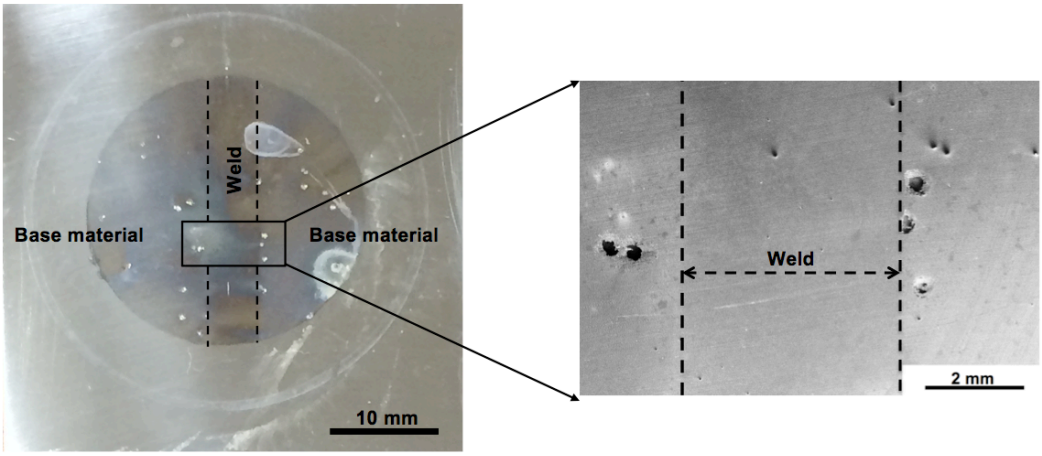

Figure 4.21 Pitting corrosion on alloy 825 weldment

4.7 Correlation Between Laboratory Tests and Performance of Alloy 825 Weldment in Real Environment (Seawater)

A major goal of this study was to test whether laboratory accelerated corrosion tests could be used to predict the performance of the alloy 825 in seawater. Therefore, long-term immersion tests were conducted in stagnant seawater for more than six months. Furthermore, these tests were performed at four maximum allowed seawater temperatures for alloy 825, predicted by the accelerated corrosion tests (see section 4.5). The test samples were welded so that the effect of welding could be observed.

Table 4.8 summarises results of both laboratory corrosion tests and seawater long-term immersion tests. It was already mentioned (in section 4.5) that those results for chemical (ASTM G48) was obtained from works of McCoy et.al. (2013). As can be seen from Table 4.8, no pitting corrosion attack was observed in the weldment after six months of immersion test, regardless of the solution temperature. Clearly, these results indicate that there is no correlation whatsoever, between the accelarated laboratory corrosion tests and the long-term immersion tests.

		Critical Pitting Temperature			
Testing Method	**Testing Sample**	**30°C**	**50°C**	**60°C**	**70°C**
Chemical (ASTM G48)	Alloy 825	Y			
Potentiodynamic	//		Y		
Long-Term Immersion	Weldment	N	N	N	N
Note:					
Y = Pitting Corrosion attack					
N= No attack					

Table 4.8 Electrochemical accelerated and laboratory immersion tests results

Figure 4.22 shows critical temperatures (CPT) and the respective potentials for alloy 825, obtained using accelerated tests as well as the immersion test temperatures. In the potentiodynamic pitting tests, alloy 825 potential was shifted from cathodic to anodic direction at scan rate of 0.1 mV/s, pitting corrosion was first observed at 50 °C and potential was around 350 mV_{SCE}. According to (Ronge, Druli and Valen, 1992), the 6% $FeCl_3$ test solution used in chemical tests (ASTM G48) is too severe such that potentials of passive alloys rise to the range of 600 to 650 mV_{SCE}.

All the accelarated corrosion tests were probably performed above the critical pitting potential of alloy 825, while long-term exposure tests were performed at alloy 825 stable rest potential (corrosion potential) , which was about -350 mV_{SCE} (see Table 4. 8). Under real service conditons, pitting corrosion is normally observed at potentials and temperatures higher than the pitting potential and critical pitting temperatures respectively (Szklarska-Smialowska, 2005). In this regions, metastable pits are capable of becoming stable. Furthermore, the induction time for pitting nucleation has also been found to be a function of the pitting potential. Supporting findings have been published by Dunn, Sridhar and Cragnolino (1996), where alloy 825 was immersed in a chloride solution at 95 °C and no pitting was observed at potentials lower than 500 mV_{SCE} even after 2 days.

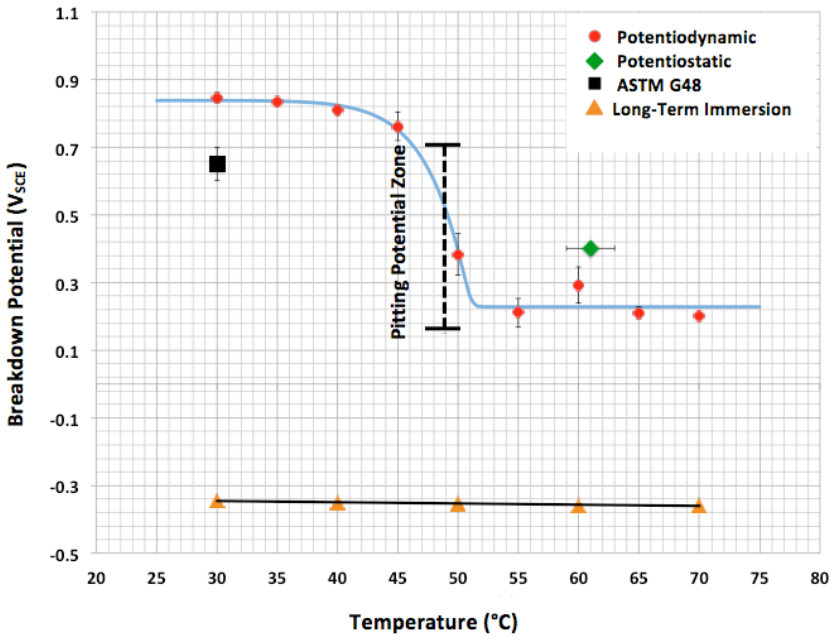

Figure 4.22 Critical pitting temperatures for alloy 825 and their potential range

The lack of correlation between critical pitting temperature determined by electrochemical laboratory tests and the temperature above which alloy 825 would exhibit pitting corrosion in exposure tests is due to the difference in potential at which the tests were performed. The exposure tests remained at rest potential, or coupled potential, while the electrochemical tests scanned through the potential range, which forced the potential into the transpassive region. It appears that the critical pitting temperature determined by all electrochemical tests (potentiodynamic and potentiostatic) and ASTM G48 were all found at or above the critical pitting potential of alloy 825. On the other hand, in the long-term immersion test, samples were exposed to natural seawater at temperatures suggested by the electrochemical tests

but the exposure conditions were not severe enough (freely exposed and at corrosion potential) to induce pitting corrosion in alloy 825 weldment.

CHAPTER FIVE: CONCLUSIONS & RECOMMEDATIONS

5.1. CONCLUSIONS

The purpose of this dissertation was to evaluate the corrosion behaviour of alloy 825, alloy 625 welds and alloy 825 weldment in stagnant seawater over a range of temperatures. The following conclusion can be drawn from the results obtained:

- Alloys 825 and 625 weld, like any other chromium containing alloy, are passivated by air formed films. These films are probably formed from spinels of iron, chromium, nickel and molybdenum.

- Welding solidification causes elemental segregation and variation in the alloy 625 filler metal. Polarization results obtained indicate that welding shifts the corrosion potential (E_{corr}) of alloy 625 to more anodic values.

- Alloy 825 and alloy 625 weld exhibit outstanding resistance to uniform or general corrosion (< 25 μm/yr) in seawater in the temperature range 30 to 60 °C. The corrosion resistance of both alloys will continue to improve gradually in a long-term as the passive film gets thicker.

- Although the predicted current density of alloy 625 weld increases substantially when it is coupled to alloy 825, alloy 625 weld still exhibits excellent corrosion resistance within 30 to 60 ºC temperature range. Therefore, the galvanic effect between alloy 825 (base material) and alloy 625 weld (fusion zone) is not of concern.
- The breakdown potential of alloys 825, 625 and 825 weldment becomes more active (i.e. less positive e.m.f) as the temperature increases. Except for alloy 625 weld, there is considerable decrease in breakdown potential in a very narrow temperature interval, which coincides with the transition from transpassive or grain boundary corrosion to pitting corrosion.

- The effect of welding on the breakdown potential of alloy 825 is negligible.

- The alloy 825 critical pitting temperature from two independent test laboratory methods, one potentiometrically controlled and one freely corroding were compared. There was no agreement between the test results, the freely corroding test (ASTM G48) gave the most conservative estimative result (30°C). The most reliable result was obtained from the potentiodynamic test where the transition from grain boundary to pitting corrosion suggest that there is a temperature in the 30 to 60 °C interval below which alloy 825 does not suffer pitting corrosion when exposed to seawater.

- Corrosion attack and the morphology of alloy 825 and its weldment are temperature and potential dependent. At temperatures below 45 °C, very high potentials were required to breakdown the passive film and grain boundary attack was observed in alloy 825 samples. At temperatures higher than 50 °C, relatively low potentials were required to induce pitting corrosion on alloy 825 sample surfaces. Alloy 625 required very low potential to breakdown its passive film compared to alloy 825. However, alloy 625 exhibited only one mode of corrosion attack (i.e. galvanic corrosion) throughout the temperature testing range.

- The lack of correlation between the critical pitting temperature determined by electrochemical laboratory tests and the temperature above which alloy 825 would exhibit pitting corrosion in much longer seawater exposures is due to the potential at which alloy 825 samples were held during the different tests. All the electrochemical tests were performed above the critical pitting potential of alloy 825 and its weldment and hence pitting occurred. On the other hand, the immersion tests were performed at the rest corrosion or coupled potential and no pitting was observed in the samples regardless of the test temperature.

- Overall, alloys 825 and 625 and the weldment proved to be excellent choices for seawater application under severe conditions, because both alloys 825 and 625 weld exhibit outstanding resistance to uniform or general corrosion (< 25 μm/yr) in seawater in the temperature range 30 to 60 °C.

5.2. RECOMMENDATIONS

This section highlights some of the shortcomings of the research and gives recommendations for future work:

- In this research, only the grain boundaries, galvanic and pitting corrosion have been assessed, while in the seawater environment crevice corrosion, erosion corrosion and microbial induced corrosion are forms of corrosion often found in offshore seawater systems. Therefore, for the future prediction of the corrosion resistance and service life of alloy 825 in and offshore environment, further experimental work should be performed to evaluate the susceptibility of alloy 825 to the other form of corrosions.

- Mixed potential and galvanic current density for alloy 825 weldment were predicted using the mixed potential theory proposed by Wagner & Traud (1938) and polarisation curves of alloys 825 and 625 weld samples in the uncoupled conditon. Alloy 825 HAZ formed by the heat of welding was not considered in prediction of the galvanic parameters. According to the work of Bakour et al., (2012) , the galvanic potential tends to be more active (i.e. more negative e.m.f) and the corrosion rates higher at the HAZ than in the base metal and fusion zone surfaces. Therefore, in the future, polarization curves should also be measured in the HAZ for more accurate prediction of the effect of welding on the corrosion behaviour of alloy 825.

- Critical pitting temperature (CPT) for alloy 825 in seawater were compared based on three different test methods (one chemical and one potentiometrically controlled). However, there was no agreement in the results obtained. In order to verify the reliability of these results, electrochemical impedance spectroscopy technique (EIS) should be employed as an alternative method. EIS technique employs ac current to investigate the passive film properties. According to Ebrahimi et al. (2012), as the testing temperature increases, the charge transfer resistance of the testing sample decreases. CPT is the temperature where the charge transfer resistance of the testing sample falls down significantly due to the local activity of the surface.

REFERENCE

Abd El Kader, J. and Shams El Din, A. (1979) 'Film Thickening on Nickel in Aqueous Solution in Relation to Anion Type and Concentration', British Corrosion Journal, vol. 14, no. 1, January, pp. 40-45.

Abd El Meguid, E. and Abd El Latif, A. (2007) 'Critical Pitting Temperature for Type 254 SMO Stainless Steel in Chloride Solutions', Corrosion Science, vol. 49, no. 2, February, pp. 263-275.

Al-Frozan, S. A. and Malik, A. U. (2008) 'Effect of Seawater Level on Corrosion Behaviour Different Alloys', Desalination, Vol. 228, pp. 61- 67.

ASM International (1990) ' Properties and Selection: Nonferrous Alloys and Special-Purpose Materials', ASM Metals Handbook: Vol.2. USA

American Society for Testing Materials (2011) Standard Test Methods for Pitting and Crevice Corrosion Resistance of Stainless Steels and Related Alloys by Use of Ferric Chloride Solution (ASTM G48-11), Pennsylvania: ASTM.

American Society for Testing Materials (2013) Standard Reference Test Method for Making Potentiodynamic Anodic Polarization Measurements (ASTM G5-13), Pennslvania: ASTM.

American Society for Testing Materials (2013) Standard Test Method for Electrochemical Critical Pitting Temperature Testing of Stainless Steels (ASTM G150-13), Pennsylvania: ASTM International.

American Society of Testing Materials (2006) Standard Test Method for Conducting Cyclic Potentiodynamic Polarisation Measurements to Determine the Corrosion Susceptibility of Small Implant Devices (ASTM F2129-06), Pennsylvania: ASTM International.

Amon, C., Howl, R. and Oldfield, J. (1999) 'Alloy 825 and 718 Gasket Corrosion in Deep Water (500m) Connection', Corrosion 99, Houston, 332.

Analytical, R. (2004) Conductivity, Theory and Practice, 1st edition, Lyon: Radiometer Analytical SAS.

Bakour, S., Bellaouchou, A., Escriva-Cerdan, C., Sanchez-Tavor, R., Leiva-Garcia, R. and Garcia-Anton, J. (2012) 'Effect of Welding on the Corrosion Behaviour of a Highly Alloyed Austenitic Stainless Steel UNS N06027 in polluted phosphoric acid media', International Journal of Electrochemical Science, vol. 7, no. 7, July, pp. 10530-10543.

Beavers, J., Koch, G. and Berry, W. (1986) Corrosion of Metals in Marine Environments, 1st edition, Ohio: MCIC.

Beverskog, B. and Puigdomenech, I. (1997) 'Revised Pourbaix Diagram for Chromium at 25-300 C', Corrosion Science, vol. 39, no. 1, January, pp. 43-57.

Boboian, R. (1976) 'Electrochemical Techniques for Predicting Galvanic Corrosion ', Galvanic and Pitting Corrosion-Field and Laboratory Studies, Pennsylvania, 5-19.

Boboian, R., France, W., Rowe, L. and Rynewicz, J. (1976) Galvanic and Pitting Corrosion-Field and Laboratory Studies, 1st edition, Pennsylvania: ASTM.

Boboian, R. (Ed.) (2005) ' Corrosion Tests and Standards: Application and Interpretation', 2nd Edition, ASTM International.

Bockris, J.O. and Drazic, D. (1972) Electro-Chemical Science, 1st edition, London: Taylor & Francis LDT.

Boyd, W. and Fink, F. (1978) Corrosion of Metals in Marine Environments, 1st edition, Ohio: MCIC.

Bradford, S. (2001) Corrosion Control, 2nd edition, Canada.

Brigham, R. (1972) 'Pitting of Molybdenum Bearing Austenitic Stainless Steel', Corrosion, vol. 28, no. 5, May, p. 177.

Brigham, R. and Tozer, E. (1973) 'Temperature as a Pitting Criterion', Corrosion, vol. 29, no. 1, January, pp. 33-36.

Brigham, R. and Tozer, E. (1974) 'Effect of Alloying on the Pitting Resistance of 18% Cr Austenitic Stainless Steel', Corrosion, vol. 30, no. 5, May, p. 161.

Brown Jr., G., Henrich, V., Casey, W., Clark, D. and Eggleston, C. (1999) 'Metal Oxide Surface and Their Interactions with Aqueous Solutions and Microbial', US Department of Energy Publications, 1 Jan.

Burstein, G., Pistorius, P. and Mattin, S. (1993) 'The Nucleation and Growth of Pits on Stainless Steel', Corrosion Science, vol. 35, no. 4, April, pp. 57-62.

Cardoso, M., Amaral, S. and Martini, E. (2008) 'Temperature Effect in the Corrosion Resistance of Ni-Fe-Cr Alloy in Chloride Medium', Corrosion Science, vol. 50, no. 7, July, pp. 2429-2436.

Carranza, R. and Alvarez, M. (1996) 'The Effect of Temperature on the Passive Film Properties and Pitting Behaviour of a Fe-Cr-Ni Alloy', Corrosion Science, vol. 38, no. 6, June, pp. 909-925.

Cieslak, M. (1991) 'The Welding and Solidification Metallurgy of Alloy 625', Welding Journal, vol. 70, no. 2, February, pp. 49s-56s.

Cieslak, M., Headley, T., Kollie, T. and Romig Jr., A. (1988) 'A Melting and Solidification Study of Alloy 625', Metallurgical Transactions A, vol. 19A, no. 10, September, pp. 2319-2331.

Cieslak, M., Knorovsky, G., Headley, T. and Romin Jr., A. (1986) 'The Use of New PHACOMP in Understanding the Solidification Microstrucure of Nickel Base Alloy Weld Metal', Metallurgical Transactions A, vol. 17A, no. 12, December, pp. 2107-2116.

Crum, J., Shoemaker, L. and Kiser, S. (2000) 'Alloys and Overmatching Welding Products Solve FGD Corrosion Problems', Corrosion 2000, Florida, 26-31.

Devereux, F. and Yeum, K. (1992) 'Modeling Electron Transfer, Diffusional Effects, Passivation, and Ohmic Loss in Multi-Reaction Polarisation Curves', Computer Modeling in Corrosion,ASTM STP 1154, Philadelphia, 126-142.

Dowling, N., Duret-Thual, C., Auclair, G., Audouard, J. and Combrade, P. (1995) 'Effect of Complex Inclusions on Pit Initiation in 18% Cr-8% Ni Stainless Steel Types 303,304 and 321', Corrosion Science, vol. 51, no. 5, May, pp. 343-355.

Drogowska, M., Brossard, L. and Me'nard, H. (1998) '304 Stainless steel oxidation in sulfate and sulfate bicarbonate solutions', Journal of Applied Electrochemistry, vol. 28, no. 5, May, pp. 491-501.

Dunn, D., Sridhar, N. and Cragnolino, G. (1996) 'Long-Term Predition of Localized Corrosion of Alloy 825 in High-Level Nuclear Waste Repository Environment', Corrosion Science, vol. 52, no. 2, February, pp. 115-124.

DuPont, J. (1996) 'Solidification of an 625 Weld Overlay', Metallurgical and Materials Transactions A, vol. 27A, no. 10, November, pp. 3612-3620.

DuPont, J., Lippold, J. and Kiser, S. (2009) Welding Metallurgy and Weldability of Nickel-Based Alloys, New Jersey: John Wiley & Sons.

Ebrahimi, N., Momeni, M., Kosari, A., Zakeri, M. and Moayed, M. (2012) 'A Comparative Study of Critical Pitting Temperature of Stainless Steels by Electrochemical Impedance Spectroscopy, Potentiodynamic and Potentiostatic Techniques', Corrosion Science, vol. 59, pp. 96-102.

Elayaperumal, K. and Raja, V.S. (2015) Corrosion Failures, Theory, Case Studies and Solutions, 1st edition, New Jersey: Wiley.

Evans, U. (1960) The Corrosion and Oxidation of Metals, 1st edition, London.

Flitt, H. and Schweinsberg, D. (2010) 'Shynthesis, Matching and Deconstruction of Polarisation curves fo the Active Corrosion of Zinc in Aerated Near-Neutral NaCl Solutions', Corrosion Science, vol. 52, no. 3, March, pp. 1905-1914.

Fontana, M. (1987) Corrosion Engineering, 3rd edition, Sinpore: McGraw-Hill Book Co.

Frankel, G. (1998) 'Pitting Corrosion of Metals :A Review of the Critical Factors', Journal of the Electrochemical Socciety, vol. 145, no. 6, January, pp. 2186-2198.

Frankel, G.S., Stockert, L., Hunkeler, F. and Boehni, H. (1987) 'Metastable Pitting of Stainless Steel', Corrosion, vol. 43, no. 7, July, pp. 429-436.

Galvele, J. (1976) 'Transport Processes and Mechanism of Pitting of Metals', Journal of the Electrochemical Society, vol. 123, no. 4, April, pp. 454-474.

Gamry, I. (2015) Application Note: Copliance Voltage: How much is enough?, [Online], Available: HYPERLINK " www.gamry.com/site-search/results?search=application+notes" [30 March 2015].

Garner, A. (1981) 'Crevice Corrosion of Stainless Steel in Seawater; Correlation of Field and Laboratory Tests', Corrosion, vol. 37, March, p. 178.

Garverick, L. (1994) Corrosion in the Petrochemical Industry, 1st edition, ASM.

Goodman, P. (1987) 'Effect of Chlorination on Materials for Sea Water Cooling Systems: A Review of Chemical Reactions', British Corrosion Journal, vol. 22, no. 1, January, pp. 56-62.

Groysman, A. (2009) Corrosion For Everybody, Illustrated edition, Amsterdam: Springer.

Henthorne, M. (1972) 'Intergranular Corrosion in Iron and Nickel Base Alloys', Symposium on Localized Corrosion-Cause of Metal Failure, Philadelphia, 66-119.

Ives, M., Lu, Y. and Luo, J. (1991) 'Cathodic Reactions Involved in Metallic Corrosion in Chlorinated Saline Environments', Corrosion Science, vol. 32, no. 1, January, pp. 91-102.

Jones, D. (1996) Principles and Prevention of Corrosion, 2nd edition, New Jersey: Prentice-Hall,Inc.

Kasparova, O. (2000) 'Intergranular Corrosion of Nickel Alloys (Review)', Protection of Metals, vol. 36, no. 6, June, pp. 575-583.

Kelly, R., Scully, J., Shoesmith, D. and Buchheit, R. (2002) Electrochemical Techniques in Corrosion Science and Engineering, 1st edition, New York: Marcel Dekker,Inc.

Kennard, E. and Waber, J. (1970) 'Mathematical Study of Galvanic Corrosion : Equal Coplanar and Cathode with Unequal Polarisation Parameters', Journal of the Electrochemical Society, vol. 117, no. 7, July.

Kruger, J. (1976) 'Passivity and Its Breakdown of Iron and Iron-Base Alloys', NACE, Houston, 91.

Macdonald, D. (1992) 'The Point Defect Model for the Passive State', Journal of the Electrochemical Society, vol. 139, no. 12, December, p. 3434.

Manning, P. (1980) 'The Effect of Scan Rate on the Pitting Potential of High Performance Alloys in Acidic Chloride Solution', Corrosion , vol. 36, no. 9, September, pp. 468-474.

Mansfeld, F. (1971) 'Area Relationships in Galvanic Corrosion', Corrosion, vol. 27, no. 10, October, pp. 436-442.

Mansfeld, F. (1973) 'Galvanic Corrosion of Al Alloys Coupled to Coated PH13-8Mo Stainless Steel', Corrosion , vol. 29, no. 7, July, pp. 276-281.

Mansfeld, F., Hengstenberg, D. and Kenkel, J. (1974) 'Galvanic Corrosion of Al Alloys I. Effect of Dissimilar Metals', Corrosion , vol. 30, no. 10, October, pp. 434-353.

Mansfeld, F. and Kenkel, J. (1976) 'Laboratory Studies of Galvanic Corrosion of Aluminum Alloys', Galvanic and Pitting Corrosion-Field and Laboratory Studies STP 576, pp. 20-47.

Marion, G., Millero, F., Camoes, M., Spitzer, P., Feistel, R. and Chen, C. (2011) 'pH of Seawater', Marine Chemistry, vol. 126, no. 1-4, September, pp. 89-96.

McCafferty (2010) Introduction to Corrosion Science, 1st edition, Alexandria: Springer.

McCoy, S., Puckett, B. and Hibner, E. (2013) High Performance Age-Hardenable Nickel Alloys Solve Problems in Sour oil & Gas Service, January, [Online], Available: HYPERLINK http://www.pccforgedproducts.com/web/user_content/files/wyman [14 June 2015].

Mueller, W. (1962) 'Derivation of Anodic Dissolution Curve of Alloys from those of Metallic Components', Corrosion, vol. 18, no. 2, February, pp. 73t-79t.

NACE (2015) Pitting Corrosion, 9 May, [Online], Available: HYPERLINK https://www.nace.org/Pitting-Corrosion [9 May 2015].

Natishan, P., O'Grady, W., McCafferty, E., Ramaker, D., Pandya, K. and Russel, A. (1999) 'Chloride Uptake by Oxide Covered Aluminum as Determined by X-Ray Photoelectron

and X-Ray Absorption Spectroscopy', Journal of the Electrochemistry Society, vol. 146, no. 5, May, pp. 1737-1740.

Oldfield, J. (1988) 'Electrochemical Theory of Galvanic Corrosion', Galvanic Corrosion, Philadelphia, 5 - 22.

Paul, L., Clark, G., Eckhardt, M., Hoberg, B. (2004) 'Experience with Weld Overlay and Solid Alloy Tubing Materials in Waste to Energy Plants'. 12th North American Waste to Energy Conference, Savannah, Georgia, USA, May 17-19. ASME, pp111-119.

Petzow, G. (1999) Metallographic Etching 2nd Edition, 2nd edition, Ohio: ASM International.

Pistorius, P. and Burstein, G. (1994) 'Aspects of the Effects of Electrolyte Composition on the Occurence of Metastable Pitting on Stainless Steel', Corrosion Science, vol. 36, no. 3, April, pp. 525 - 538.

Pourbaix, M. (1974) Atlas of Electrochemical Equilibria in Aqueous Solutions , 1st edition, Texas: NACE.

Qvarfort, R. (1989) 'Critical Pitting Temperature Measurements of Stainless Steels with an Improved Electrochemical Methode', Corrosion Science, vol. 29, no. 8, June, pp. 987-993.

Raymond, E. (1968) 'Mechanisms of Sensitization and Stabilization of Incoloy Nickel-Iron-Chromium Alloy 825', Corrosion, vol. 24, no. 6, June, pp. 180-188.

Revie, R. (Ed.) (2011) Uhlig's Corrosion Handbook, 3rd edition, New Jersey: John Wiley & Sons.

Ronge, T., Druli, J. and Valen, S. (1992) 'Testing of Stainless Steel Welds for Varios Applications', Corrosion, vol. 48, no. 10, October, p. 864.

Salinas-Bravo, V. and Newman, R. (1994) 'An Alternative Method to Determine CPT of Stainless Steels in Ferric Chloride Solution', Corrosion Science, vol. 36, no. 1, January, pp. 67-77.

Shibata, T. and Takeyama, T. (1977) 'Stochastic Theory of Pitting Corrosion', Corrosion, vol. 33, no. 7, July, p. 243.

Shreir, L. (1982) Electrochemical Principles of Corrosion : A Guide for Engineers, 1st edition, London.

Silva, C., de Miranda, H., Motta, M., Farias, P., Afonso, C. and Ramirez, A. (2013) 'New Insight on the Solidification Path of Alloy 625 Weld Overlay', Journal of Materials Research and Technology, vol. 2, no. 3, February, pp. 228-237.

Steinsmo, U., Rogne, T. and Drugli, J. (1997) 'Aspect of Testing and Selecting Stainless Steels for Seawater Applications', Corrosion, vol. 53, no. 12, December, p. 955.

Stern, M. (1958) 'Surface Area Relationships in Polarisation and Corrosion', Corrosion, vol. 14, no. 7, July, pp. 43-46.

Stern, M. (1958) 'The Mechanism of Passivating -Type Inhibitors', Journal of the Electrochemical Society, vol. 105, no. 11, November, pp. 638-647.

Stern, M. and Geary, A. (1957) 'Electrochemical Polarisation I. A Theoretical Analysis of the Shape of Polarisation Curves', Journal of the Electrochemical Society, vol. 104, no. 1, January, pp. 56-62.

Streicher, M. (1956) 'Pitting Corrosion of 18Cr-8Ni Stainless Steel', Journal of the Electrochemical Society, vol. 103, no. 7, July, pp. 375-390.

Szklarska-Smialowska, Z. (1971) 'Review of Literature on Pitting Corrosion Published Since 1960', Corrosion, vol. 27, no. 6, June, pp. 223-233.

Szklarska-Smialowska, Z. (1999) 'Pitting Corrosion of Aluminium', Corrosion Science, vol. 41, no. 5, September, pp. 1743-1767.

Szklarska-Smialowska (2005) Pitting and Crevice Corrosion, 1st edition, Houston: NACE.

Tait, W. (1994) An Introduction to Electrochemical Corrosion Testing For Practing Engineers and Scientists, California: PairODocs Publications.

Tan, Y. (2013) Heterogeneous Electrode Processes and Localized Corrosion, 1st edition, New Jersey: John Wiley & Sons.

Trasatti, S. (1986) 'The Absolute Electrode Potential: An Expanation Note', Pure and Applied Chemistry, vol. 58, no. 7, June, pp. 955-966.

Trethewey, K. and Chamberlain, J. (1998) Corrosion for Science and Engineering, 2nd edition, Harlow: Longman.

Videm, K. (1974), Proceedings on 5th International Congress on Metallic Corrosion, Huston, 264.

Waber, T. (1954) 'Mathematical Studies on Galvanic Corrosion : I. Coplanar Electrodes with Negligible Polarisation ', Journal of the Electrochemical Society, vol. 101, no. 6, June, pp. 271 -276.

Waber, J. and Rosenblunt, M. (1955) 'Mathematical Studies of Galvanic Corrosion : II. Coplanar Electrodes with One Electrode Infinitely Large and with Equal Polarization Parameters', Journal of the Electrochemical Society, vol. 102, no. 6, June, pp. 344-353.

Wagner, C. (1951) 'Theoretical Analysis of the Current Density Distribution in Electrolytic Cells', Journal of the Electrochemical Society, vol. 98, no. 3, March, pp. 116-128.

Wagner, C. and Traud, W. (1938) 'On the Interpretation of Corrosion processes Through the Superposition of Electrochemical Partial Processes and the Potential of Mixed Electrodes', Zeitschrift fur Electrochemie, vol. 44, no. 7, Jully, pp. 391-402.

Walker, M. and Rowe, L. (1969) 'The Application of Electrochemical Techniques to the Study of Corrosion Of Automotive Trim Materials', Corrosion, vol. 25, no. 2, February, pp. 47-58.

Wang, W., Lartigue-Korinek, S., Brisset, F., Helbert, A., Bourgon, J. and Baudin, T. (2015) 'Formation of Annealing Twins during Primary Recrystalization of Two Low Stacking Fault Energy Ni-Based Alloys', Journal of Material Science, vol. 50, no. 12, December, pp. 2167-2177.

Zhang, J. (Ed.) (2008) PEM Fuel Cell Electrocatalysts and Catalyst Layers: Fundamentals and Applications, 1st edition, London: Springer.

APPENDICES

Appendix A

Material Certificate: Alloy 825

TW Ref: 32064288000 1 - Heat No.: 164133 - Customer: Lansefield Engineering Limited - Ref.: E8366 - Part: - Printed on: 20/12/2011 16:23:08

325/1220-8 164/23

ThyssenKrupp VDM

ThyssenKrupp VDM GmbH
Division
Plate & Sheet

Klefstraße 23 D-58762 Altena Tel. +49 2392 552092
Postbox 1251 D-58742 Altena Fax +49 2392 552047
EMail wilhelm.zoebe@thyssenkrupp.com

ThyssenKrupp

Inspection certificate 91910/0 Page 1 of 2
DIN EN 10204/01.05 3.1 printed: 29.06.2011

Order No. 386431
Delivery No. 613211
Trademark NICROFER 4221
2.4858

Philip Cornes & Co. LTD.

Majestic Road , Nursling Estat
GB - SO16 0AF Southampton

Product
plate, hot rolled, soft annealed, descaled, sheared

Specification	Material
ASTM B 424 - 05 (Reapproved 2009)	UNS N08825
ASME SB-424-2010	UNS N08825
BS 3072: 1989	NA 16
VDTÜVBL. 432/1 12.2009	NiCr21Mo
NACE MR0175-2003	

Item	Pcs	Wht [kg]	Dimension [mm]			Cast	Lot
8	1	10,000 x	2500,0 x	6000,0	164133	10344414	

Purchase Order No. M 32511220

LE=combustion analysis, RF=XRF

Analysis (weight %)
ASTM B 424 - 05 (Reapproved 2009): ASME SB-424-2010; BS 3072: 1989; VDTÜVBL. 432/1 12.2009

Cast	Melting Pr.	C	S	Cr	Ni	Mn	Si	Mo	Ti	Cu	Fe	P	Al	Co
164133	EF/VD	0,012	0,002	22,6	39,7	0,78	0,26	3,09	0,73	1,90	R30,4	0,017	0,15	0,15
	top Meth	LE	LE	RF	RF	RF	RF	RF	RF	RF	RF	RF	RF	RF

Lot	Sample No.	Temp [°C]	Yield 0.2% [MPa]	Yield 1.0% [MPa]	Tensile [MPa]	Elongation A [%]	Elongation A [%]
Sample Condition soft annealed		Tensile Test 1 ISO 6892-1 B10 2 EN 10002-5					
10344414	1-K1	2 250	185	222	515		
10344414	1-K1	2 450	166	209	515		
10344414	1-K1	1 RT	255	294	613	50	56

Hardness Test		
1 ASTM E 18	HRC	
		2 without objection
		1 <20 surface

Corrosion Test	
1 DIN EN ISO 3651-2 Meth. A	
2 DIN EN ISO 3651-2 Meth. A T. 1	
	2 without objection
	1 without objection

ISO 9001, AS9100, EN 9001
LRQA Approval
KLN 4000941/B

We herewith certify, that the material is in conformance with the above mentioned specifications Mark of the Inspector E

This certification was created by machine and is valid without signature Q

Wilhelm Zoebe, authorized inspection representative Date of release: 30.06.2011

91910-0- E

This certified test report shall not be reproduced except in full, without the written approval of ThyssenKrupp VDM. The recording of false, fictitious or fraudulent statements or entries on the certificate may be punished as a felony under federal law.

PHILIP CORNES
TEST CERTIFICATE CHECKED
Sig. signature removed
Date 3/8/11

Chemical Composition: Alloy 625

INCONEL® nickel-chromium alloy 625 (UNS N06625/W.Nr. 2.4856) is used for its high strength, excellent fabricability (including joining), and outstanding corrosion resistance. Service temperatures range from cryogenic to 1800°F (982°C). Composition is shown in Table 1.

Strength of INCONEL alloy 625 is derived from the stiffening effect of molybdenum and niobium on its nickel-chromium matrix; thus precipitation-hardening treatments are not required. This combination of elements also is responsible for superior resistance to a wide range of corrosive environments of unusual severity as well as to high-temperature effects such as oxidation and carburization.

The properties of INCONEL alloy 625 that make it an excellent choice for sea-water applications are freedom from local attack (pitting and crevice corrosion), high corrosion-fatigue strength, high tensile strength, and resistance to chloride-ion stress-corrosion cracking. It is used as wire rope for mooring cables, propeller blades for motor patrol gunboats, submarine auxiliary propulsion motors, submarine quick-disconnect fittings, exhaust ducts for Navy utility boats, sheathing for undersea communication cables, submarine transducer controls, and steam-line bellows. Potential applications are springs, seals, bellows for submerged controls, electrical cable connectors, fasteners, flexure devices, and oceanographic instrument components.

High tensile, creep, and rupture strength; outstanding fatigue and thermal-fatigue strength; oxidation resistance; and excellent weldability and brazeability are the properties of INCONEL alloy 625 that make it interesting to the aerospace field. It is being used in such applications as aircraft ducting systems, engine exhaust systems, thrust-reverser systems, resistance-welded honeycomb structures for housing engine controls, fuel and hydraulic line tubing, spray bars, bellows, turbine shroud rings, and heat-exchanger tubing in environmental control systems. It is also suitable for combustion system transition liners, turbine seals, compressor vanes, and thrust-chamber tubing for rocket

The outstanding and versatile corrosion resistance of INCONEL alloy 625 under a wide range of temperatures and pressures is a primary reason for its wide acceptance in the chemical processing field. Because of its ease of fabrication, it is made into a variety of components for plant equipment. Its high strength enables it to be used, for example, in thinner-walled vessels or tubing than possible with other materials, thus improving heat transfer and saving weight. Some applications requiring the combination of strength and corrosion resistance offered by INCONEL alloy 625 are bubble caps, tubing, reaction vessels, distillation columns, heat exchangers, transfer piping, and valves.

In the nuclear field, INCONEL alloy 625 may be used for reactor-core and control-rod components in nuclear water reactors. The material can be selected because of its high strength, excellent uniform corrosion resistance, resistance to stress cracking and excellent pitting resistance in 500°-600°F (260-316°C) water. Alloy 625 is also being considered in advanced reactor concepts because of its high allowable design strength at elevated temperatures, especially between 1200°-1400°F (649-760°C).

The properties given in this bulletin, results of extensive testing, are typical of the alloy but should not be used for specification purposes. Applicable specifications appear in the last section of this publication.

Table 1 – Limiting Chemical Composition, %

Nickel	58.0 min.
Chromium	20.0-23.0
Iron	5.0 max.
Molybdenum	8.0-10.0
Niobium (plus Tantalum)	3.15-4.15
Carbon	0.10 max.
Manganese	0.50 max.
Silicon	0.50 max.
Phosphorus	0.015 max.
Sulfur	0.015 max.
Aluminum	0.40 max.
Titanium	0.40 max.
Cobalt[a]	1.0 max.

[a]If determined

INCONEL® alloy 625

Seawater Certificate of Analysis

A.L. ABBOTT AND ASSOCIATES (PTY) LTD
(Reg. No. 1982/004379/07)

Consulting Analytical & Industrial Chemists
Specialists in Water & Waste Water Treatment
Telephone (021)448 6340/1
After Hours (021)712 0940
Telefax (021)448 6342
e-Mail Address :
info@alabbott.co.za

T0276

No. 1, Vine Park
Vine Road
7925
P.O. Box 483
WOODSTOCK, CAPE
7915

Doc.No. 5.10/1 Rev.3

Certificate of Analysis

UNIVERSITY OF CAPE TOWN
ANALYSIS (ORDER NO. 1485547)
SEA WATER

DATE SAMPLED : 2016/02/12
DATE RECEIVED : 2016/02/12
DATE ANALYSIS COMMENCED : 2016/02/12

OUR REF. : 2016/02/12/3416
REPORT NO . : 662

	Sample Number	3416	
Mthd ALA No.	**Analyses**	**Results**	**SANS 241-1:2015**
9	Conductivity (mS/m) (at 25 °C)	6675	≤170 Aesthetic
7	Total Dissolved Solids (mg/l)	46067	≤1200 Aesthetic
19	pH (at 25 °C)	7.07	≥5 - ≤9.7 Operational
24	Sulphate (mg/l as SO4)	2725	≤250 Aesthetic ≤500 Acute Health
29	Fluoride (mg/l as F)	1.9	≤1.5 Chronic Health
25	Chloride (mg/l as Cl)	20074	≤300 Aesthetic
92	Sodium (mg/l as Na)	9800	≤200 Aesthetic
28	Total Alkalinity (mg/l as CaCO3)	148	N/A
Calc	Bicarbonate mg/l	181	N/A
92	Strontium(µg/l as Sr)	678	N/A
92	Calcium (mg/l as Ca)	401	N/A
92	Potassium (mg/l as K)	200	N/A
92	Magnesium (mg/l as Mg)	1885	N/A
N/A	Bromide (mg/l)	22.0	N/A

Sampler : Unknown

A.L. ABBOTT AND ASSOCIATES (PTY) LTD

(Reg. No. 1982/004379/07)

Consulting Analytical & Industrial Chemists
Specialists in Water & Waste Water Treatment
Telephone (021)448 6340/1
After Hours (021)712 0940
Telefax (021)448 6342
e-Mail Address :
info@alabbott.co.za

T0276

No. 1, Vine Park
Vine Road
7925
P.O. Box 483
WOODSTOCK, CAPE
7915

Doc.No. 5.10/1 Rev.3

Certificate of Analysis

UNIVERSITY OF CAPE TOWN

ANALYSIS (ORDER NO. 1485547)

SEA WATER

DATE SAMPLED : 2016/02/12
DATE RECEIVED : 2016/02/12
DATE ANALYSIS COMMENCED : 2016/02/12

OUR REF. : 2016/02/12/3416
REPORT NO. : 662

	Sample Number	3416	
Mthd ALA No.	Analyses	Results	SANS 241-1:2015

signature removed

N. VAN BINSBERGEN (Pr.Sci.Nat.)
DIRECTOR
25 February 2016

TO: Centre for Materials Engineering
University Private bag
Rondebosch
7700

Att: Beverley Glass <beverley.glass@uct.ac.za> & Penny Park-Ross <penny.park-ross@uct.ac.za>

Sampler : Unknown

Appendix B:

Potentiodynamic Polarization Curves

In this section, some of the recorded potentiodynamic polarization curves for alloy 825, alloy 625 weld and alloy 825 weldment at different temperatures are presented.

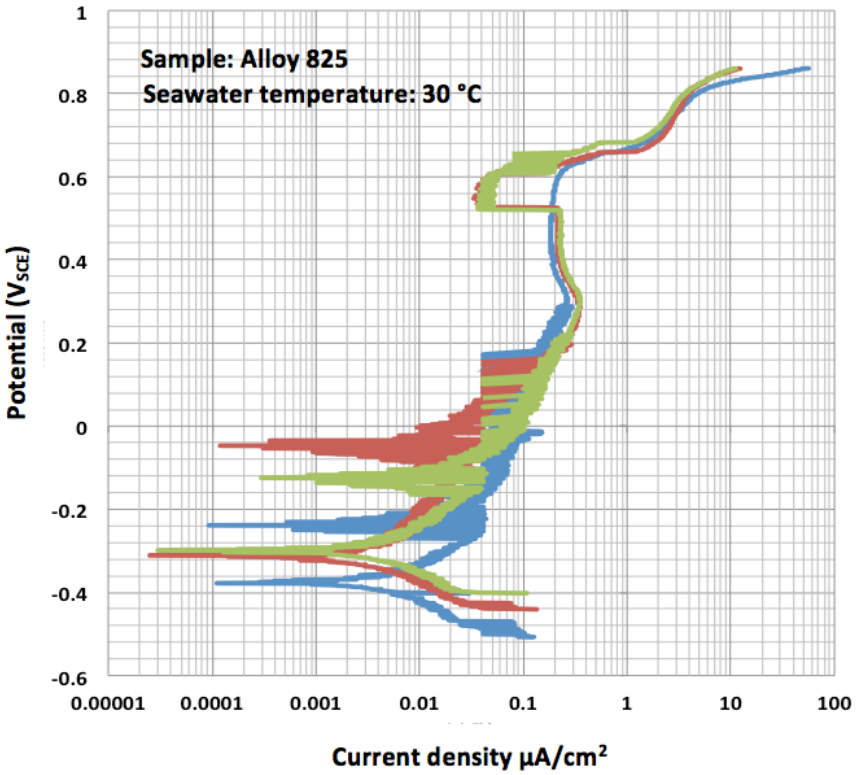

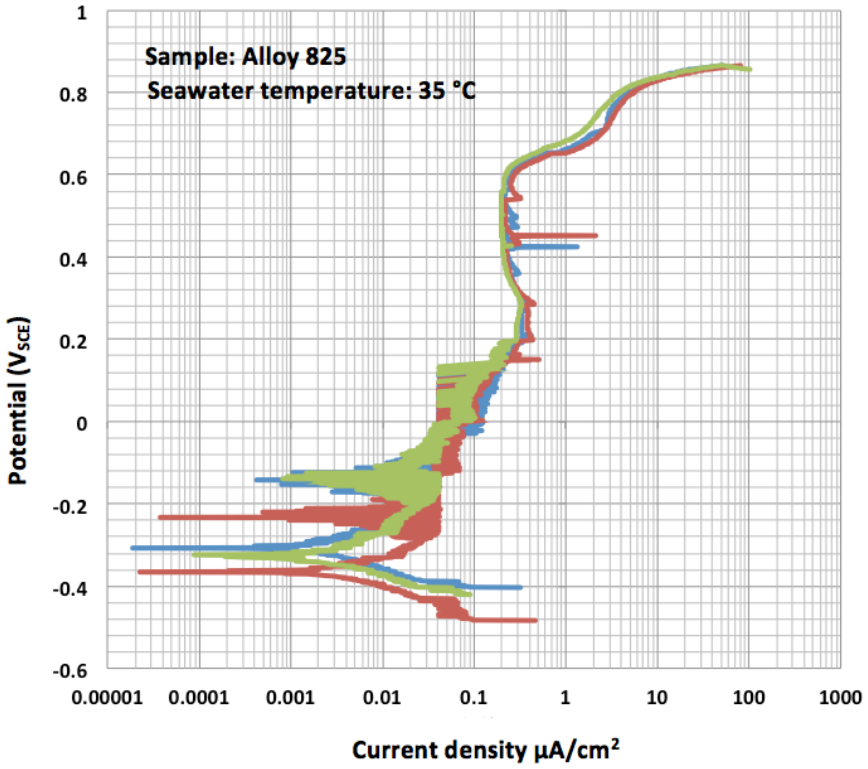
Sample: Alloy 825
Seawater temperature: 35 °C
Potential (V_{SCE})
1
0.8
0.6
0.4
0.2
0
-0.2
-0.4
-0.6
0.00001
0.0001
0.001
0.01
0.1
1
10
100
1000
Current density µA/cm²

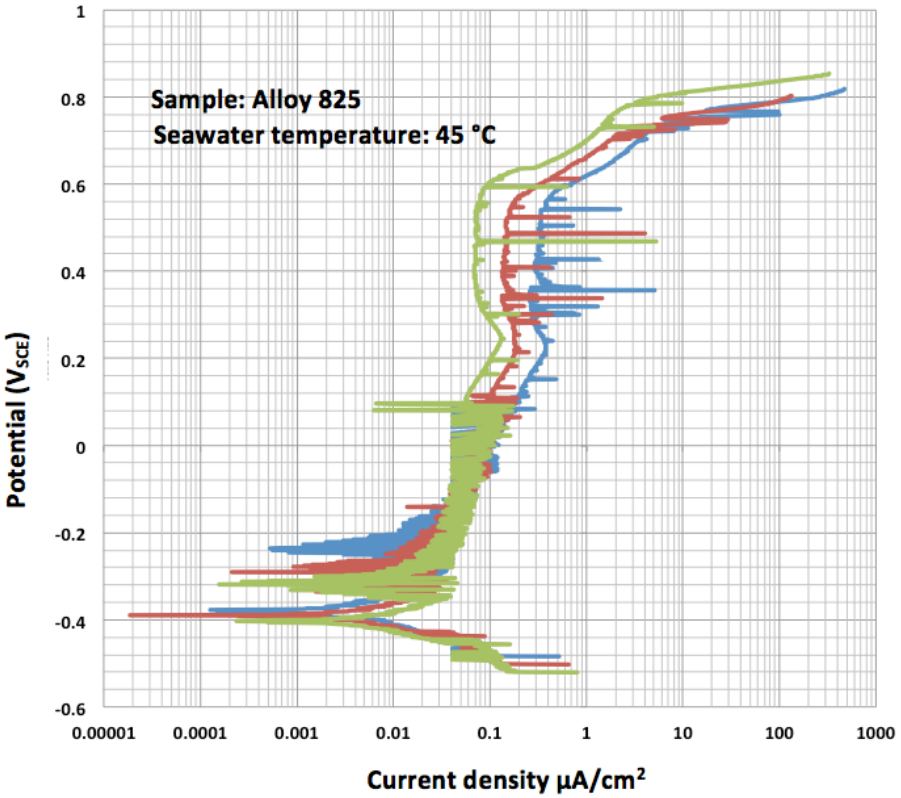
Sample: Alloy 825
Seawater temperature: 45 °C
Potential (V_{SCE})
1
0.8
0.6
0.4
0.2
0
-0.2
-0.4
-0.6
0.00001
0.0001
0.001
0.01
0.1
1
10
100
1000
Current density µA/cm²

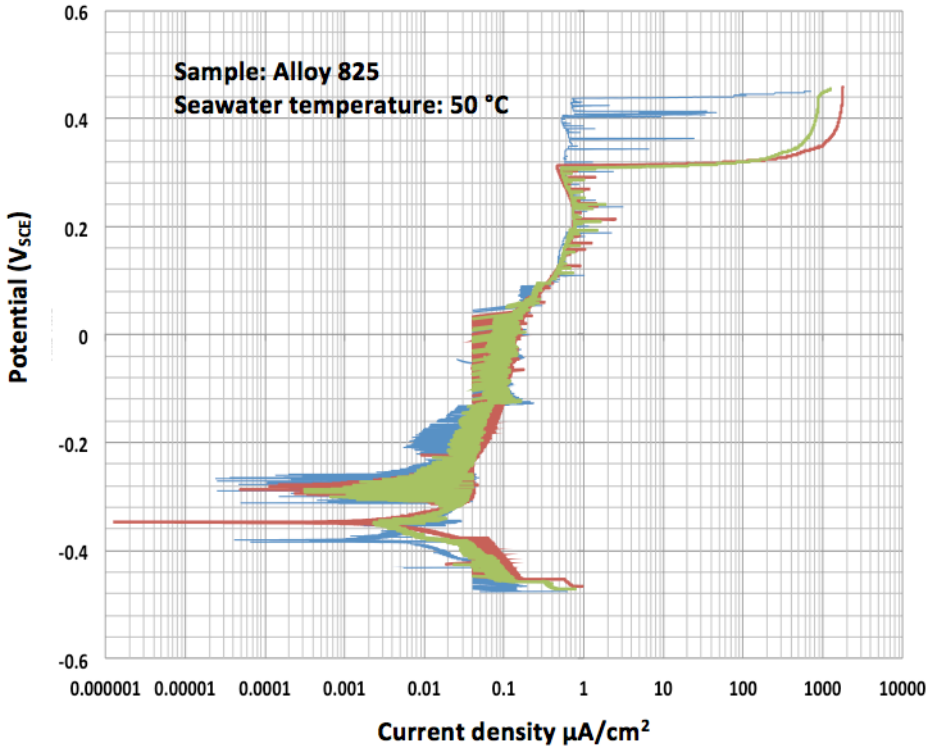
Sample: Alloy 825
Seawater temperature: 50 °C
Potential (V_{SCE})
0.6
0.4
0.2
0
-0.2
-0.4
-0.6
0.000001 0.00001 0.0001 0.001 0.01 0.1 1 10 100 1000 10000
Current density µA/cm²

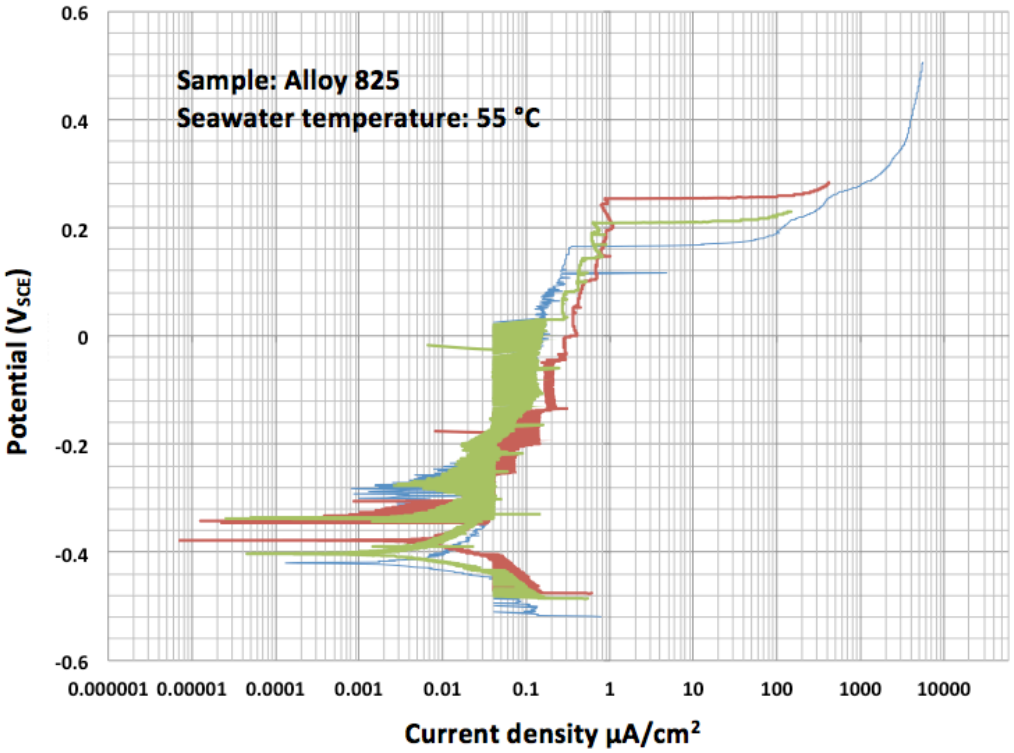
Sample: Alloy 825
Seawater temperature: 55 °C
Potential (V_{SCE})
0.6
0.4
0.2
0
-0.2
-0.4
-0.6
0.000001 0.00001 0.0001 0.001 0.01 0.1 1 10 100 1000 10000
Current density µA/cm²

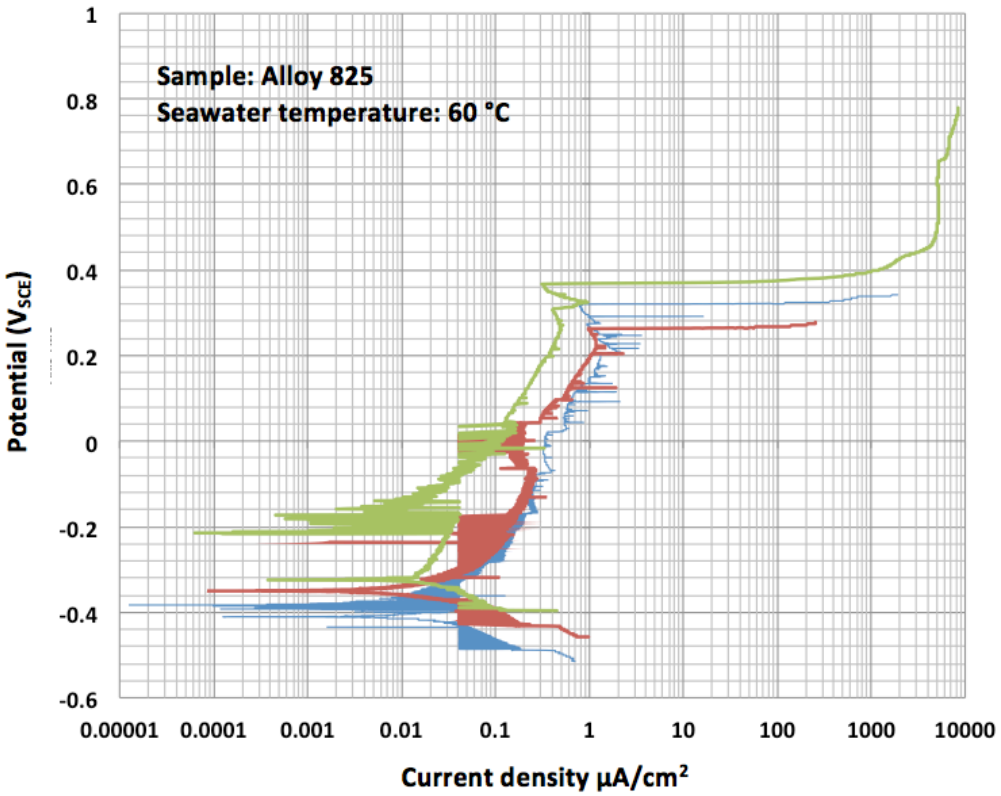
Sample: Alloy 825
Seawater temperature: 60 °C
Potential (V$_{SCE}$)
1
0.8
0.6
0.4
0.2
0
-0.2
-0.4
-0.6
0.00001
0.0001
0.001
0.01
0.1
1
10
100
1000
10000
Current density µA/cm^2

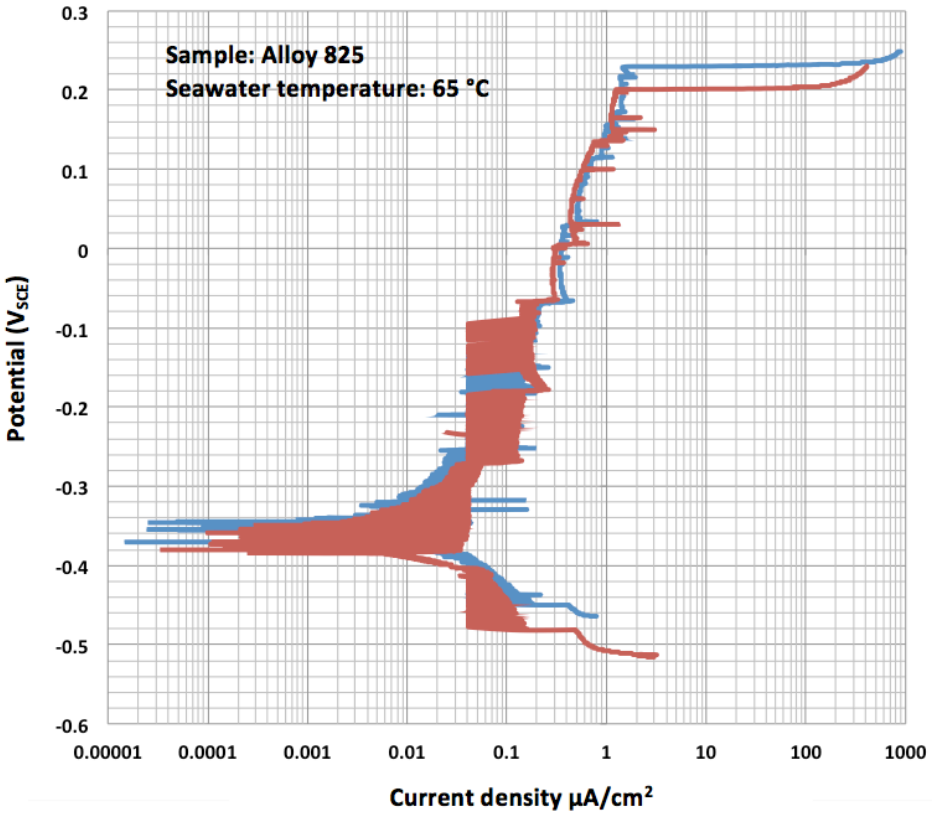
Sample: Alloy 825
Seawater temperature: 65 °C
Potential (V$_{SCE}$)
0.3
0.2
0.1
0
-0.1
-0.2
-0.3
-0.4
-0.5
-0.6
0.00001
0.0001
0.001
0.01
0.1
1
10
100
1000
Current density µA/cm^2

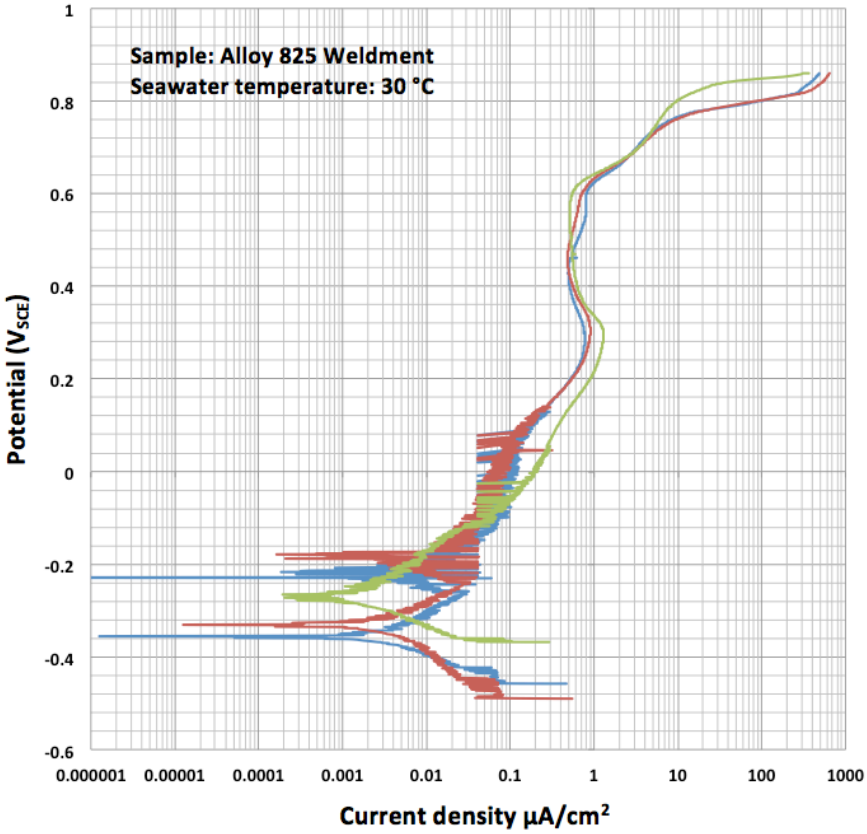
Sample: Alloy 825 Weldment
Seawater temperature: 30 °C
Potential (V_{SCE})
1
0.8
0.6
0.4
0.2
0
-0.2
-0.4
-0.6
0.000001
0.00001
0.0001
0.001
0.01
0.1
1
10
100
1000
Current density µA/cm²

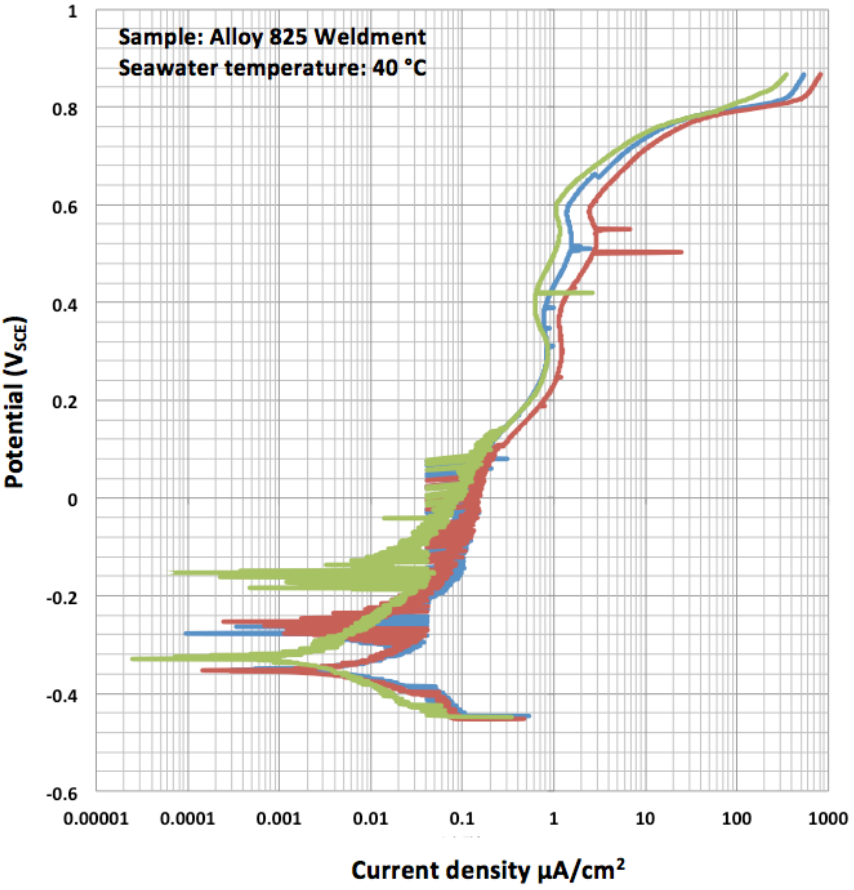
Sample: Alloy 825 Weldment
Seawater temperature: 40 °C
Potential (V_{SCE})
1
0.8
0.6
0.4
0.2
0
-0.2
-0.4
-0.6
0.00001
0.0001
0.001
0.01
0.1
1
10
100
1000
Current density µA/cm²

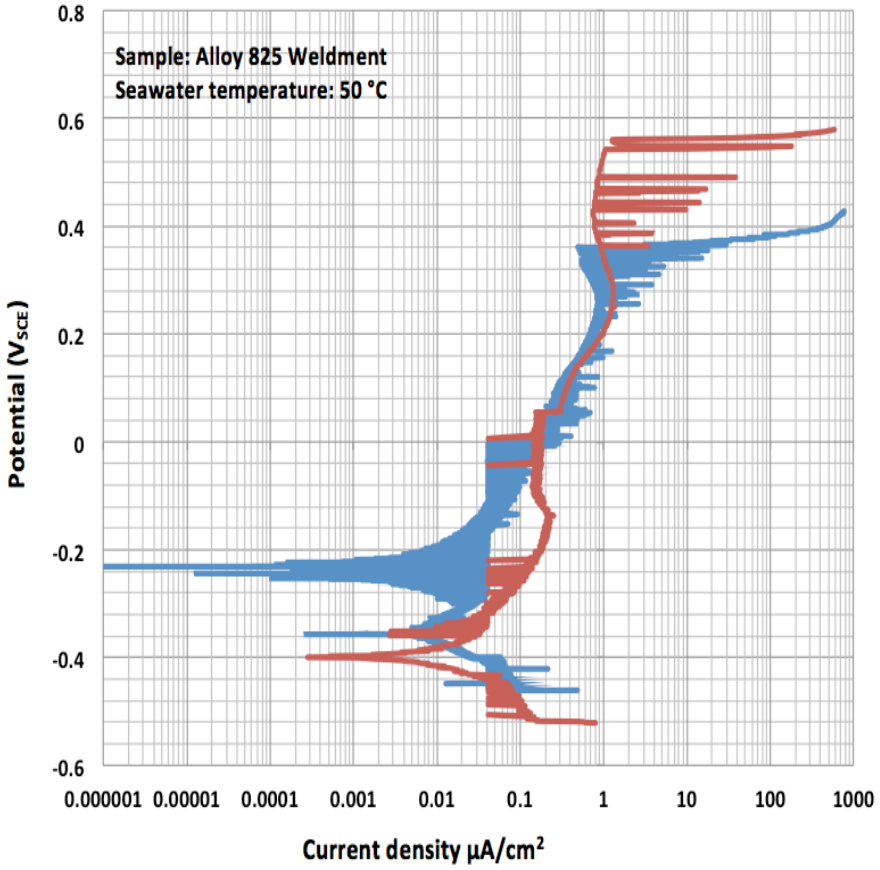
Sample: Alloy 825 Weldment
Seawater temperature: 50 °C
Potential (V_SCE)
0.8
0.6
0.4
0.2
0
-0.2
-0.4
-0.6
0.000001 0.00001 0.0001 0.001 0.01 0.1 1 10 100 1000
Current density µA/cm²

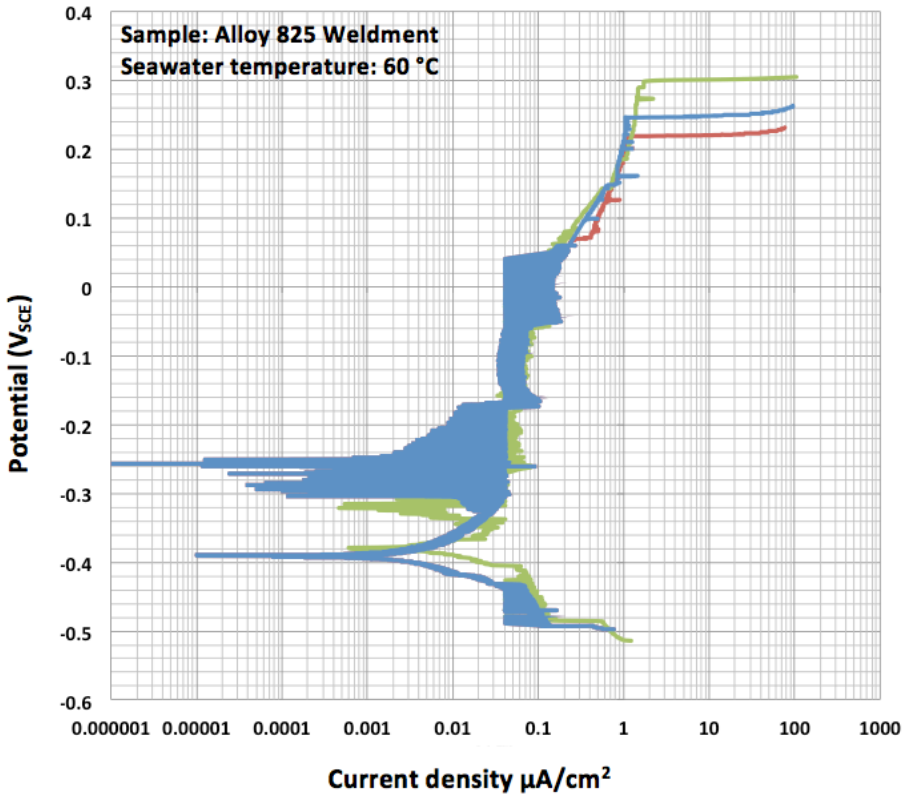
Sample: Alloy 825 Weldment
Seawater temperature: 60 °C
Potential (V_SCE)
0.4
0.3
0.2
0.1
0
-0.1
-0.2
-0.3
-0.4
-0.5
-0.6
0.000001 0.00001 0.0001 0.001 0.01 0.1 1 10 100 1000
Current density µA/cm²

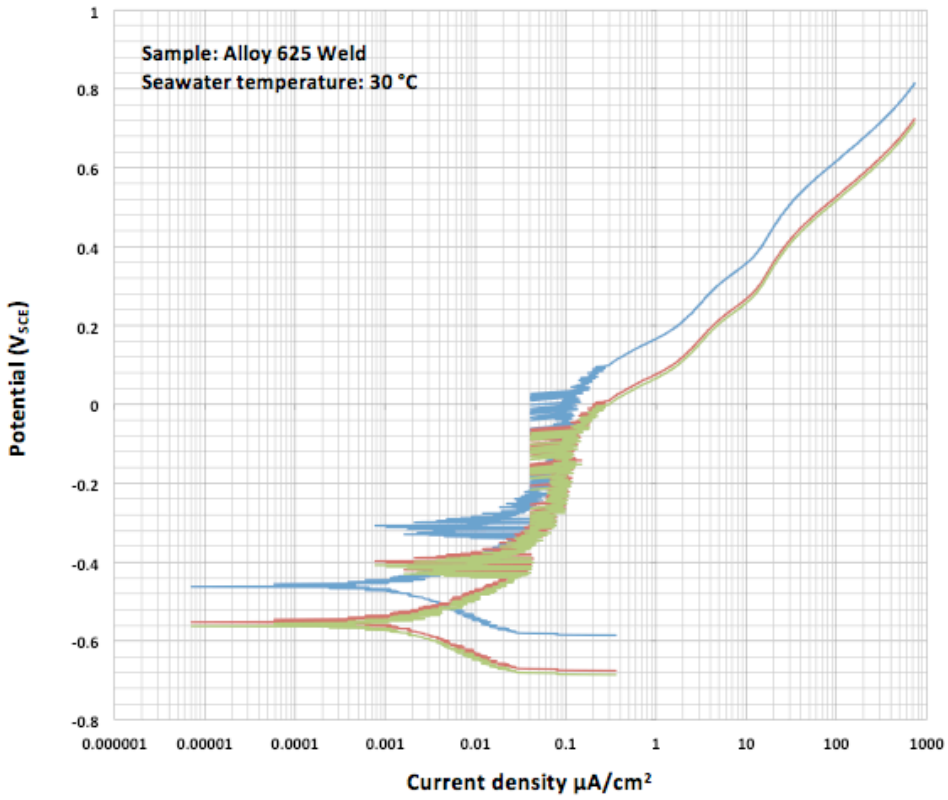
Sample: Alloy 625 Weld
Seawater temperature: 30 °C
Potential (V_{SCE})
1
0.8
0.6
0.4
0.2
0
-0.2
-0.4
-0.6
-0.8
0.000001
0.00001
0.0001
0.001
0.01
0.1
1
10
100
1000
Current density µA/cm²

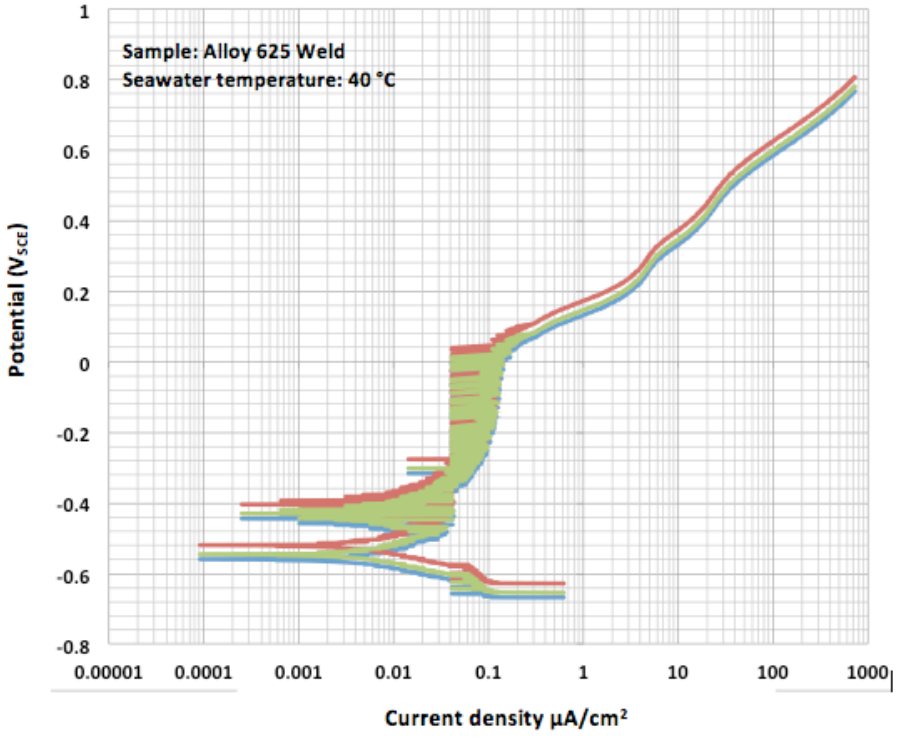
Sample: Alloy 625 Weld
Seawater temperature: 40 °C
Potential (V_{SCE})
1
0.8
0.6
0.4
0.2
0
-0.2
-0.4
-0.6
-0.8
0.00001
0.0001
0.001
0.01
0.1
1
10
100
1000
Current density µA/cm²

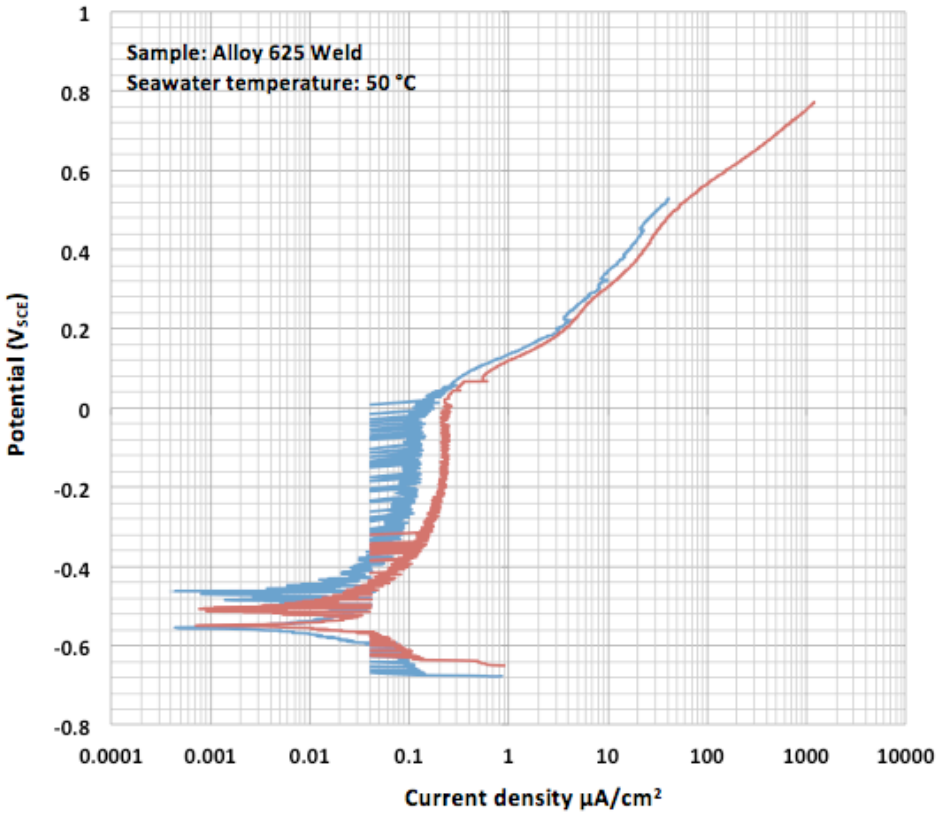
Sample: Alloy 625 Weld
Seawater temperature: 50 °C
Potential (V_{SCE})
1
0.8
0.6
0.4
0.2
0
-0.2
-0.4
-0.6
-0.8
0.0001
0.001
0.01
0.1
1
10
100
1000
10000
Current density µA/cm²

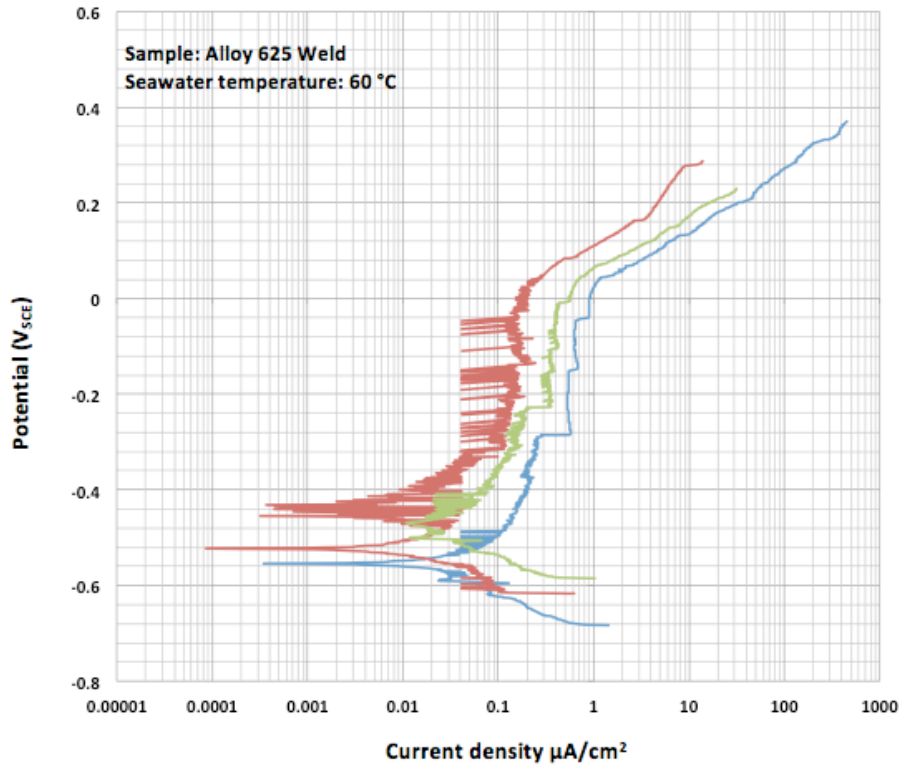
Sample: Alloy 625 Weld
Seawater temperature: 60 °C
Potential (V_{SCE})
0.6
0.4
0.2
0
-0.2
-0.4
-0.6
-0.8
0.00001
0.0001
0.001
0.01
0.1
1
10
100
1000
Current density µA/cm²

Appendix C

C1. Polarisation Curve Fitting

According to Goodman(1987) and Ives et al.(1991), the most common cathodic reactions driving the aqueous dissolution of a metal in seawater are reduction of oxygen or reduction of hydrogen cations. The pH of seawater (8.2) used in this work suggests that the predominant cathodic reaction at the surface of alloy 825 is oxygen reduction (equation 1):

$$O_2 + 2H_2O + 4e^- \rightarrow 4OH^- \qquad \text{(Equation 6.1)}$$

The relationship between the rate of the equation 6.1, expressed as cathodic current density and high values of the activation at the metal/solution interface is:

$$i_c = i_o \exp(\alpha n F \eta_{act}/RT) \qquad \text{(Equation 6.2)}$$

where α is the transfer coefficient; n the number of electrons involved in the reaction; F the Faraday's constant; η polarisation; R = 8.314 J/K*mol; T in Kelvin. Rearranging Equation 2 gives the Tafel equation:

$$\eta_{act,\,c} = b_c * \log(i_c/i_o) \qquad \text{(Equation 6.3)}$$

where b_c = Tafel slope= -2303RT/αnF

The reaction for active metal dissolution is $M \rightarrow M^{2+} + 2e^-$ and this is also described by Tafel equation:

$$i_a = i_o \exp((1-\alpha) n F \eta_{act}/RT) \qquad \text{(Equation 6.4)}$$

or $$\eta_{act,\,a} = b_a * \log(i_a/i_o) \qquad \text{(Equation.6.5)}$$

Resistance polarisation due to the presence of the passive film will also be present and the recorded potentials must be corrected for the IR drop.

In order to model a section of the polarisation curve (close to the corrosion potential) of the alloys 825 and 625, the values of the Tafel slopes and exchange current density of the equations 3 and 5 need to be guessed continuously until the shape of the theoretical curve much the experimental one. Finally, the theoretical (matched) curve is deconvoluted (deconstructed) to reveal the anodic and cathodic branches.

Figure 6.1 shows the experimental and matched section of alloy 825 polarisation curve.

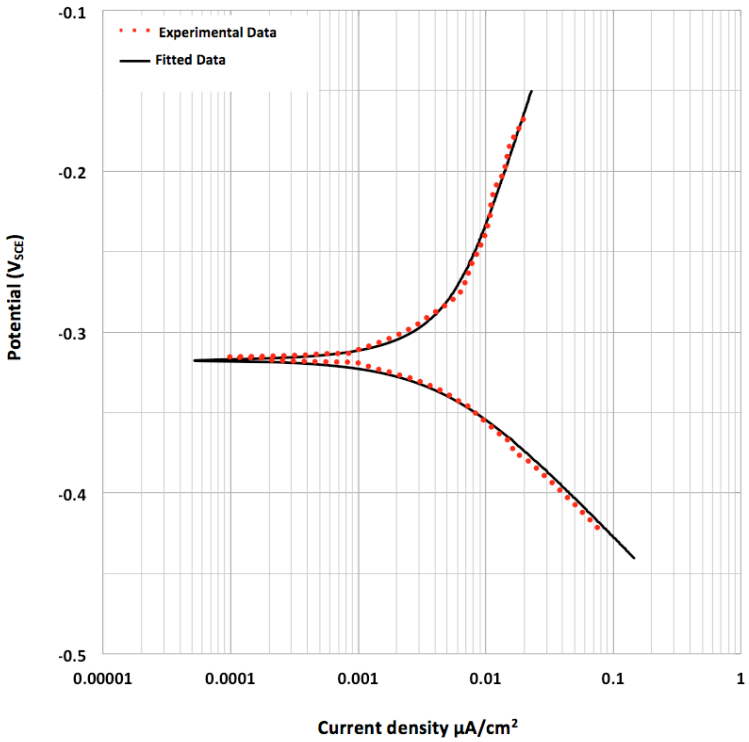

Figure 6.1 Experimental and theoretical section of alloy 825 polarisation curve, near its first corrosion potential

Table 6.1 and Table 6.2 summarise the constant parameters used to find the fitting curves for the experimental polarisation curves of alloy 825 and 625 respectively.

Alloy 825						
		Anode			Cathode	
Temperature	io	Eo	ba	io	Eo	bc
C	microA/cm2	mV	mV/dec	microA/cm2	mV	mV/dec
30	0.00006	-780	112	1.00E-06	18	-37
40	6.00E-05	-560	45	1.00E-06	70	-35
50	6.00E-05	-410	15	1.00E-06	233	-14
60	6.00E-05	-420	15	1.00E-06	255	-11.3
		Anode			Cathode	
Temperature	io	Eo	ba	io	Eo	bc
C	microA/cm2	mV	mV/dec	microA/cm2	mV	mV/dec
30	6.00E-05	-780	119	1.00E-06	18	-36
40	6.00E-05	-580	44	1.00E-06	70	-35
50	6.00E-05	-500	30	1.00E-06	263	-14
60	6.00E-05	-885	105	1.00E-06	85	-25
		Anode			Cathode	
Temperature	io	Eo	ba	io	Eo	bc
C	microA/cm2	mV	mV/dec	microA/cm2	mV	mV/dec
30	6.00E-05	-650	80	1.00E-06	18	-34.5
40	6.00E-05	-450	35	1.00E-06	95	-30
50	6.00E-05	-540	30	1.00E-06	265	-16
60	6.00E-05	-450	8.5	1.00E-06	330	-9

Table 6.1 Values of the parameters for theoretical polarisation curve of alloy 825 weld

Alloy 625						
		Anode			Cathode	
Temperature	io	Eo	ba	io	Eo	bc
C	microA/cm2	mV	mV/dec	microA/cm2	mV	mV/dec
30	6.00E-05	-620	45	1.00E-06	140	-43
40	6.00E-05	-728	38	1.00E-06	350	-25
50	6.00E-05	-640	20	1.00E-06	430	-15.5
60	6.00E-05	-725	29	1.00E-06	220	-34
		Anode			Cathode	
Temperature	io	Eo	ba	io	Eo	bc
C	microA/cm2	mV	mV/dec	microA/cm2	mV	mV/dec
30	6.00E-05	-645	50	1.00E-06	403	-36
40	6.00E-05	-584	40	1.00E-06	415	-34
50	6.00E-05	-650	21	1.00E-06	420	-14.5
60	6.00E-05	-592	25	1.00E-06	370	-30
		Anode			Cathode	
Temperature	io	Eo	ba	io	Eo	bc
C	microA/cm2	mV	mV/dec	microA/cm2	mV	mV/dec
30	6.00E-05	-596	45	1.00E-06	425	-40
40	6.00E-05	-640	43	1.00E-06	401	-36
50	6.00E-05	-621	25	1.00E-06	397	-18
60	6.00E-05	-679	29	1.00E-06	385	-33

Table 6.2 Values of the parameters for theoretical polarisation curve of alloy 625 weld

C2. Determination of Corrosion Potential and Current Density

Figure 6.2 shows the modeled polarisation curve for alloy 825 and its anodic and cathodic branches. It is worth mentioning that the modeled polarisation curve (black line) results from the sum of the anodic and cathodic components (green lines).

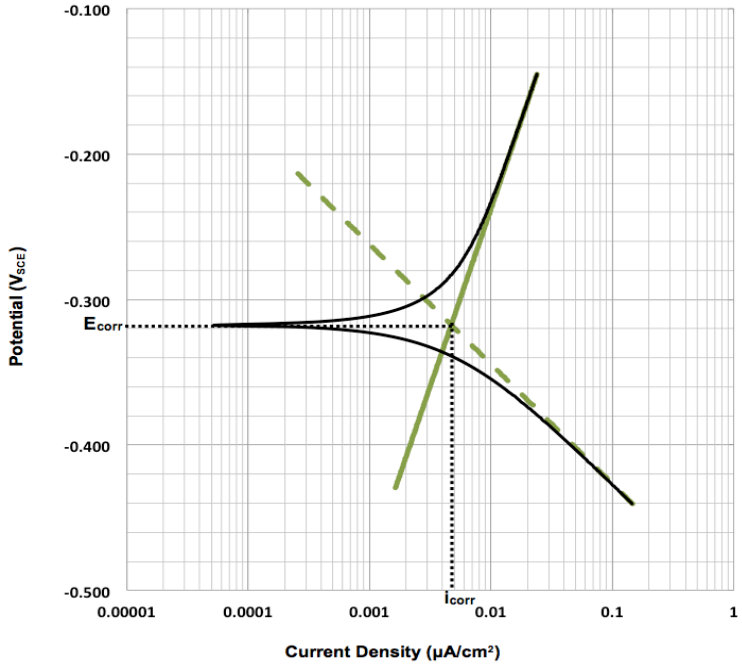

Figure 6.2 Fitted polarisation curve of alloy 825 plus its anodic and cathodic components

A straight line fitted across approximately a decade of the linear portion of the measured cathodic curve will represent the Tafel slope. The anodic branch also shows some linearity but it is not an indication of Tafel region because the anodic branch of the experimental curve represents the dissolution of various alloying elements. However, a reasonable estimation of the corrosion current density may be determined from the intersection of E_{corr} with the anodic and cathodic components of the matched curves (Flitt and Schweinsberg, 2010).

Table 6.3 summarises the corrosion current densities and potentials at different temperatures, these parameters were determined using the technique illustrated in Figure 6.2.

	Alloy 825		Alloy 625	
Temperature	**icorr**	**Ecorr**	**icorr**	**Ecorr**
C	**microA/cm2**	**V**	**microA/cm2**	**V**
30	3.60E-03	-0.317	5.06E-03	-0.461
40	4.58E-03	-0.361	1.11E-02	-0.558
50	3.69E-03	-0.344	8.68E-03	-0.553
60	5.35E-03	-0.348	4.84E-02	-0.553

	Alloy 825		Alloy 625	
Temperature	**icorr**	**Ecorr**	**icorr**	**Ecorr**
C	**microA/cm2**	**V**	**microA/cm2**	**V**
30	3.35E-03	-0.316	5.50E-03	-0.561
40	5.74E-03	-0.367	1.20E-02	-0.523
50	4.72E-03	-0.377	7.82E-03	-0.549
60	3.31E-03	-0.322	4.12E-02	-0.525

	Alloy 825		Alloy 625	
Temperature	**icorr**	**Ecorr**	**icorr**	**Ecorr**
C	**microA/cm2**	**V**	**microA/cm2**	**V**
30	4.37E-03	-0.307	6.12E-03	-0.559
40	4.65E-03	-0.34	1.15E-02	-0.556
50	4.30E-03	-0.329	1.62E-02	-0.542
60	7.25E-03	-0.41	4.25E-02	-0.562

Table 6. Corrosion current density and potential of alloys 825 and 625 at different temperatures

C3. Determination of the Galvanic Current Density and Potential According to the Mixed Potential for Two Metals

Figure 6.3 shows sections of the modeled polarisation curves for uncouple alloys 825 & 625 weld as well as theirs anodic and cathodic branches. The area ratio of alloy 825 to alloy 625 in weldment is 2.4 (see Figure 4.17). Therefore, factor of 2.4 was used to adjust the current density of alloy 625 in the couple condition.

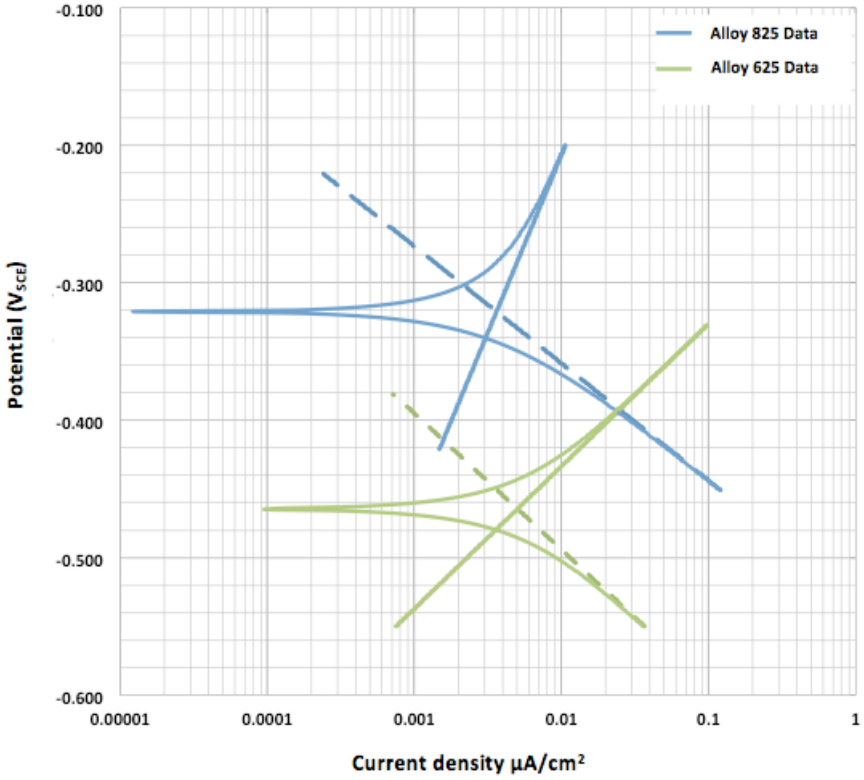

Figure 6.3 Modeled curves for alloys 825 & 625 as well as theirs anodic and cathodic branches

According to the mixed potential theory on two metals (Boboian et al., 1976: 7), the galvanic potential and current densities of the alloy 825 coupled to alloy 625 weld lies where the total oxidation and reduction component (orange lines in Figure 6.4) of the system intercepts. Since alloy 625 weld is the anodic component in the couple, its corrosion current density increases to $i_{corr\ B'}$ and alloy 825 corrosion rate reduces to $i_{corr\ A'}$.

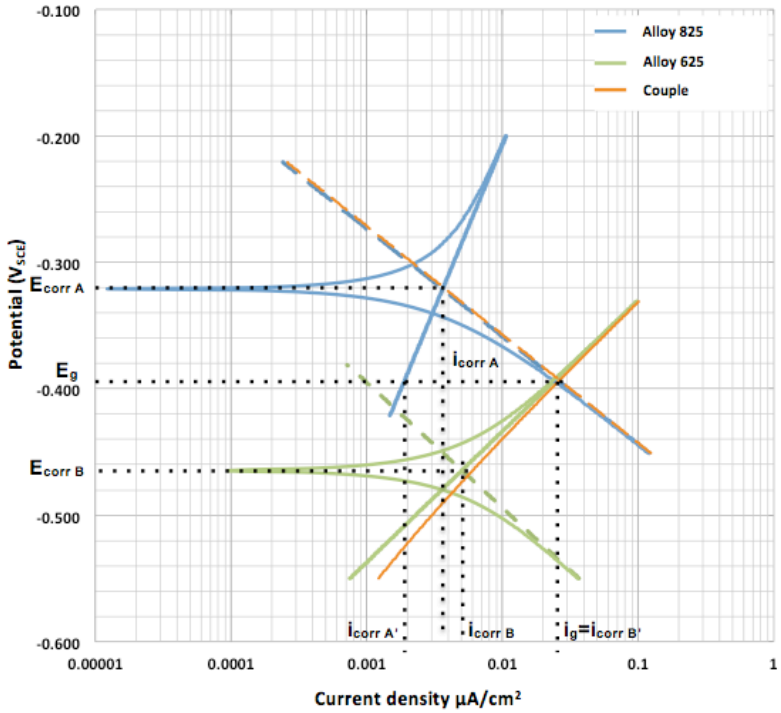

Figure 6.4 Mixed potential behaviour for the galvanic couple alloys 825 & 625

Table 6.4 summarises the galvanic currents and potentials at different temperatures, determined according to mixed potential theory for two metals for the galvanic couple alloys 825 and 625 (Figure 6.4).

Galvanic Parameters				
Temperature	**Eg**	**ig**	**icorr A'**	**Icorr B'**
C	**V**	**microA/cm2**	**microA/cm2**	**microA/cm2**
30	-0.393	2.62E-02	1.90E-03	2.46E-02
40	-0.476	1.09E-01	3.88E-04	1.09E-01
50	-0.442	2.87E+00	7.11E-05	2.87E+00
60	-0.427	3.18E+00	3.76E-05	3.18E+00
Temperature	**Eg**	**ig**	**icorr A'**	**icorr B'**
C	**V**	**microA/cm2**	**mV/dec**	**microA/cm2**
30	-0.421	3.83E-02	4.50E-04	3.26E-02
40	-0.437	1.14E-01	8.23E-05	1.27E-01
50	-0.46	2.52E+00	2.35E-04	2.52E+00
60	-0.435	3.07E+00	4.49E-03	3.06E+00
Temperature	**Eg**	**ig**	**icorr A'**	**Icorr B'**
C	**microA/cm2**	**mV**	**mV/dec**	**microA/cm2**
30	-0.452	2.51E-02	2.51E-03	2.74E-02
40	-0.433	1.10E-01	6.43E-04	1.15E-01
50	-0.4247	2.34E+00	8.54E-05	2.04E+00
60	-0.459	3.04E+00	5.62E-04	3.06E+00

Table 6.3 Galvanic currents and potentials of alloys 825 & 625 in couple form at different temperatures

C4. Corrosion Activation Energy

The effect of temperature on the corrosion rate is evaluated using the Arrhenius equation:

$$\log(i_{corr}) = -\frac{E_a}{RT} + \log k \qquad \text{(Equation 6.6)}$$

Where i_{corr} is the corrosion current density, E_a is the apparent activation corrosion energy, R is the universal gas constant, T is the absolute temperature in K and k is the Arrhenius pre-exponential constant. Table 6.5 summarises the absolute values for the logarithm of the corrosion current density as a function of the inverse of absolute temperature. According to equation 6.6, the plot between log (i_{corr}) and 1/T for both alloys, produce straight lines, which slopes represent the corrosion activation energy.

	Uncouple		Couple	
1/T	log(Icorr)_ (alloy 825)	log(Icorr)_ (alloy 625)	log(icor)r_(alloy 825)	log(icorr)_(alloy 625)
1/K	µA/cm2	µA/cm2	µA/cm2	µA/cm2
0.00330	2.44348	2.29594	2.72121	1.60947
0.00319	2.33952	1.95434	3.41117	0.96158
0.00310	2.43258	2.06138	4.14834	0.45787
0.00300	2.27199	1.31516	4.42452	0.50234

	Uncouple		Couple	
			log(icorr)_(alloy 825)	log(icorr)_(alloy 625)
1/T	log(Icorr)_ (alloy 825)	log(Icorr)_ (alloy 625)	µA/cm2	µA/cm2
1/K	µA/cm2	µA/cm2	2.87290	
0.00330	2.4750	2.25964	3.34679	1.60947
0.00319	2.2411	1.92082	4.08460	0.96158
0.00310	2.3260	2.10693	3.62832	0.45787
0.00300	2.4803	1.38555	2.34818	0.50234

	Uncouple		Couple	
1/T	log(Icorr)_(alloy 825)	log(Icorr)_(alloy 625)	log(icorr)_(alloy 825)	log(icorr)_(alloy 625)
1/K	µA/cm2	µA/cm2	µA/cm2	µA/cm2
0.00330	2.359817	2.21325	2.60033	1.56209
0.00319	2.332547	1.93930	3.19179	0.94044
0.00310	2.366532	1.78968	4.06839	0.30886
0.00300	2.139662	1.37120	3.25026	0.48528

Table 6.4 Absolute value of the log(icorr) vs. 1/T for alloys 825 and 625 in the couple and uncouple conditions

Appendix D:

D1. Corrosion Penetration Rate Calculation

According to Jones (1996: 77), the equivalence for alloys 825 and 625 between current density and penetration rate is 1 μA/cm^2 = 0.40 mpy. The unit **mpy** continues as the most frequently used corrosion rate expression in the Unites States. However, with increasing use of the metric units in recent years, engineers are becoming more familiar with **mm/yr** and **μm/yr** for high and low corrosion rates respectively. The conversion from mpy to the equivalent metric penetration rates is: 1mpy = 0.0025 mm/yr = 25.4 μm/yr = 2.90nm/h (Fontana, 1987: 172).

Using the information above, one can calculate the equivalence for alloys 825 and 625 between current density (μA/cm^2) and penetration rate (μm/yr). For example, for the corrosion current densities of 3.6*10^{-3} μA/cm^2 and 5.06*10^{-3} μA/cm^2 for alloys 825 and 625 respectively, the penetration corrosion rates can be found as follow:

$$r_{alloy825} = \frac{3.6 * 10^{-3} \mu A / cm^2 * 0.4 \text{ mpy} * 25.4 \ \mu m/yr}{1 \ \mu A / cm^2 * 1 \text{ mpy}} = 36.57 * 10^{-3} \mu m / yr$$

$$r_{alloy625} = \frac{5.06 * 10^{-3} \mu A / cm^2 * 0.4 \text{ mpy} * 25.4 \ \mu m/yr}{1 \ \mu A/cm^2 * 1 \text{ mpy}} = 51.41 * 10^{-3} \mu m / yr$$

Table 6. 6 and Table 6. 7 summarise the corrosion current densities, galvanic currents and their equivalent penetration corrosion rates for alloys 825 and 625 at different temperatures.

	Alloy 825		Alloy 625	
Temperature	icorr	r	icorr	r
C	microA/cm2	microm/yr	microA/cm2	microm/yr
30	3.60E-03	3.66E-02	5.06E-03	5.14E-02
40	4.58E-03	4.65E-02	1.11E-02	1.13E-01
50	3.69E-03	3.75E-02	8.68E-03	8.82E-02
60	5.35E-03	5.43E-02	4.84E-02	4.92E-01
	Alloy 825		Alloy 625	
Temperature	icorr	r	icorr	r
C	microA/cm2	microm/yr	microA/cm2	microm/yr
30	3.35E-03	3.40E-02	5.50E-03	5.59E-02
40	5.74E-03	5.83E-02	1.20E-02	1.22E-01
50	4.72E-03	4.80E-02	7.82E-03	7.94E-02
60	3.31E-03	3.36E-02	4.12E-02	4.18E-01
	Alloy 825		Alloy 625	
Temperature	icorr	r	icorr	r
C	microA/cm2	microm/yr	microA/cm2	microm/yr
30	4.37E-03	4.44E-02	6.12E-03	6.22E-02
40	4.65E-03	4.72E-02	1.15E-02	1.17E-01
50	4.30E-03	4.37E-02	1.62E-02	1.65E-01
60	7.25E-03	7.37E-02	4.25E-02	4.32E-01

Table 6.5 Corrosion current densities and penetration rates for alloy 825 and 625 at different temperatures

Galvanic Parameters						
Temperature C	ig microA/cm2	rg microm/yr	icorr A' microA/cm2	rA' microm/yr	Icorr B' microA/cm2	rB' microm/yr
30	2.62E-02	2.66E-01	1.90E-03	1.93E-02	2.46E-02	2.50E-01
40	1.09E-01	1.11E+00	3.88E-04	3.94E-03	1.09E-01	1.11E+00
50	2.87E+00	2.92E+01	7.11E-05	7.22E-04	2.87E+00	2.92E+01
60	3.18E+00	3.23E+01	3.76E-05	3.82E-04	3.18E+00	3.23E+01
Temperature C	ig microA/cm2	rg microm/yr	icorr A' microA/cm2	rA' microm/yr	icorr B' microA/cm2	rB' microm/yr
30	3.83E-02	3.89E-01	4.50E-04	4.57E-03	3.26E-02	3.31E-01
40	1.14E-01	1.16E+00	8.23E-05	8.36E-04	1.27E-01	1.29E+00
50	2.52E+00	2.56E+01	2.35E-04	2.39E-03	2.52E+00	2.56E+01
60	3.07E+00	3.12E+01	4.49E-03	4.56E-02	3.06E+00	3.10E+01
Temperature C	ig microA/cm2	rg microm/yr	icorr A' microA/cm2	rA' microm/yr	Icorr B' microA/cm2	rB' microm/yr
30	2.51E-02	2.55E-01	2.51E-03	2.55E-02	2.74E-02	2.78E-01
40	1.10E-01	1.12E+00	6.43E-04	6.53E-03	1.15E-01	1.17E+00
50	2.34E+00	2.38E+01	8.54E-05	8.68E-04	2.04E+00	2.07E+01
60	3.04E+00	3.09E+01	5.62E-04	5.71E-03	3.06E+00	3.11E+01

Table 6.6 Galvanic current densities and their equivalent corrosion penetration rate ate different temperatures

D2. Relative Dissolution Rate Calculation

Mansfeld & Kenkel (1976: 20) have proposed the relative dissolution rate as a way to check the compatibility of dissimilar alloys in the galvanic couple.

$$\frac{r_a - r_o}{r_o} = \frac{i_g}{i_{corrA}} \qquad \text{(Equation 6.7)}$$

were, r_a and r_O are the dissolution rate of the anode metal in the couple and uncoupled conditions respectively, while i_g is the galvanic current and i_{corrA} is the current density of the anode metal in the uncoupled condition respectively. For the galvanic couple considered in this report, alloy 625 is the anodic component. Therefore the relative dissolution rate is given by ratio between the predicted galvanic current (Table 6.7) and the corrosion current density of alloy 625 in the uncouple condition (Table 6.6). Table 6.7 summarises the dissolution rate for the alloys 825 & 625 couple for different temperatures.

Temperature C	Alloy 625 icorr microA/cm2			Galvanic current ig microA/cm2			Relative dissolution Rate ig/icorr		
30	5.06E-03	5.50E-03	6.12E-03	2.62E-02	3.83E-02	2.51E-02	5.2	7.0	4.1
40	1.11E-02	1.20E-02	1.15E-02	1.09E-01	1.14E-01	1.10E-01	9.9	9.5	9.6
50	8.68E-03	7.82E-03	1.62E-02	2.87E+00	2.52E+00	2.34E+00	330.6	322.8	144.3
60	4.84E-02	4.12E-02	4.25E-02	3.18E+00	3.07E+00	3.04E+00	65.7	74.5	71.5

Table 6.7 Alloy 625 corrosion current density, galvanic current density and the relative dissolution rate at different temperatures

D3. Wagner Number and Polarisation

Wagner number is used to check the distribution of the galvanic current density and corrosion potential in a galvanic couple. The Wagner number is given by the ratio between the critical dimension (x), which is the half the dimension of the anodic member in the galvanic couple, and the Wagner polarisation parameter (δ) (Waber, 1954). Depending whether the critical dimension is larger or smaller than the Wagner polarisation parameter, the potential and current density of a galvanic couple may be uniformly distributed or vary along the distance away from the couple junction.

The polarisation parameter has the dimension of length and is defined by Wagner (1951) as:

$$\delta = \sigma \left| \frac{d\Delta E}{di} \right| = \frac{R_P}{R_o} \qquad \text{(Equation 6.8)}$$

Where σ is the specific conductivity of the medium, ΔE and i are the overvoltage and current density of the anodic metal or electrode respectively, R_o is the resistivity of the medium and R_P is the polarisation resistance of the anodic metal. The test solution used in corrosion experiment is seawater and its resistivity is calculated from the electrical conductivity i.e. R_o =1/conductivity, where the values of seawater resistivity are reported in Ω/cm. Conductivity as well as the resistivity of seawater are temperature dependent. A typical temperature dependence data set for seawater from 0 to 30 ºC is shown in Figure 6.7 (Ed. Lide, 2008).

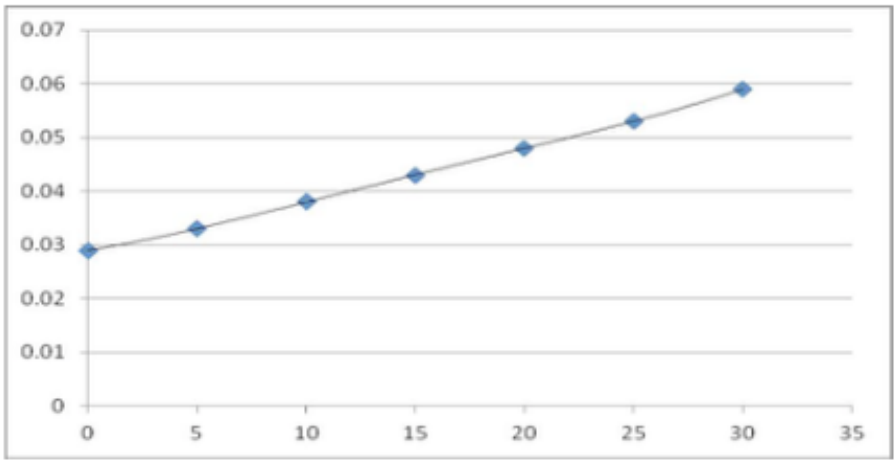

Figure 6.5 Dependence of Conductivity (S/cm) of seawater on temperature over the range 0 to 30 °C (Ed. Lide, 2008)

According to Figure 6.7, the conductivity of seawater at 10 ºC and 25 ºC are roughly 0.038013 S/cm and 0.053088 S/cm respectively. The values of the seawater resistivity are given by the inverse of the conductivity:

$$R_{10^{\circ}C} = \frac{1}{k_{10^{\circ}C}} = \frac{1}{0.038013\ S/cm} = 26.307\ \Omega/cm$$

$$R_{25^{\circ}C} = \frac{1}{k_{25^{\circ}C}} = \frac{1}{0.053088\ S/cm} = 18.837\ \Omega/cm$$

(Equation 6.9 & 6.10)

The linear dependence of conductivity and resistivity on the temperature as shown in Figure 6.7 , allows extrapolation of seawater conductivity and resistivity at higher temperatures. Therefore, conductivity k_x at temperature T_x can be calculated by using the following equation (Analytical, 2004):

$$k_x = k_{25^{\circ}C}\left(1 + \theta * (T_x - T_{25^{\circ}C})\right) \qquad \text{(Equation 6.11)}$$

Where $k_{25^{\circ}C}$ and $T_{25\ ^{\circ}C}$ are the conductivity and temperature of seawater at 25 ºC respectively, θ is the slope or temperate and is calculated by the following equation:

$$\theta = \frac{(k_{T2} - k_{T1})}{(T_2 - T_1) * k_{T1}} \qquad \text{(Equation 6.12)}$$

For the graph in Figure 6.7, the temperature coefficient is:

$$\theta = \frac{(0.053088 - 0.038013)\ S/cm}{(25 - 10)\ ^{\circ}C * 0.053088\ S/cm} = 0.0189\ ^{\circ}C^{-1}$$

Table 6.9 summarises the extrapolated values of seawater conductivity and resistivity using equation 11.

	Seawater	
Temperature	Conductivity	Resistivity
T	k	Ro
ºC	s/cm	Ω/cm
30	0.0581	17.21
40	0.0681	14.68
50	0.0782	12.79
60	0.0882	11.34

Table 6.8 Seawater conductivity and resistivity at different temperatures

The expression for polarisation resistance of the anodic metal (Rp) was derived by Stern and Geary (1957) as follow:

$$R_p = \frac{b_a b_c}{2.3 * (b_a + b_c) * i_{corr}} \qquad \text{(Equation 13)}$$

Where i_{corr} is the corrosion current density of the anodic metal in the couple (alloy 625 weld) , ba and bc are the tafel slopes. The width of the alloy 625 filler metal in the alloy 825 weldment is 5 mm, therefore the critical dimension (x) is 2.5 mm. Table 6. 10 a-c summarises the seawater resistivity extracted from Table 6. 8, tafel slopes from Figure 6.7, corrosion current density for alloy 625 in coupled condition from Table 6.4, polarisation resistance of alloy 625 in the couple condition , calculated using Equation 13, Wagner parameter calculated using equation 6.8 and the Wagner number, which is the ratio between the critical dimension and the Wagner parameter.

Temperature	Seawater Res	Polarisation Parameters		Polarisation Res	Wagner Par	
T	Ro	ba	bc	Rp	δ	X/δ
C	Ω/cm	mV	mV	Ω	cm	
30	17.21	45	43	388.99	22.60	0.11
40	14.68	38	25	266.76	18.18	0.14
50	12.79	28	23	223.39	17.46	0.14
60	11.34	29	34	276.87	24.42	0.10

Temperature	Seawater Res	Polarisation Parameters		Polarisation Res	Wagner Par	
T	Ro	ba	bc	Rp	δ	X/δ
C	Ω/cm	mV	mV	Ω	cm	
30	17.21	50	36	370.27	21.51	0.12
40	14.68	40	34	325.13	22.15	0.11
50	12.79	27	25	229.64	17.95	0.14
60	11.34	25	30	241.24	21.28	0.12

Temperature	Seawater Res	Polarisation Parameters		Polarisation Res	Wagner Par	
T	Ro	ba	bc	Rp	δ	X/δ
C	Ω/cm	mV	mV	Ω	cm	
30	17.21	45	40	374.63	21.77	0.115
40	14.68	43	36	346.65	23.62	0.106
50	12.79	25	18	185.13	14.47	0.173
60	11.34	29	33	273.06	24.09	0.104

Table 6.9a-c Seawater resistivity (R_o), alloy 625 Tafel slopes (b_a & b_C) and polarisation resistance (R_P), Wagner polarisation parameter (δ) and number (x/δ) at different temperatures.

D4. Breakdown Potential and Critical Pitting Temperature

Three potentiodynamic polarisation curves were obtained at each 5°C increment in 30 - 70°C interval. Each curve exhibits a breakdown potential. In this work, breakdown potential (E_b) is defined as the potential at which the current density equals 10 μA/cm^2 in the potentiodynamic polarisation curve (Figure 6. 8).

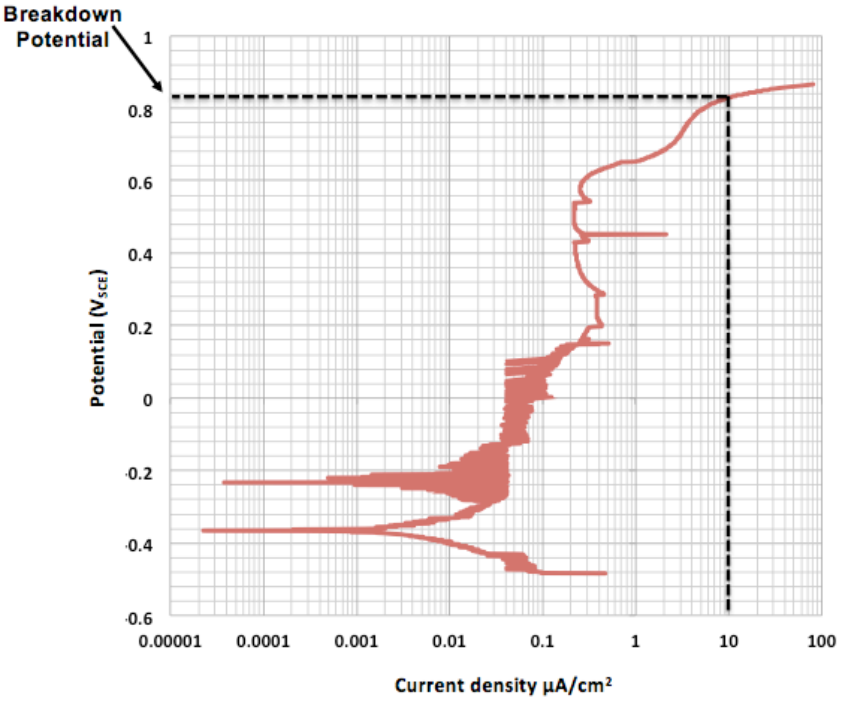

Figure 6. 6 Potentiodynamic polarisation curve for alloy 825 at 30 °C, showing its breakdown potential

Table 6. 11 to Table 6. 13 summarise the breakdown of alloy 825, 625 and alloy 825 weldment at different temperatures obtained from potentiodynamic polarisation curves (see Appendix B).

Alloy 825 Sample

Temperature	30 ºC	35 ºC	40 ºC	45 ºC	50 ºC	55 ºC	60 ºC	65 ºC	70 ºC
Breakdown Potential (V vs SCE)	0.828	0.835	0.805	0.810	0.438	0.168	0.320	0.230	0.200
//	0.854	0.829	0.800	0.737	0.315	0.254	0.264	0.201	0.209
//	0.856	0.836	0.825	0.738	0.396	0.210	0.370	0.200	0.197
mean	0.846	0.833	0.810	0.761	0.383	0.211	0.292	0.210	0.202
std	0.016	0.004	0.013	0.042	0.063	0.043	0.053	0.017	0.007

Table 6. 10 Breakdown Potential of alloy 825 at different temperatures

Alloy 625 Sample

Temperature	25 ºC	30 ºC	40 ºC	50 ºC	60 ºC	70 ºC	80 ºC
Breakdown Potential (V vs SCE)	0.0835	0.357	0.332	0.345	0.250	0.1805	0.170
//	0.1721	0.314	0.302	0.305	0.278	0.1795	0.161
//	0.347	0.326	0.358	0.337	0.241	0.2054	0.167
mean	0.201	0.332	0.331	0.329	0.256	0.188	0.166
std	0.134	0.022	0.028	0.021	0.019	0.015	0.005

Table 6. 11 Breakdown potential of alloy 625 at different temperatures

Alloy 825 Weldment

Temperature	30 ºC	40 ºC	45ºC	50 ºC	55 ºC	60 ºC	65 ºC
Breakdown Potential (V vs SCE)	0.765	0.737	0.689	0.369	0.220	0.234	0.203
//	0.762	0.714	0.712	0.563	0.301	0.211	0.220
//	0.801	0.748	0.714	0.301	0.248	0.200	0.204
mean	0.776	0.733	0.705	0.411	0.256	0.215	0.209
std	0.022	0.017	0.014	0.137	0.041	0.017	0.010

Table 6. 12 Breakdown potential of alloy 825 weldment at different temperatures

To determine the critical pitting temperature, E_b was plotted as function of the test temperature, which produced a reverse. For alloy 825 the onset of pitting resulted in a stepper decrease in potential. Therefore, CPT was considered to be the in the temperature interval where E_b dropped from the high potential range to the low potential range.